AD-A084 446 PENNSYLVANIA STATE UNIV UNIVERSITY PARK APPLIED RESE--ETC F/G 21/5
THE UNSTEADY RESPONSE OF AN AXIAL FLOW TURBO-MACHINERY ROTOR TO--ETC(U)
OCT 78 L C BARR N00017-73-C-1418
UNCLASSIFIED ARL/PSU/TM-78-253 NL

1 OF 3
AD A
084446

LEVEL II

THE UNSTEADY RESPONSE OF AN AXIAL FLOW TURBOMACHINERY ROTOR TO INLET FLOW DISTORTIONS

Barr, L. C.

Technical Memorandum
File No. 78-253
October 12, 1978
NASA Research Grant NSG 3031

Copy No. 1

Contract N00017-73-C-1418

The Pennsylvania State University
Institute for Science and Engineering
APPLIED RESEARCH LABORATORY
Post Office Box 30
State College, PA 16801

National Aeronautics and Space Administration

Approved for Public Release
Distribution Unlimited

UNCLASSIFIED

SECURITY CLASSIFICATION OF THIS PAGE *(When Data Entered)*

REPORT DOCUMENTATION PAGE

READ INSTRUCTIONS BEFORE COMPLETING FORM

1. REPORT NUMBER: TM-78-253	2. GOVT ACCESSION NO.: AD-A084 446
3. RECIPIENT'S CATALOG NUMBER:	
4. TITLE (and Subtitle): THE UNSTEADY RESPONSE OF AN AXIAL FLOW TURBOMACHINERY ROTOR TO INLET FLOW DISTORTIONS.	5. TYPE OF REPORT & PERIOD COVERED: Technical Memorandum
	6. PERFORMING ORG. REPORT NUMBER:
7. AUTHOR(s): Barr, L. C. / Barr	8. CONTRACT OR GRANT NUMBER(s): N00017-73-C-1412, NSG-3031
9. PERFORMING ORGANIZATION NAME AND ADDRESS: Applied Research Laboratory, P. O. Box 30, State College, PA 16801	10. PROGRAM ELEMENT, PROJECT, TASK AREA & WORK UNIT NUMBERS: 216
11. CONTROLLING OFFICE NAME AND ADDRESS: National Aeronautics and Space Administration, Cleveland, OH 44135	12. REPORT DATE: 12 Oct 1978
	13. NUMBER OF PAGES: 208
14. MONITORING AGENCY NAME & ADDRESS *(if different from Controlling Office)*: ARL/PSU/TM-78-253	15. SECURITY CLASS. *(of this report)*: UNCLASSIFIED
	15a. DECLASSIFICATION/DOWNGRADING SCHEDULE:

16. DISTRIBUTION STATEMENT *(of this Report)*

Approved for Public Release. Distribution Unlimited
Per NAVSEA - October 26, 1978 and National Aeronautics and Space Administration - April 23, 1980.

17. DISTRIBUTION STATEMENT *(of the abstract entered in Block 20, if different from Report)*

18. SUPPLEMENTARY NOTES

Submitted in Partial Fulfillment of the Master of Science Degree in Aerospace Engineering, March 1979.

19. KEY WORDS *(Continue on reverse side if necessary and identify by block number)*

turbomachinery
unsteady response
flow distortion
axial flow
inlet flow

20. ABSTRACT *(Continue on reverse side if necessary and identify by block number)*

An investigation was conducted to study the unsteady response of an axial flow turbomachinery rotor to spatial variations in the rotor inflow velocity. Distorted inlet flow is a very realistic and prevalent problem in jet aircraft engines, and the consequences of subjecting the rotating blades of an axial flow fan or compressor to an inlet distortion are excessive radiated noise, blade vibration, and performance degradation. Therefore, it is important for the turbomachinery designer to be concerned with designs which minimize the unsteady response of turbomachines to such spatial inlet dis-

DD FORM 1 JAN 73 1473 EDITION OF 1 NOV 65 IS OBSOLETE

UNCLASSIFIED

SECURITY CLASSIFICATION OF THIS PAGE *(When Data Entered)*

20. tortions. The study discussed in this report is a combination of experimental and analytical efforts which are directed toward obtaining information relating the influence of distortion characteristics and rotor design and operating variables such as solidity, stagger angle, rotor-stator spacing, and blade loading to the unsteady rotor response. The approach taken to measure the response of the rotor was to make detailed circumferential surveys of the time-mean flow field upstream and downstream of the rotor using five-hole prism type probes. This enables the total pressure, static pressure, and the three components of velocity to be determined. These data were then Fourier analyzed to provide a method of quantifying the size of the distortion, thus permitting the attenuation of the distortion to be evaluated. A portion of the data obtained in this study was analyzed to determine the total pressure losses associated with a distorted inflow.

The results of this investigation revealed that the attenuation of the distortion is a function of the blade stagger angle, the distortion reduced frequency, and the intrablade frequency. Little effect of rotor steady blade loading or of rotor-stator spacing was observed. It was shown that the attenuation of the distortion was maximized at values of rotor blade spacing corresponding to one-half the wavelength of the distortion. The amount of attenuation measured experimentally was found to be much greater than that predicted by an unsteady, two-dimensional, inviscid theory. However, the trends of the predicted and measured attenuation with reduced frequency or intrablade frequency were similar. This discrepancy is attributed to blade thickness and viscous effects which were neglected in the theory. In most cases, the unsteady total pressure losses were found to be greater than the losses in a uniform flow, and the effect of measuring the losses at radial locations other than the mean radius of the blade was significant.

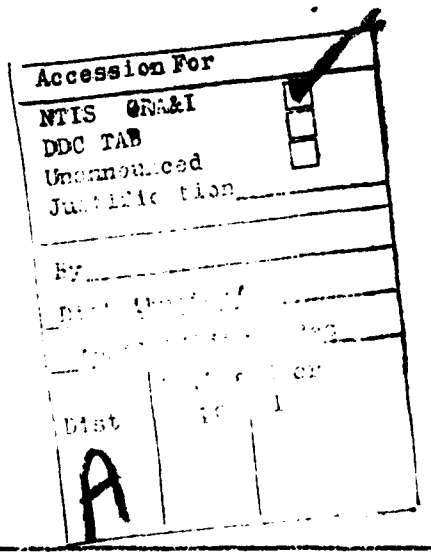

ABSTRACT

An investigation was conducted to study the unsteady response of an axial flow turbomachinery rotor to spatial variations in the rotor inflow velocity. Distorted inlet flow is a very realistic and prevalent problem in jet aircraft engines, and the consequences of subjecting the rotating blades of an axial flow fan or compressor to an inlet distortion are excessive radiated noise, blade vibration, and performance degradation. Therefore, it is important for the turbomachinery designer to be concerned with designs which minimize the unsteady response of turbomachines to such spatial inlet distortions. The study discussed in this report is a combination of experimental and analytical efforts which are directed toward obtaining information relating the influence of distortion characteristics and rotor design and operating variables such as solidity, stagger angle, rotor-stator spacing, and blade loading to the unsteady rotor response. The approach taken to measure the response of the rotor was to make detailed circumferential surveys of the time-mean flow field upstream and downstream of the rotor using five-hole prism type probes. This enabled the total pressure, static pressure, and the three components of velocity to be determined. These data were then Fourier analyzed to provide a method of quantifying the size of the distortion, thus permitting the attenuation of the distortion to be evaluated. A portion of the data obtained in this study was analyzed to determine the total pressure losses associated with a distorted inflow.

The results of this investigation revealed that the attenuation of the distortion is a function of the blade stagger angle, the distortion reduced frequency, and the intrablade frequency. Little effect of rotor steady blade loading or of rotor-stator spacing was observed. It was

shown that the attenuation of the distortion was maximized at values of rotor blade spacing corresponding to one-half the wavelength of the distortion. The amount of attenuation measured experimentally was found to be much greater than that predicted by an unsteady, two-dimensional, inviscid theory. However, the trends of the predicted and measured attenuation with reduced frequency or intrablade frequency were similar. This discrepancy is attributed to blade thickness and viscous effects which were neglected in the theory. In most cases, the unsteady total pressure losses were found to be greater than the losses in a uniform flow, and the effect of measuring the losses at radial locations other than the mean radius of the blade was significant.

TABLE OF CONTENTS

TABLE OF CONTENTS (Continued)

LIST OF TABLES

LIST OF FIGURES

LIST OF FIGURES (Continued)

LIST OF FIGURES (Continued)

LIST OF FIGURES (Continued)

LIST OF FIGURES (Continued)

LIST OF FIGURES (Continued)

LIST OF FIGURES (Continued)

NOMENCLATURE

A_n	Fourier amplitude of n^{th} harmonic
a_n, b_n	Fourier coefficients of n^{th} harmonic
B	number of rotor blades
C	chord length (in., cm)
C_D	steady drag coefficient on the blades
C_L	steady lift coefficient on the blades
$C_{P_{T\ loss}}$	total pressure loss coefficient
$C_{P\ pitch}$	pitch coefficient
$C_{P\ static}$	static pressure coefficient
$C_{P\ total}$	total pressure coefficient
$C_{P\ yaw}$	yaw coefficient
h_o	total enthalpy per unit mass (BTU/lb_m, J/kg)
i	angle of incidence (degrees)
ℓ	distortion wavelength (ft, m)
N	number of distortion cycles
P_{ATM}	atmospheric pressure (psf, pascals)
P_T	total pressure (psf, pascals)
P_S	static pressure (psf, pascals)
PA	pitch angle relative to axial reference (degrees)
r	radius (in., cm)
S	blade spacing (in., cm)
t	time (sec)
T	period (sec)
U	blade speed at the mean radius (fps, mps)
V	absolute velocity (ft/sec, m/sec)
W	relative velocity (ft/sec, m/sec)

NOMENCLATURE (Continued)

w	work per unit mass (BTU/lb_m, J/kg)
W_{CV}	total work transfer to control volume (BTU/lb_m, J/kg)
X	axial position (ft, m)
y, θ	circumferential position
YA	yaw angle relative to axial reference (degrees)
α	angle of absolute flow with axial direction (degrees)
β	angle of relative flow with axial direction (degrees)
γ	pitch angle relative to the probe (degrees)
Γ	total blade circulation (ft^2/sec, m^2/sec)
μ	yaw angle relative to the probe (degrees)
ν	distortion frequency (= $2\pi V/\ell$)
ξ	stagger angle (degrees)
ρ	mass density (slugs/ft^3, kg/m^3)
σ	angle of probe rotation in the yaw plane (degrees)
τ	intrablade frequency (= $-2\pi S/\ell$)
Φ	flow coefficient (= V_X/U)
ϕ	Fourier phase angle (degrees)
Ψ	pressure rise coefficient
ω	reduced frequency (= $\nu C/2W_m$)

Subscripts

m	mean value
X	axial direction
y, θ	circumferential direction
R	radial direction
SS	steady state

NOMENCLATURE (Continued)

Subscripts (Continued)

MC	blade midchord
LE	blade leading edge
TE	blade trailing edge
1	upstream of blade row
2	downstream of blade row

Superscripts

-	time-mean value
~	unsteady value

ACKNOWLEDGMENTS

The author gratefully acknowledges his adviser, Dr. Robert E. Henderson, for his guidance and consultation throughout the entire project. A special thanks goes to Mr. Adam Yocum, whose assistance in the experimentation and data reduction portions of this investigation proved to be invaluable. The author also wishes to acknowledge Mr. R. F. Davis for his help with the computer programming. Thanks also go to Mr. E. P. Bruce, Mr. G. B. Gurney, Mr. R. W. Woods, and Mr. S. S. Ross for their help in completing the experimental studies.

This work was conducted in the Applied Research Laboratory of The Pennsylvania State University under contract with the Naval Sea Systems Command, and under sponsorship of National Aeronautics and Space Administration Research Grant NSG 3031.

CHAPTER I

INTRODUCTION

1.1 Significance of Unsteady Flow in Turbomachinery

In designing the blading of a compressor or turbine, the air flow is assumed to be steady. The existence of a uniform, steady flow is unusual, however, due to the presence of viscous or real fluid effects. In a real flow, for example, viscous effects will result in wall boundary layers, wakes behind solid surfaces, and turbulence. As a result, the forces on a blade will vary with time as the flow field over the blade changes. Development of sophisticated instrumentation techniques has confirmed the presence of strong unsteady effects which can affect the aerodynamic performance, the aeroelastic performance, and noise generation in turbomachines. Very successful turbomachines have been developed in the past by compensating for the inadequate understanding of unsteady flows with extensive empirical correlations.

The existence of time-varying or unsteady forces and pressure results in noise, vibration, and a time-varying propulsive performance of a turbomachine. In general, these results are undesirable, and while it is not possible to eliminate their existence, it is desirable to minimize their occurrence.

In a turbomachine, the existence of upstream blades means that the blades will experience a time-varying flow and hence unsteady forces due to the relative motion between blade rows. Adjacent blade rows of turbomachines are usually placed as closely together as mechanical constraints will allow. In such an arrangement, dictated by the need to save engine cost and weight, some blade rows may be subjected to strong potential pressure fields from the downstream rows. A rotor passing through a

potential field of a stator will be subjected to time-dependent pressure fluctuations which may cause significant vibratory stresses. In addition to spatial velocity variations from wakes, similar variations can arise due to wall boundary layers, wall separation, and the existence of upstream bends and turns.

In recent years, the radiated noise and vibration have become important operating characteristics of the turbomachine requiring the consideration of the designer. A portion of the noise and vibration created in a turbomachine is the result of the time-dependent interaction of its blades with disturbances in the flow, both spatial and temporal. This interaction results in an unsteady or time-dependent lift on the blades. Thus, the design of turbomachines with noise and vibration levels which meet the established standards requires that time-dependent design methods be available. Unfortunately, the complexity of the flow through a turbomachine has made this a tremendous problem for the designer. The flow through an axial flow compressor, fan, or turbine stage is generally far more complicated than the flow over an isolated wing or wing-body combination. This is because of blade-to-blade interference, hub-to-tip variations along and between blades, interactions between rotating and non-rotating stages due to circulation, thickness and wake effects, and inlet distortions. The design methods resulting from the assumption of steady, time-independent flow do not allow for the consideration of the unsteady lift. Higher relative speeds, higher pressure ratios, and thinner blades have compounded the research and design problems in recent years.

Distorted inlet flow has emerged as one of the most serious problems facing the turbomachinery designer. Distorted inlet flow is a term which

is generally used to describe the flow entering a turbomachine where the flow had radial or circumferential variations in pressure, velocity, or temperature. Although both radial and circumferential distortions are present in compressors and fans, the circumferential distortion poses an additional complication since the flow relative to a moving blade row will be unsteady. Inlet flow distortions are a very realistic and prevalent problem in modern aircraft jet engines since the engines must operate under many different conditions. They can be caused by many sources, such as shock-boundary layer interaction in a supersonic inlet, crosswind-induced inlet separation, and armament firing. These and similar conditions cause pressure, temperature, and foreign gas type of distortions, and the result is generally reduced performance and stability of the compressor system.

In the flight environment, a turbojet engine must contend with disturbances due to atmospheric turbulence and the aircraft flow field, as well as with internal perturbations caused by the inlet and its controls. Therefore, the axial flow compressor may be required to operate at flow rates and pressure ratios other than the flow rate and pressure ratio for which it is designed. This especially occurs in the operation of the high pressure ratio compressor in the aircraft gas turbine cycle. The operating conditions of the compressor at speeds other than the design speed are defined by the performance of the turbine driving the compressor, the area of the outlet nozzle, and the aircraft speed and altitude. There is an unstable limit of operation known as surge, marked by a complete breakdown of the continuous steady flow through the whole compressor, resulting in large fluctuations of flow with time. When the incidence angle and subsequently the loading on an airfoil is increased, a point is

reached when the flow will separate from the suction surface of the airfoil. When this occurs in a compressor, surge can occur. Surge will result in very large fluctuating forces on the blades which may easily lead to oscillations violent enough to destroy the compressor blades.

Another important unstable condition connected with unsteady inlet flow which can lead to compressor damage is rotating stall. This is a phneomenon related to compressors working with throttled through flow and usually at rotational speeds lower than nominal speed. If a blade row is on the verge of stalling, it is likely that one particular blade will stall before another neighboring blade. A single stalled blade results in a flow diversion which tends to overload one adjacent blade and unload the other adjacent blade. The overloaded blade will then stall and the resulting flow diversion will unload the originally stalled blade. This process is repeated, and the stall cell (i.e., the region of very low flow rate) propagates in the opposite direction as the rotation of the rotor. In actual cases there may be more than one stall cell rotating on a single blade row. In general, the zones of stall, which may cover several blade spacings, rotate at about half the rotor blade speed. The alternate loading and unloading of the blades sets up an alternating stress on each blade. This stress in itself is not large unless the forcing frequency happens to match a blade vibrational frequency. In this case, large stresses are present and fatigue failure can occur, resulting in complete destruction of an entire blade row. Little can be done to prevent this failure, other than avoiding operation at speeds corresponding to resonance. Rotating stall is more dangerous than other unsteady phenomena to the survival of the compressor.

Both surge and rotating stall are unstable conditions which may severely damage a turbomachine. In order to prevent this from occurring,

the stall limit as a function of pressure rise and flow rate is established and controls are designed to prevent the machine from entering the unstable region of its operating range. An engine has to satisfy a number of often conflicting requirements such as adequate stability, low fuel consumption, long life, low weight, and low cost. To achieve an optimum performance compromise, the engine is designed to have just enough stability margin to function adequately. The required stability margin, which is defined as the margin between the engine operating line and the limit of engine stable operation, has to allow for a number of effects including the magnitude and extent of the nonuniformity of the flow entering the compressor. Therefore, the problem caused by distorted inlet flow is that the stability limit is lowered by the distortion, and unstable conditions will occur at a higher flow rate and lower pressure rise. It is therefore important for the designer to accurately predict the effect of distorted inlet flow on compressor performance and to design distortion tolerant compressors.

The phenomena that lead to performance degradation in compressors subjected to distorted inlet flows are essentially unsteady. In the absence of an understanding of the unsteady flow dynamics, compressor performance prediction techniques are steady state in concept. Further, predictions involving stage analysis are restricted to using steady state characteristics. Unsteady flow modelling techniques have been applied successfully to cascades, but usually with the limitations of inviscid flow and small perturbation assumptions, thus preventing investigations in highly nonlinear areas of response such as stall. There is therefore considerable need for the improvement of flow distortion models, but without experimental data to quantify unsteady response behavior of blade

rows, stages, and complete compressors, improvements that may take account of unsteady phenomena are difficult to make.

1.2 Status of Existing Knowledge

As mentioned in the previous section, the existence of unsteady lift on the moving or stationary blades of a turbomachine is caused by vibration of the blades, potential flow interactions due to the relative motion of adjacent blade rows, and inlet flow distortions. There are different ways to experimentally study the unsteady response of a turbomachine rotor. One approach is to obtain measurements of the unsteady normal force and moment acting on a rotor blade by instrumenting the blade with strain gages. A second method used to determine the unsteady response of a rotor in a spatially varying inlet flow is to make measurements of the circumferential distribution of time-mean total pressure at the inlet and exit of the rotor. From these measurements, the unsteady circulation on the blades caused by their interaction with the inlet distortion can be determined.

Perhaps the best known method for the design analysis of the unsteady lift and moment in a turbomachine is that by Kemp and Sears [1, 2]. They described the aerodynamic interference between a stator and rotor with the simplifications of two-dimensional, incompressible, isolated airfoil theory. This method is an extension of the earlier original work by Von Karman and Sears [3], and Sears [4], which describes the unsteady lift generated on an isolated, flat plate airfoil subjected to velocity fluctuations normal to its chord. While including the steady interaction of the other airfoils in the cascade, the unsteady interaction and hence the effects of cascade spacing, are neglected by Kemp and Sears. They consider the problem of mutual

interference of blades in cascades due to relative motion of successive blade rows. They also extend this analysis to include the effects of viscous wakes on the unsteady forces on the blades in cascades. The method of Kemp and Sears provides a solution which expresses the unsteady lift as a function of reduced frequency, i.e., the ratio of airfoil chord length to disturbance wavelength. Although the unsteady contribution of the adjacent blades of the cascade is neglected, it is this type of solution which provides the designer with the required design information.

A further improvement to the theory of unsteady, incompressible aerodynamics of an isolated airfoil was presented by Horlock [5]. Horlock analyzes velocity disturbances both normal and parallel to a flat plate airfoil. The response of the isolated airfoil to the chordwise disturbance can be expressed in terms of the Horlock function which provides a design solution similar to that of Sears for a normal disturbance. Naumann and Yeh [6] extend this analysis to include the effect of blade camber. A series of design charts is presented which show the effects of blade camber, stagger angle, and reduced frequency on the generation of unsteady lift, assuming the turbomachine blade can be represented by a single airfoil.

The inclusion of the unsteady contribution of the neighboring blades of the blade row has been considered by Whitehead in Reference [7] and by Henderson and Daneshyar in Reference [8] for an incompressible flow. The analysis by Whitehead permits the unsteady lift and moment on a cascade of rigid flat plate airfoils interacting with upstream wakes to be determined, and his results are presented in the form of extensive tables of lift and moment coefficients for vibrating airfoils in cascade. This is a solution of the direct problem, that is, it analyzes the response of

a known cascade of airfoils. The method of Henderson and Daneshyar gives a functional relationship for the fluctuating lift on a cascade of airfoils similar to the analyses for an isolated airfoil presented in References [3], [4], [5], and [6]. The analysis in Reference [8] includes the unsteady contribution of the entire blade row and thus, represents an extension of existing indirect or design solutions of the unsteady response of an isolated airfoil to a cascade of airfoils. However, for the designer, the use of this type of solution is very laborious and time consuming, since a series of calculations must be conducted to determine a configuration with minimized unsteady lift.

All the theoretical analyses just discussed utilize similar mathematical representations to develop the resulting solutions. These representations replace the airfoil by a distribution of vorticity on the blade and in its wake. The strength of this vorticity and the resulting induced velocities satisfying the boundary conditions on the airfoil surface are then determined. This specifies the unsteady pressure distribution and hence the unsteady lift. For all cases, the flow is assumed to be inviscid, incompressible, and two-dimensional, with the airfoils being infinitely thin and the disturbance velocities small in comparison with the mean or free-stream velocity.

Linear theory continues to play an important role in predicting performance, stability, and flutter of turbomachines, especially in the difficult cases of compressors with supersonic relative velocities and subsonic axial velocities. Most of the current effort in unsteady research utilizes the two-dimensional cascade approximation, for which a large background of theory has been developed over the years. Significant

differences from isolated airfoils have been found, and it has been demonstrated that blade-to-blade interference can have a large unfavorable effect on flutter characteristics.

McCroskey, in his review of research in unsteady fluid dynamics [9], cites a number of studies which are representative of the most recent activity in the field of unsteady research. Verdon and McCune [10], Jones and Moore [11], and Rao and Jones [12] have developed somewhat different theories in terms of the subsonic velocity potential for flat plate blades. They describe the effects of varying reduced frequency, stagger angle, interblade phase angle, interblade spacing, and Mach number, and they indicate the possibility of torsional flutter over a wide range of conditions. Ni and Sisto [13] developed a fully numerical time-marching scheme for small unsteady perturbations about a steady mean flow. Both subsonic and supersonic results were presented, and they found indications of torsional instability in the supersonic case.

Adamczyk [14], and Goldstein and Atassi [15] also considered small-amplitude fluctuations about a steady mean flow, along with finite blade thickness, camber, and mean incidence. Their studies are detailed mathematical analyses of the response to incompressible gusts, and their results show a large influence of blade thickness and mean incidence angle. The analysis of Horlock, Greitzer, and Henderson [16] is an appropriate method which gives analytical expressions for the unsteady lift on a moving cascade of closely spaced airfoils of arbitrary finite chord. It is a much simpler analysis since it takes advantage of the channel-like flow behavior between closely spaced blades. It shows explicitly the variation of the fluctuating lift with the various

parameters, and it clearly shows the limiting behavior of cascades exposed to low-frequency gusts.

Most of the unsteady cascade theories available at the present time are either directly applicable to inlet distortion calculations or are applicable after proper modification of the boundary conditions. Two significant recent developments appear to be the inclusion of three-dimensional effects using small disturbance theory (i.e., the blades are assumed to be flat plates or slightly cambered blades set at zero or small incidence and the unsteady disturbances are assumed to be small) as demonstrated by Namba in Reference [17] and the incorporation of viscous loss hysteresis and effects of non-uniform exit pressure into a multi-segment parallel compressor model as demonstrated by Mazzawy in Reference [18]. Both approaches are likely to contribute toward a better understanding of the major physical effects which are presently combined in the empirically derived distortion indices used in current design practice.

In contrast to the large number of theoretical methods available for the analysis of the interaction of a turbomachine blade row with upstream disturbances, there is little systematic experimental data available. As a result, the validity of these various theoretical methods and the assumptions used has not been fully determined. There is a significant need to demonstrate whether the representation of the unsteady response of a blade row as an isolated airfoil is justifiable or not.

This lack of experimental measurements of the unsteady lift, particularly in a rotating blade row, is due to the complexity and size of the required instrumentation. The development of highly sensitive, miniaturized pressure transducers has resulted in the initiation of studies in several laboratories to measure the unsteady pressure

distributions on both moving and stationary blade rows. The development of a simplified experimental method for the determination of the response of a blade row, particularly a moving one, is desirable. Such a technique is suggested by the analysis by Horlock and Daneshyar [19], and Hawthorne [20] concerning the variations in total pressure in an unsteady flow.

These analyses reach the identical conclusion that if a moving blade row has unsteady lift on its blades, there will exist a spatial variation in the time-mean total pressure downstream of the blade row. This spatial variation can be related to the unsteady circulation on the blades. Thus, by conducting the relatively simple measurement of the time-mean total pressure, the unsteady response can be indirectly determined from a knowledge of the unsteady circulation. This technique is particularly useful in determining the unsteady response of the blade row to variations in blade geometry and disturbance characteristics. It also suggests a method for studying experimentally those turbomachines whose size and physical construction do not permit the installation of miniaturized sensors to directly measure the unsteady lift. In addition to the time-mean total pressure, Hawthorne also analyzes the instantaneous total pressure and shows this to be directly related to the unsteady lift on the blades. While this approach would give a direct indication of the unsteady lift, it requires more complex instrumentation to determine the instantaneous total pressure than is required to determine the time-mean total pressure. Therefore, the most straightforward method for experimentally determining the unsteady response of a moving turbomachine blade row is to make measurements of the time-mean total pressure. This method was used by Henderson and is thoroughly presented in Reference [21]. A more recent

investigation which helps to provide the kind of instantaneous and time-mean response data that are needed to determine the range of validity of various linear theories is that of Bruce and Henderson in Reference [22]. They have verified some of the cascade theories for lift and moment for actual rotor applications, but additional losses due to unsteady effects were found that are beyond the scope of inviscid linear theory. These losses were not predicted because the theories assume an inviscid flow.

There is clearly a strong and urgent need in both rotors and cascades for more of the detailed pressure measurements of the kind just mentioned as well as of the kind that Fleeter et al. in Reference [23] and Carta and St. Hilaire in Reference [24] have begun to accumulate. However, just as unsteady cascades are more complicated than isolated airfoils and depend upon many more parameters, so are complete turbomachines still more complex than cascades. Therefore, McCroskey, in Reference [9], states that a unified plan should be established in the near future to avoid a surplus of unwieldy experimental and numerical data. Additional simplified analyses in the manner of Horlock, Greitzer, and Henderson [16] will continue to be useful in identifying dominant flow features, in checking elaborate calculations, and in understanding the extensions from cascades to rotating machines.

Mathematical models have been developed to predict the response of axial compressors to distorted inlet flow. The various types of compressor responses to inlet distortions are loss in performance, loss in stability (surge or stall), attenuation of the distortion, perturbed flow fields, and unsteady blade forces. No mathematical model exists which would predict all of these responses for every compressor and every distortion. Instead, specialized models with different prediction capabilities are

available for specific types of inlet distortions and configurations of compressors.

The parallel compressor model is used to predict the effects of steady circumferential total pressure and/or total temperature distortions on the performance and stability of compressors. The model divides the distorted compressor into sections which are treated as hypothetical compressors working in parallel in a quasi-steady flow. The parallel compressor model is only suitable for circumferential inlet distortions because radial distortions induce a great amount of radial flow redistribution which contradicts a main assumption that there is no connection between the parallel compressors.

Roberts, Plourde, and Smakula [25] measured the attenuation of a 180 degree square wave total pressure inlet distortion in a single stage, two-stage, and three-stage compressor configuration. By utilizing the parallel compressor model and comparing the experimental and analytical results, they obtained reasonable agreement between experiment and theory. In a further experiment, Roberts, Plourde, and Smakula measured the performance characteristics of a three-stage compressor subjected first to a mild and then to a severe total pressure inlet distortion. Mild and severe total pressure inlet distortions are characterized by small and large ratios of the distorted total pressure amplitude to the undistorted or uniform total pressure amplitude. They compared the results with predictions obtained with the parallel compressor model and obtained good agreement between experiment and theory for the mild distortion. However, the agreement was found to be poor for the severe distortion near the peak pressure coefficient since the assumption of parallel compressor operation on the undistorted flow is invalid under the operating conditions that were used.

It is not immediately apparent from the parallel compressor analysis what steps should be taken in compressor design to achieve a rapid attenuation of steady circumferential inlet distortions through the compressor. It is also of interest to determine the impact of the assumption that all parallel compressors operate on the undistorted flow (i.e., zero circumferential crossflow) and also to get an idea of the flow redistribution upstream of the distorted compressor. The answers to these problems can be obtained from the two-dimensional linear body-force model presented by Plourde and Stenning in Reference [26]. The theory is restricted to compressors of high hub/tip ratio, so that the flow field can be regarded as two-dimensional. Further, the assumption is made that the flow is inviscid and incompressible. The compressor is assumed to consist of a large number of small stages, and the effect of these stages on the increase in pressure is simulated by an appropriate distribution of axial body forces.

Compressor stall at high rotor speeds is generally initiated in the later stages of a multi-stage machine. To deal with a steady circumferential total pressure inlet distortion, it is therefore important to design the front stages for rapid distortion attenuation. The body-force analysis is not very suitable for providing guidelines for such a design, since it assumes all stages to have an equal performance. Better guidelines may be obtained from a model which replaces the blade rows of the compressor individually by actuator discs, as presented in References [27], [28], and [29]. Actuator disc models are used when the parallel compressor model or the body-force model is invalid and also when the distortion shape and individual blade row attenuation is of primary concern. An actuator disc is a means of representing a blade row by

shrinking the chord length of the blade to zero and concentrating the effects of the blade rows at a single location while assuming a quasi-steady flow. The model can be described for compressors with high hub/tip ratio, thus allowing the flow field to be regarded as two-dimensional. It is also assumed that the flow outside the actuator discs is inviscid and incompressible. The assumption that the velocity perturbations are small compared with the mean axial velocity permits the equations of motion to be linearized. The axial spacing of the discs corresponds to the gaps between the blade rows since circumferential flow redistribution can only occur in these gaps. The flow fields upstream and downstream of the blade row can then be solved either by an analytical solution of linearized equations or by numerical methods. The solution of the linearized inviscid flow equations is suitable for studying distortion attenuation if the distortion is small. The nonlinear equations and the unsteady response must be used for large distortions and when stall phenomena is investigated. The parallel compressor and actuator disc theories, which were just discussed, do not accurately predict the unsteady response of the blade row since they are quasi-steady theories. A detailed description and summary of these types of overall performance and engine stability prediction techniques is presented by Mokelke in Reference [30].

The theoretical modelling of unsteady flow effects in turbomachines is largely limited to the analysis of lightly loaded cascades (i.e., to two-dimensional flow assumptions). The methods used involve direct extensions of the external flow solutions for unsteady flow past single airfoils in unbounded flow to the more difficult boundary value problem of unsteady flow past airfoil arrays. Thus, there is a direct relationship with the current status of unsteady external aerodynamics, and the

methods used in this field, such as airfoil modelling by vortex distributions, conformal mapping, transform techniques, etc., are directly applicable to turbomachinery unsteady aerodynamics. Furthermore, it should be noted that the methods developed for the flutter and forced vibration analysis of turbomachinery blading are equally applicable to turbomachinery noise studies.

Within the status of knowledge, the turbomachinery designer is restricted to the use of isolated airfoil theories and two-dimensional analyses of lightly loaded cascades to predict the unsteady response of a blade row. Thus, the range of applicability and the usefulness of the current methods are severely limited. Also, the practical utility of these current methods is further hampered by the lack of experimental measurements and the inaccessibility of the currently available results. As a result, the appreciation for the unsteady aerodynamic effects of turbomachines and the access to the available results is limited to a small number of specialists. However, a simplified experimental technique which employs measurements of the time-mean total pressure suggests a more expedient manner for obtaining the necessary data.

Platzer, in his review on current developments in unsteady turbomachinery aerodynamics [31], notes that a significant change in attitude and increase in research effort has taken place in the past decade. He concludes by distinguishing the following major developments and results:

1. Incompressible, subsonic and supersonic unsteady flow past lightly loaded single cascades has been studied in considerable detail, but relatively little comparative evaluation and documentation of the various solutions is available in this country.

2. Recently, solutions for incompressible unsteady flow past highly loaded cascades have also been published, but little information is yet available for subsonic and supersonic cascades with finite blade thickness and loading.
3. The unsteady transonic cascade problem is still unsolved, but some new approaches are presently in progress which are likely to provide new insight.
4. Work on the analysis of three-dimensional unsteady flow effects is in progress and some valuable new results for lightly loaded rotors have already been published.
5. New measuring techniques coupled with modern data acquisition systems are being applied to the investigation of unsteady cascade and rotor flows throughout the entire speed regime. A number of papers have recently been published which provide detailed unsteady flow and pressure information for comparison with the available theoretical models.
6. Progress has also been made towards the prediction of rotating stall and surge using nonlinear unsteady analyses, but much more experimental and theoretical work is required to understand and describe highly viscous and separated unsteady flow phenomena such as wake formations and interactions, stall flutter, etc.

In order to promote acceptance and use of unsteady flow information in turbomachinery research and design, increasing emphasis will have to be placed on the problem of data access, evaluation, and documentation [31]. Therefore, systematic comparisons and evaluations of various theoretical methods and experimental results should be conducted for well-defined test configurations. Further improvements in aircraft engine performance and the avoidance of aerodynamic and aeroelastic stability problems which cause expensive engine modifications will depend on the continued research effort in unsteady turbomachinery aerodynamics and on the transfer of highly specialized unsteady aerodynamic and aeroelastic information to the design community.

1.3 Statement of the Problem

In dealing with the problem of distorted inlet flows, designers of axial flow fans and compressors require a knowledge of the fluctuating forces on the blades, the attenuation of the distortion through each blade row, the loss in performance, and any reduction in stability caused by the distortion, as a function of the operating and geometrical design variables of the machine which the designer can control. Theoretical predictions are valuable in understanding distortion phenomena and also in making some design decisions; however, theory has several shortcomings when used in the design process. For example, when trying to predict distortion attenuation, performance loss, or stability limits of a compressor or fan, theoretical methods such as the parallel compressor theory and actuator disc model require the steady performance of the compressor or blade row to be known. Since the performance characteristics are determined by a number of geometric design parameters, these theoretical methods give very little insight into the selection of the proper design

parameters to be used in the design process. Unsteady airfoil theories and two-dimensional cascade analyses can be used for selecting design parameters to minimize the fluctuating lift on the blade, but these methods generally apply to lightly loaded blades and neglect viscous effects.

To aid in the continual development of theoretical design techniques and to help bridge the gap between present day theories and the needs of designers, experimental data of a fundamental nature demonstrating the effect of geometric and operating variables are needed. Most of the data available to date are not of this nature. Extensive studies have been made on modern aircraft engines to determine their response to distortions and to identify problem areas. These studies, however, are usually part of a continuing development program aimed at determining safe operating limits and suggesting modifications rather than providing the fundamental data needed for designing the next generation of engines.

The purpose of this investigation was to study the unsteady response of an axial flow turbomachine blade row to time-mean spatial variations in the rotor inlet flow. This program is a combination of experimental and analytical efforts which are directed toward obtaining information relating the influence of rotor geometrical and operating parameters, such as solidity, stagger angle, and steady load, on the unsteady rotor response. Specifically, the effect of the rotor employed in various geometric configurations on the distortion flow field was studied. Two test rotor configurations were employed in the experimental portion of this investigation. The effects of rotor solidity, stagger angle, and steady load (i.e., mean incidence angle) were examined using a six-bladed uncambered rotor. The effects of rotor-stator spacing and radial variations of the flow field were investigated with a cambered test rotor

consisting of nine blades. The effects of radial variations were determined by measuring the flow field at various spanwise locations along the blade. The approach taken to measure the response of the rotor was to make time-mean flow measurements upstream and downstream of the rotor. Detailed circumferential surveys of the time-mean flow field upstream and downstream of the rotor were made.

In addition to the experimental program, a theoretical analysis is presented which predicts the time-mean total pressure at the exit of the rotor. This theory is an unsteady cascade analysis, and it includes the unsteady blade-to-blade interaction effects. Thus, a basis of comparison is provided between experimental measurements and theoretical predictions using a two-dimensional, unsteady, inviscid, cascade analysis.

The objective of this study, then, is to provide some of the necessary fundamental data by examining the response of a turbomachinery rotor as a function of blade geometry and type of distortion. Comparison of these results with the predicted values of time-mean total pressure downstream of the rotor is also used to determine the validity of the unsteady analysis and the practicability of the experimental technique. These data will form a basis from which design data can be derived which should result in axial flow fan configurations with improved performance when operated in an inlet distortion.

CHAPTER II

THEORETICAL ANALYSIS

2.1 Prediction of Time-Mean Total Pressure at the Exit of a Rotating Blade Row

The operation of a turbomachine in a spatially varying inflow will result in the generation of time-varying or unsteady pressures and forces on the blades. This unsteady response will also lead to a variation in the time-mean flow as it passes through the blade row. From a knowledge of the absolute flow in front of and behind the blade row, it is possible to determine the unsteady response of the blades. Specifically, it is possible to determine the unsteady circulation on the blades which can then be used to predict the unsteady effect of the turbomachine rotor on the inflow distortion. The characteristics of the distortion after its passage through the rotor are important for the determination of the unsteady interaction of subsequent blade rows.

The analyses of Horlock and Daneshyar in Reference [19] and Hawthorne in Reference [20] show that if a moving blade row has an unsteady lift on its blades, then a spatial variation in time-mean total pressure which is associated with the unsteady lift will exist downstream of the blade row. This variation in time-mean total pressure can be related to the unsteady circulation on the blades, thus describing its unsteady response. The work of Horlock and Daneshyar also suggests an experimental procedure which permits the unsteady response of a rotating blade row to spatial variations in its inlet flow to be determined from measurements of the time-mean total pressure. Henderson [32] employs this experimental procedure to determine the unsteady circulation on a rotating blade row exposed to a spatially varying inlet flow.

By reversing the procedure described by Henderson in Reference [32], it is possible to predict the circumferential variation of time-mean total pressure at the exit of the blade row. This is precisely the problem which was undertaken in this investigation. In the following sections, the theoretical development is presented which results in the equation used to predict the time-mean total pressure at the exit of the rotor. Horlock and Daneshyar present the derivation of the equation describing the variation of time-mean total pressure in unsteady flow. They derive this result using two different analyses. For a complete derivation of the time-mean total pressure downstream of a row of blades with fluctuating circulation using a vortex analysis, refer to Reference [19]. The changes in total pressure produced by movement of rows, arrays, and sheets of vortices are derived. This result can also be derived from energy considerations, and a detailed formulation of this procedure is presented here.

2.1.1 Steady Transport of a Distortion Through a Blade Row. Consider a two-dimensional cascade of airfoils operated in a distorted flow which varies sinusoidally along the face of the cascade as shown in Figure 1. The variation of total pressure shown in Figure 1 exists in the presence or absence of the rotor. The presence of the rotor will induce a circumferential velocity upstream of the rotor which will influence the axial velocity and static pressure. As the distortion is carried through the moving cascade, it is transported in the circumferential direction by an amount dependent upon the amount of mean swirl (i.e., circumferential velocity) introduced by the blades.

The velocity diagram of the flow relative to the rotor is shown in Figure 2. Also shown are the relative mean streamlines of the flow as it

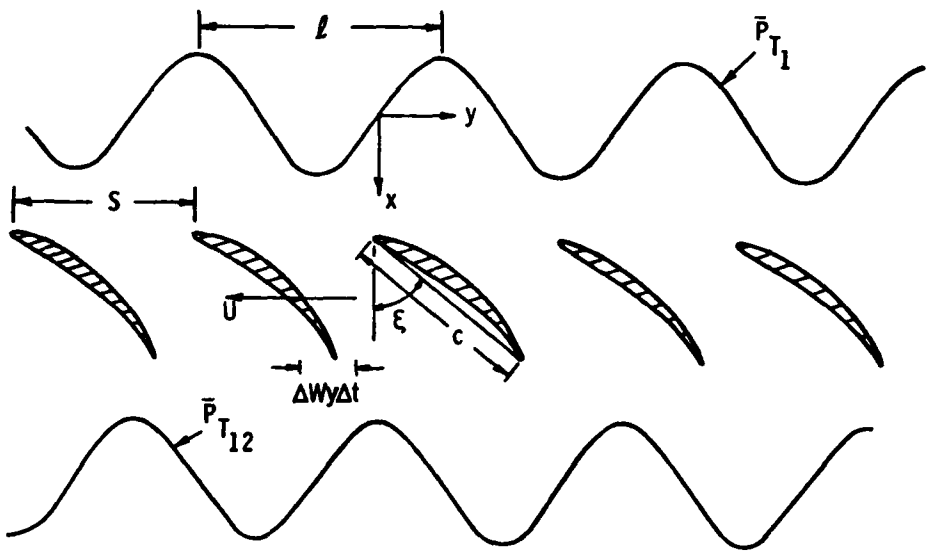

Figure 1. Passage of Distortion Through Rotor

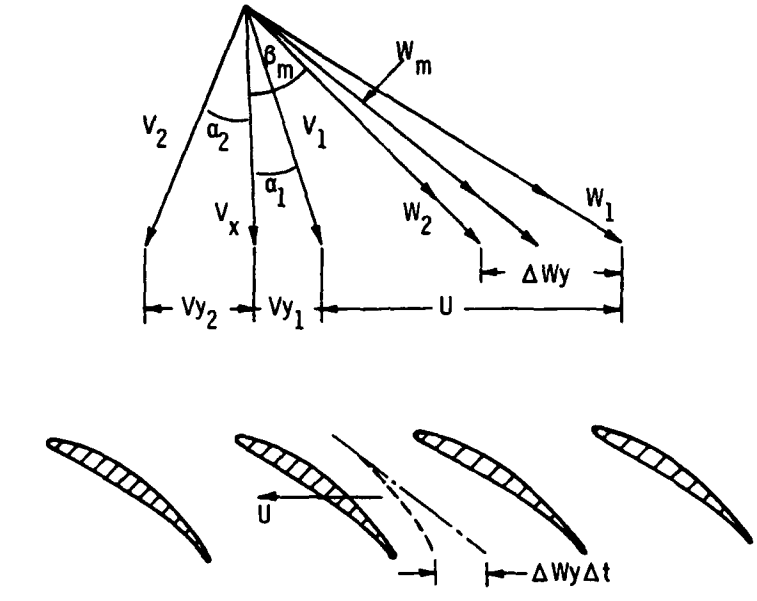

——·——RELATIVE STREAMLINE, CL = 0

- - - - - - - RELATIVE STREAMLINE, CL ≠ 0

Figure 2. Flow Relative to Rotor

passes through the rotor for the cases of zero steady lift and non-steady lift on the blades. Assume that the time-mean total pressure distribution at the cascade inlet can be expressed as:

$$\overline{P_{T_1}} = A_n e^{i \frac{2\pi y}{\ell}} . \tag{1}$$

From Figure 2, it is seen that the time for a particle of fluid to be transported through the cascade is:

$$\Delta t = \frac{C}{W_m} , \tag{2}$$

where W_m is the mean relative velocity through the cascade. In this length of time, a fluid particle is transported in the circumferential direction a distance equal to $\Delta W_y \cdot \Delta t$ where ΔW_y is the change in time-independent tangential or circumferential-mean velocity relative to the cascade. Thus, at the exit of the cascade the inlet distortion given in Equation (1) has the form:

$$\overline{P_{T_{12}}} = A_n e^{i\{\frac{2\pi}{\ell} [y-(\Delta W_y \cdot \Delta t)]\}} , \tag{3}$$

where y is the circumferential measurement location. Since $\Delta W_y = W_{y_1} - W_{y_2} = V_X (\tan\beta_1 - \tan\beta_2)$ if V_X = constant, Equation (3) becomes:

$$\overline{P_{T_{12}}} = A_n e^{i\{\frac{2\pi}{\ell} [y- \frac{(W_{y_1} - W_{y_2})}{V_X} \frac{V_X}{W_m} C]\}} \tag{4}$$

and

$$= A_n e^{i\{\frac{2\pi}{\ell}\,[y - \frac{V_X(\tan\beta_1 - \tan\beta_2)}{V_X}\,\frac{V_X}{W_m}\,C]\}} \quad . \tag{5}$$

But from Figure 2, $\frac{V_X}{W_m} = \cos\beta_m$; thus,

$$\overline{P_{T_{12}}} = A_n e^{i\{\frac{2\pi}{\ell}\,[y-(\tan\beta_1 - \tan\beta_2)\,C\,\cos\beta_m]\}}. \tag{6}$$

The steady lift coefficient on the blades can be written as (see Reference [33]):

$$C_L = 2(\frac{S}{C})\,[\tan\beta_1 - \tan\beta_2]\,\cos\beta_m - C_D\,\tan\beta_m \tag{7}$$

Therefore, substitution of Equation (7) into Equation (6) gives:

$$\overline{P_{T_{12}}} = A_n e^{i\{\frac{2\pi}{\ell}\,[y-\,(C_L + C_D\,\tan\beta_m)\,\frac{C}{2(S/C)}\,]\}}\,. \tag{8}$$

This is the expression for the inlet distortion downstream of the rotor blade row after it has been transported through the blades with the circumferential-mean or steady flow assuming that its amplitude A_n is constant, i.e., there is no mixing or diffusion of the distortion.

2.1.2 Influence of Unsteady Blade Forces. The forces on the blades of an isolated turbomachine rotor relative to the blade row are constant if the flow entering the blade row is uniform. This implies that the total pressure must increase across the blade row if work is done on the fluid. A total pressure probe located downstream of the

rotor in the absolute reference frame (i.e., fixed with respect to the casing wall) will sense an instantaneous total pressure variation which will be constant when it is averaged with time. Therefore, the time-mean total pressure downstream of a rotating blade row with time invariant forces is constant.

If the blades experience an unsteady force, Horlock and Daneshyar [19] and Hawthorne [20] have shown that the time-mean total pressure will vary in the absolute frame of reference. This variation is a function of the time-mean absolute flow angle at the rotor exit and the unsteady circulation on the blades. Thus, it is possible to determine the unsteady characteristics of the blades, in particular the unsteady circulation, from measurements of the time-mean total pressure. This procedure was demonstrated in Reference [32].

While the relationship of the time-mean total pressure downstream of the blades, $\overline{P_{T_2}}$, can be derived by a vortex analysis of the blades, as was done in References [19] and [20], it can also be derived by considering the energy exchange across the blade row, as shown in Reference [19]. In a turbomachine, the flow can be considered as adiabatic. Therefore, the energy equation, neglecting potential energy effects and considering a compressor application, can be written as:

$$h_{o_2} - h_{o_1} = w \ . \tag{9}$$

This expression relates the energy per unit mass through a control volume. If a control volume fixed in the absolute reference frame is considered, as shown in Figure 3, then the mass flow rate is $\dot{m} = \rho V dy$. Therefore, Equation (9) for a length of time dt becomes:

$$\rho V h_{o_2} dydt - \rho V h_{o_1} dydt = dW_{CV} , \tag{10}$$

where dW_{CV} is the work transferred to the control volume in time dt. As seen in Figure 3, the axial velocity V is assumed to be constant throughout the control volume.

The blades shown in Figure 3 are moving in the circumferential or y direction with a velocity U and have a blade-to-blade spacing of S. Hence, for an incompressible, isentropic flow, integration of Equation (10) over the period T = S/U gives:

$$\rho V\left(\frac{\overline{P_{T_2}} - \overline{P_{T_{12}}}}{\rho}\right) T\, dy = \Delta W_{CV} , \tag{11}$$

where ΔW_{CV} is the total work transfer to the control volume in the period T. This work transfer occurs when a blade passes through the control volume.

The circulation on the blade is unsteady and assumed to have the harmonic form

$$\tilde{\Gamma} = \Gamma_{SS} + |\tilde{\Gamma}| e^{-i(\nu t + \pi - \phi_{TE})} , \tag{12}$$

where Γ_{SS} is the steady-state circulation, $|\tilde{\Gamma}|$ is the magnitude of the unsteady circulation, ν is the frequency of the variation of the unsteady circulation relative to the moving blades, and ϕ_{TE} is the phase angle between the steady and unsteady circulation. ϕ_{TE} is referenced to the blade trailing edge since that is where the vorticity (or circulation) is shed into the absolute flow or wake and, hence, enters the control volume. The addition of π in the exponential term of Equation (12) is

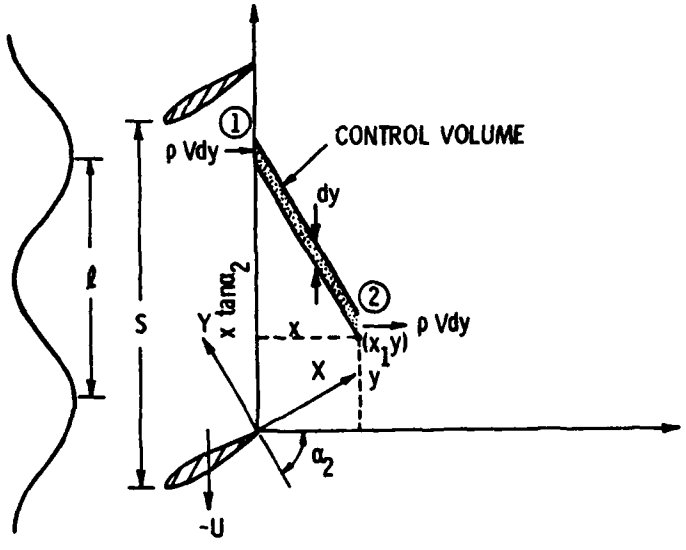

Figure 3. Control Volume

due to the fact that the quasi-steady circulation is 180 degrees, or π radians, out of phase with the distortion. All terms in the unsteady analysis must be referenced to the distortion, thus the factor of π must be included. From Figure 3, the frequency ν is equal to $-2\pi U/\ell$ and the length of one period T is $t = -(y + x\tan\alpha_2)/U$. And since $e^{-i\pi} = \cos\pi - i\sin\pi = -1$, Equation (12) can be expressed as

$$\tilde{\Gamma} = \Gamma_{SS} - |\tilde{\Gamma}| e^{-i[\frac{2\pi}{\ell}(y + x\tan\alpha_2) - \phi_{TE}]} . \tag{13}$$

It is assumed that the lift on the blades and their circulation are in phase with each other. This is a valid assumption for low values of reduced frequency. Then the work done, ΔW_{CV}, is the product of the y component of the lift, $\rho V\Gamma$, and the distance moved, dy; i.e.:

$$\Delta W_{CV} = \rho V \Gamma dy . \tag{14}$$

Recalling that the period $T = S/U$ and combining Equations (11), (13), and (14) gives:

$$\Delta W_{CV} = \rho V \left(\frac{\overline{P_{T_2}} - \overline{P_{T_{12}}}}{\rho}\right) T \, dy \tag{15}$$

or

$$\Delta W_{CV} = V \left(\overline{P_{T_2}} - \overline{P_{T_{12}}}\right) \frac{S}{U} dy . \tag{16}$$

But,

$$\Delta W_{CV} = \rho V \Gamma dy = \rho V \Gamma_{SS} dy - \rho V |\tilde{\Gamma}| e^{-i\left[\frac{2\pi}{\ell}(y + x\tan\alpha_2) - \phi_{TE}\right]} dy \ . \qquad (17)$$

Substitution of Equation (16) into Equation (17) gives:

$$V(\overline{P_{T_2}} - \overline{P_{T_{12}}}) \frac{S}{U} dy = \rho V \Gamma_{SS} dy - \rho V |\tilde{\Gamma}| e^{-i\left[\frac{2\pi}{\ell}(y + x\tan\alpha_2) - \phi_{TE}\right]} dy \ . \qquad (18)$$

And finally,

$$\overline{P_{T_2}} = \overline{P_{T_{12}}} + \frac{\rho U \Gamma_{SS}}{S} - \frac{\rho U |\tilde{\Gamma}|}{S} e^{-i\left[\frac{2\pi}{\ell}(y + x\tan\alpha_2) - \phi_{TE}\right]} \ . \qquad (19)$$

Equation (19) is the final expression for the time-mean total pressure at the exit of the rotor whose blades experience unsteady forces and circulation. It is the same result as that obtained by Horlock and Daneshyar in Reference [19] from a vortex analysis if, assuming as they did, $\phi_{TE} = 0$. Thus, it is seen from Equation (19) that as the flow is transported through the moving blades, three time-mean total pressure fields are superimposed to give the time-mean total pressure, $\overline{P_{T_2}}$, which is recorded by a total pressure probe located downstream of the blades. The first term of Equation (19) represents the upstream disturbance field which is transported through the blades with the circumferential-mean or steady flow, and it is given by Equation (8); the second term represents the steady total pressure rise which arises due to the steady lift on the blades and is uniform in the direction of blade motion; the third term represents the time-mean total pressure due to the unsteady circulation on the blades.

2.2 Solution of the Problem

In the previous section, Equation (19) was derived which predicts theoretically the time-mean total pressure downstream of a rotating blade row. The equation was found to be a function of the type of disturbance entering the rotor and the geometric and operating variables of the rotor. The purpose of this section is to give an explanation of how the theoretical problem was solved and how the various operating parameters used in the solution were determined. Also, the contribution of each separate term in Equation (19) to the total solution will be shown.

First consider the time-mean total pressure distribution at the cascade inlet given by Equation (1). This total pressure distribution can be represented by a standard Fourier series as a function of θ, the circumferential measurement position, as follows:

$$\overline{P_{T_1}}(\theta) = \frac{a_o}{2} + \sum_{n=1}^{\infty} a_n \cos n\theta + b_n \sin n\theta \ . \tag{20}$$

Dividing and multiplying by the square root of the sum of the squares of the Fourier coefficients gives:

$$\overline{P_{T_1}}(\theta) = \frac{a_o}{2} + \sum_{n=1}^{\infty} \left(\frac{a_n}{\sqrt{a_n^2 + b_n^2}} \cos n\theta + \frac{b_n}{\sqrt{a_n^2 + b_n^2}} \sin n\theta \right) \sqrt{a_n^2 + b_n^2} \ . \tag{21}$$

The following definitions are made for the Fourier coefficients:

$$a_n \equiv -A_n \sin\phi_n$$

and

$$b_n \equiv A_n \cos\phi_n \ ,$$

where $A_n = \sqrt{a_n^2 + b_n^2}$ and ϕ_n is the phase angle defined as:

$$\phi_n \equiv -\tan^{-1}\left(\frac{a_n}{b_n}\right),$$

Using these definitions for a_n and b_n, Equation (21) becomes:

$$\overline{P_{T_1}}(\theta) = \frac{a_o}{2} + \sum_{n=1}^{\infty} A_n(-\sin\phi_n \cos n\theta + \cos\phi_n \sin n\theta) . \tag{22}$$

And, finally, by applying the trigonometric relation for the difference of two angles, we arrive at the following expression which describes the sinusoidal distribution of total pressure at the rotor inlet:

$$\overline{P_{T_1}}(\theta) = \frac{a_o}{2} + \sum_{n=1}^{\infty} A_n \sin(n\theta - \phi_n) . \tag{23}$$

Physically, this term is obtained from measurements of the total pressure inlet distortion without the rotor operating.

As the total pressure distortion, given by Equation (23), passes through the rotor blade row, it undergoes a further shift in phase angle due to the steady lift on the blades. The amount of phase shift due to the steady transport of a distortion through a blade row was discussed in detail in Section 2.1.1. Therefore, assuming the amplitude of the distortion is not altered, i.e., A_n = constant, the expression for the inlet distortion downstream of the rotor blade row after it has been transported through the blades with the steady flow is:

$$\overline{P_{T_{12}}}(\theta) = \frac{a_o}{2} + \sum_{n=1}^{\infty} A_n \sin\left[n\theta - \phi_n - \frac{2\pi}{\ell}(C_L + C_D \tan\beta_m)\frac{C}{2\frac{S}{C}}\right] . \tag{24}$$

The calculation of lift coefficient, C_L, was made from the following equation:

$$C_L = 2(S/C)[\tan\beta_1 - \tan\beta_2] \cos\beta_m - C_D \tan\beta_m \ . \tag{25}$$

The angles β_1 and β_2 are found from the geometry in Figure 2. β_m is then given by

$$\tan\beta_m = \frac{\tan\beta_1 + \tan\beta_2}{2} \ . \tag{26}$$

The drag coefficient, C_D, is given by:

$$C_D = \frac{\Delta P_T}{1/2\rho W_1^2} \frac{S}{C} \frac{\cos^3\beta_m}{\cos^2\beta_1} \ , \tag{27}$$

where

$$\Delta P_T = (P_T)_{ideal} - (P_T)_{actual}$$

and

$$\Delta P_T = \frac{2(V_{y_2} - V_{y_1})}{U} - \frac{(P_{T_2} - P_{T_1})}{1/2\rho U^2} \ .$$

The steady lift on the blades does not change the magnitude of the total pressure variation downstream of the rotor; it only transports the distortion in the circumferential direction. In a real physical situation, viscous effects would cause a change in magnitude. However, the theory does not account for viscous effects, so the magnitude of the amplitude of the total pressure is unchanged by the steady lift.

The second term in Equation (19) represents the steady state total pressure rise, $P_{T\ downstream} - P_{T\ upstream}$, and it is also a result of

the steady lift on the blades. This term is merely the differences in total pressure between the upstream and downstream measuring locations in a uniform flow. It does not shift the phase angle of the total pressure disturbance; it only adds to the overall magnitude of the circumferential mean value inlet distortion as it passes through the blade row.

The last term which must be considered in the solution of the time-mean total pressure at the rotor exit is the unsteady term. The unsteadiness of the total pressure distortion is represented by the magnitude of unsteady circulation and a phase angle. This phase angle, ϕ_{TE}, is referenced to the trailing edge of the blade. Henderson, in Reference [21], uses measured values of time-mean total pressure to predict the unsteady circulation and phase angle as a function of blade stagger angle, space-to-chord ratio, and reduced frequency. These predicted values of unsteady circulation and phase angle are used in the solution of the problem which is presently being discussed. It should be noted that the values of magnitude and phase angle of the circulation which are calculated from the analysis in Reference [21] are referenced to the mid-chord of the blade. The following transformation is necessary to reference the circulation and phase angle to the blade trailing edge:

$$|\tilde{\Gamma}|_{TE} = |\tilde{\Gamma}|_{MC} e^{i\omega} \quad , \tag{28}$$

$$[\tilde{\Gamma}_{real} + i\tilde{\Gamma}_{imaginary}]_{TE} = [\tilde{\Gamma}_{real} + i\Gamma_{imaginary}]_{MC} \ (\cos\omega + i\sin\omega) \tag{29}$$

and

$$\phi_{TE} = -\tan^{-1}\frac{(\tilde{\Gamma}_{imaginary})_{TE}}{(\tilde{\Gamma}_{real})_{TE}} \quad , \tag{30}$$

where ω is the reduced frequency. This phase angle, ϕ_{TE}, is measured

relative to the steady, or quasi-steady (ω=u), circulation. To express this phase angle relative to the inlet distortion, $\overline{P_{T_1}}$, it must be increased by π radians, since the steady circulation is 180 degrees out of phase with the distortion field [21]. Hence:

$$[\phi_{TE}]_{\text{distortion}} = \pi - [\phi_{TE}]_{\text{steady circulation}} .$$

An additional phase shift arises in the unsteady term which represents the amount that the distortion is convected after its passage through the rotor. This distance, $x\tan\alpha_2$, is shown in Figure 3. Therefore, the contribution to the time-mean total pressure due to the unsteady circulation on the blades is given by:

$$\tilde{P}_{T_2}(\theta) = \sum_{n=1}^{\infty} \frac{\rho U |\tilde{\Gamma}|}{S} \sin(\pi + n\theta - \phi_{TE} + \frac{2\pi}{\ell} x\tan\alpha_2) . \qquad (31)$$

The final solution of the time-mean total pressure downstream of the rotor blade row is then obtained by considering all the terms given in Equations (24) and (31) plus the steady-state total pressure rise. Equation (19) was derived in the previous section for a general case in exponential form; however, only the sine portion of the general form needs to be considered for the solution.

CHAPTER III

EXPERIMENTAL EQUIPMENT, INSTRUMENTATION, AND EXPERIMENTAL STUDIES CONDUCTED

3.1 The Axial Flow Research Fan

The entire experimental program was conducted in a facility referred to as the Axial Flow Research Fan (AFRF), which was designed and constructed at the Applied Research Laboratory, The Pennsylvania State University. This facility was designed specifically for studying the response of axial flow turbomachinery blade elements and/or a single stage to subsonic incompressible unsteady flows of the type encountered in practice. Thus, the overall dimensions of the test rotor and the remainder of the facility were made sufficiently large so that the blades could be instrumented or flow surveys could be made with few spatial limitations. Figure 4 is a sketch of the AFRF which shows the important components and some overall dimensions of the facility. A highly detailed description of the system is given in Reference [34].

The AFRF can most simply be described as a subsonic, incompressible, open circuit wind tunnel with an annular cross section. The facility has a hub radius of 4.75 inches (12.1 cm), a hub-to-tip radius ratio of 0.442, and was designed to operate in the total pressure ratio range from 1.0 to 1.1. The overall length is 19.67 feet (6.0 m) and consists of an annular flow passage bounded at one end by a bellmouth inlet and at the other end by an exhaust throttle. The facility can be operated with axial velocities up to 112 ft/sec (34.14 m/sec) with test rotor speeds up to 320 ft/sec (97.54 m/sec). The forward region, from the inlet to a point just upstream of the test rotor blade drive motor, is bounded by a 9.5 inch (24.13 cm) diameter cylindrical hub surface and a 21.5 inch (54.6 cm)

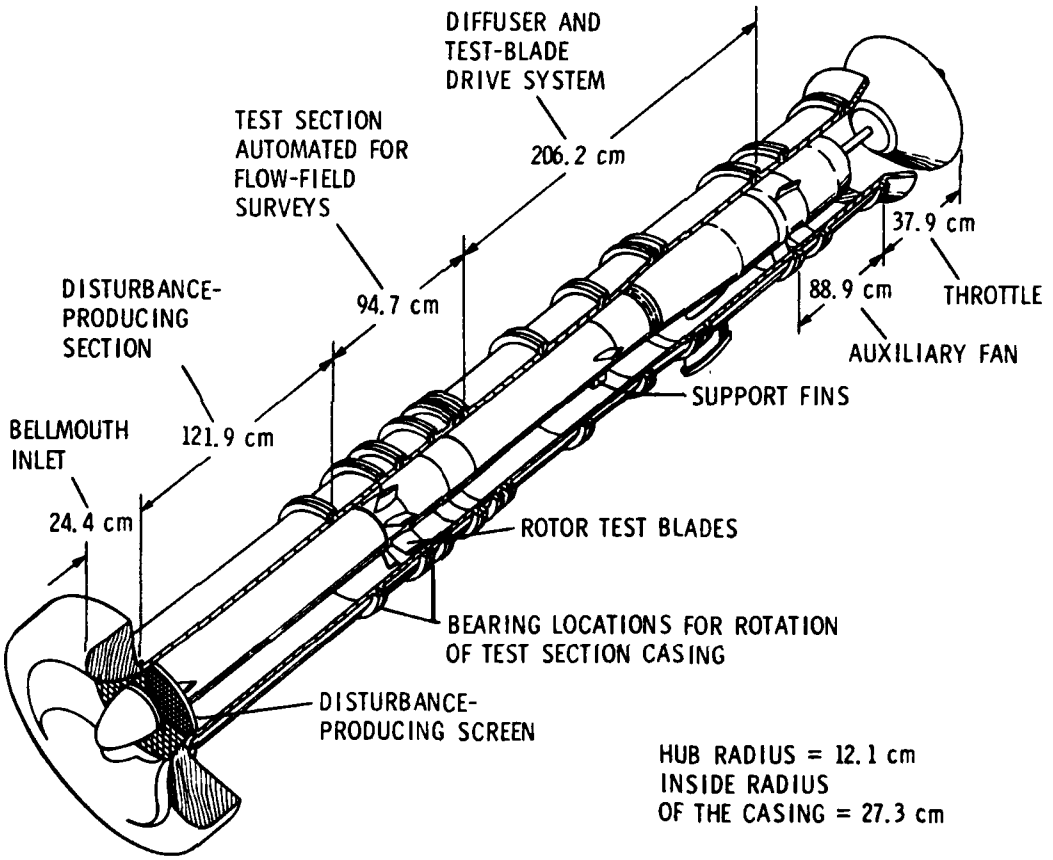

Figure 4. The Axial Flow Research Fan

inside diameter cylindrical outer casing. The drive unit for the rotor is a 70 horsepower (52.2 kw) motor enclosed in the hub of the AFRF. The auxiliary fan drive motor and the rotor blade drive motor can be independently regulated at any speed up to 3400 rpm through the use of two Borg-Warner Model No. BW1200 Solid State Adjustable Frequency Drive inverter units. This gives a maximum relative blade tip Mach number of 0.338. The airflow through the facility is controlled by the auxiliary axial flow fan and the throttle arrangement provided at the exit of the facility. With a zero steady lift rotor of the type being used in the initial research experiments, the final adjustment of the throughflow velocity can be produced either by adjusting the auxiliary fan rpm with a fixed throttle setting, or by adjusting the throttle position with the auxiliary fan operating at a fixed speed.

The disturbance generating section is housed in the two 24-inch (61.0 cm) long outer casing segments positioned immediately downstream of the bellmouth inlet. This 48-inch (122.0 cm) long flowpath was provided to permit the development of distorted flowfields. In the absence of the disturbance producing screens, the inlet of the facility was designed to provide a steady uniform flow to the annulus. For studies involving distorted flow, screens are placed in the inlet which produce sinusoidal or square circumferential variations of total pressure. These disturbance generating screens of the type shown in Figure 5 provide a capability to carry out experiments at reduced frequencies from 0.27 to 2.46, based on the mid-span radius, a chord length of six inches, and an inlet relative flow angle of 45 degrees. The design and performance evaluation of these screens is presented in Reference [35]. Immediately downstream of the screens, as shown by Figure 4, is a section of the

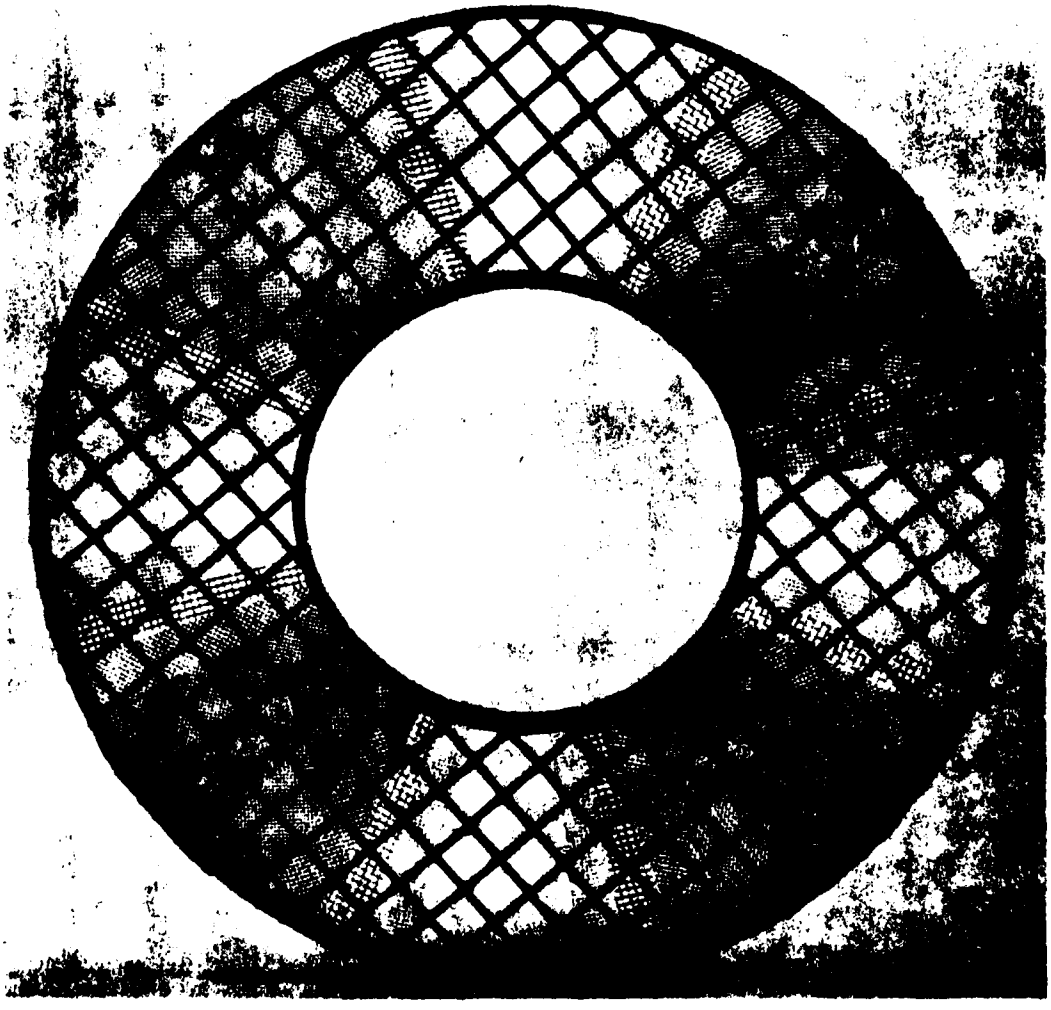

Figure 5. Four-Cycle Disturbance Producing Screen

annulus which serves as a settling section where small velocity variations and the static pressure gradient are removed. The section between the screen and test rotor also isolates the rotor from the screen. This is very important, since a rotor will strongly alter the upstream flow in the immediate vicinity of the rotor.

The section just downstream of the settling section contains the test rotor-stator stage. An important feature of the facility with regard to this investigation is the ability of the outer casing surrounding the rotor-stator stage to be rotated freely about the AFRF centerline. Rotation of the casing is accomplished by electrically turning a wheel driven worm gear, and it is automatically controlled by the data acquisition system. The worm gear is driven by a 1800 inch-ounce (130 cm-kg) torque Slo-Syn Type SS1800-1007 motor which is controlled by a Slo-Syn Preset Indexer. This feature is provided to enable circumferential surveys of the flow to be performed by rigidly attaching instrumentation to the casing and indexing the casing in preselected increments.

The AFRF design utilizes split outer casing and hub sections both upstream and downstream of the stator. By interchanging sections of different lengths, it is possible to move the stator blade row relative to the rotor blade row. Tests with rotor-stator axial spacings, rotor trailing edge to stator leading edge, of 3, 6, 9, or 12 inches (i.e., 7.62, 15.24, 22.86, or 30.48 cm) are possible. For six-inch (15.24 cm) chord blades, these dimensions correspond to non-dimensional rotor-stator spacings from 0.5 to 2.0 blade chord lengths.

To determine the influence of rotor geometrical parameters on the unsteady rotor response, two rotor configurations were employed in this investigation. The first configuration consisted of a zero lift,

uncambered rotor which was designed to produce a zero circumferential-mean total pressure rise at its design operating condition in a uniform flow. The rotor was designed with this criterion primarily to enable accurate comparisons to be made with unsteady cascade theories which are usually restricted to zero or lightly loaded blades. The characteristics of the zero steady lift test rotor are shown in Figure 6. For the tests conducted in this study, the rotor was used in its six-bladed configuration. The second rotor configuration employed in the tests consisted of a nine-bladed cambered rotor with a fixed number of blades and fixed stagger angle. Both the zero lift, uncambered rotor and the lifting, or cambered, rotor were designed with identical blade thickness distribution, chord length, and blade span. The characteristics of the cambered rotor are shown in Figure 7.

For the tests conducted in this study, the zero steady lift rotor was assembled with six blades, which results in a space-to-chord ratio of 1.35 at the mean radius. Variations in blade stagger angle were achieved by rotating the blades in the hub and by using different hub spacer blocks. In addition to the nominal 45 degree stagger angle for which the blades are designed, stagger angles of 35 degrees and 55 degrees at the mean radius were also evaluated. Operation at these stagger angle settings produces an off-design condition which will result in three-dimensional flow effects. However, the deviation of the blade angle from a design based on that particular stagger angle is not large. Thus, the three-dimensional effects should be small and the flow is still justifiably considered as two-dimensional at the mean radius. The data that was measured in the present investigation using the six-bladed rotor in its 35 and 55 degree stagger angle configurations show that the

ZERO STEADY LIFT ROTOR

- DESIGNED TO EVALUATE UNSTEADY PRESSURES, LIFT, AND MOMENT WITH AND WITHOUT STEADY LIFT AND MOMENT

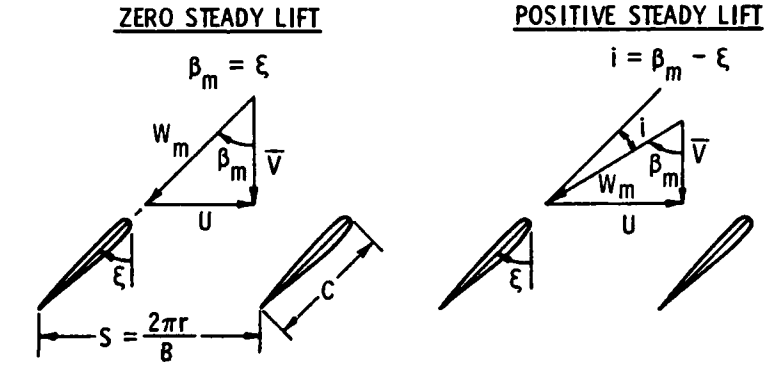

- DESIGN BASED ON THE RELATION

$$\xi = \beta_m = \tan^{-1}(U/\bar{V})$$

WITH

$\xi = 45^0$ AT $r = r_m$

- UNCAMBERED 10% THICK CI PROFILE
- BLADE CHORD (C) = 6.0 INCHES (15.24 cm)
- BLADE SPAN = 5.9 INCHES (14.98 cm)
- NUMBER OF BLADES (B) = 6 OR 12
- SPACE-TO-CHORD RATIOS (S/C) = 4.06, 2.71, 2.03, 1.35, 0.90 OR 0.68
- STAGGER ANGLE (ξ) = 35, 45, OR 55 DEGREES

Figure 6. Characteristics of the Uncambered, Zero Steady Lift Rotor

CAMBERED ROTOR

- DESIGNED TO INVESTIGATE UNSTEADY PRESSURES, FORCES, AND MOMENTS WITH NONZERO STEADY FORCES AND MOMENTS

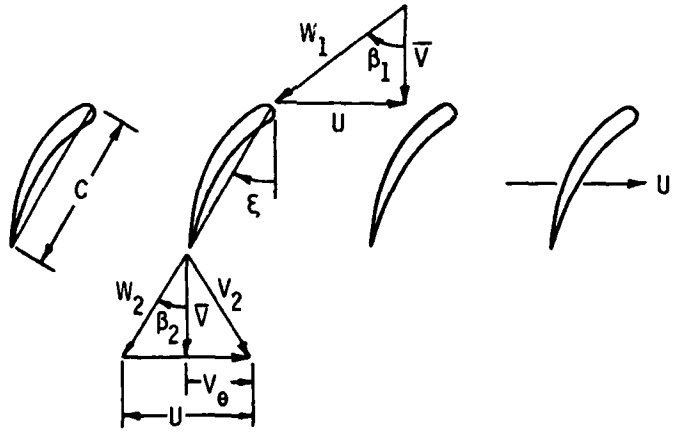

- DESIGN BASED ON LIEBLEIN'S METHOD (NASA SP-36) FOR CIRCULAR ARC MEAN LINES
- FREE-VORTEX LOADING WITH RV_θ = 25 ft^2/sec (2.32 m^2/sec) WITH $\bar{V}$ = 80 ft/sec (24.4 m/sec)
- NUMBER OF BLADES = 9 (S/C = 0.90 AT MEAN RADIUS)
- STAGGER ANGLE (ξ) = 50 deg
- PROFILE, CHORD, AND SPAN IDENTICAL TO ZERO STEADY LIFT ROTOR

Figure 7. Characteristics of the Cambered Rotor

fluctuations (i.e., the local peak values) of radial velocity were less than ten percent of the free-stream velocity. Thus, the assumption of two-dimensional flow at the mean radius is valid.

Downstream of the test rotor-stator stage is another section of the annulus which isolates the rotor from the effects of the auxiliary fan and throttle. As mentioned previously, the mean axial velocity through the facility is controlled by the speed of the auxiliary fan. The test rotor is driven by the 70 horsepower motor, so that control of the test rotor rpm setting is independent of the auxiliary fan rpm setting. By increasing the test rotor RPM while making minor adjustments to the auxiliary fan rpm setting to maintain the mean flow velocity at a constant value, it is possible to vary the flow incidence on the test rotor blades. The test rotor can thus be operated with an off-design incidence resulting in a steady load on the blades. This enables the facility to be used to investigate the effects of incidence, or steady loading, ranging all the way to stall, or the unsteady response of the blade row.

3.2 Instrumentation

In many complex flow fields such as those encountered in turbomachines, the experimental determination of the three-dimensional characteristics of the flow field is frequently required. If space limitations or other considerations make nulling techniques impractical, five-hole probes in a non-nulling mode can be employed for measurements in low speed, incompressible flows. In this program, the approach taken to measure the response of the rotor was to take time-mean flow measurements upstream and downstream of the rotor. To make these measurements, two five-hole pressure probes were used in the non-nulling mode. Five-hole probes were selected for the measurements because they enable the total pressure,

static pressure, and axial, circumferential, and radial components of velocity to be determined. The probes employed were commercially available United Sensor prism type probes. The geometry of this type of probe offers easy insertion and mounting of the probe in the AFRF. An enlarged sketch of the sensing element and a sketch of the entire probe showing its dimensions is presented in Figure 8. The probes were positioned at stations referred to as 1-D and 15, axially located 0.137 rotor blade chord length upstream of the rotor and 0.820 chord length downstream of the rotor at the mean radius, respectively. The probes used in this investigation were calibrated in a known flow field by Yocum. A brief description of the procedure used in the calibration of these probes is presented here for the sake of completeness.

The five-hole probes employed in the experimental program were used in a non-nulling mode, which means that they had a fixed orientation with respect to the casing during the tests. This means that relationships must be determined between the measured pressures at the five holes and the true, local total and static pressure or velocity. These desired relationships are usually expressed as dimensionless pressure coefficients, which are functions of the flow angularity.

For operation in the non-nulling mode, the calibration characteristics must include data that represent pressure differences in both the pitch and yaw planes, see Figure 9, as well as differences between the measured and the true local total and static pressures. The pressure coefficients representing these data must be defined so that they are independent of velocity and are a function only of the flow angularity.

Referring to Figure 9, the dimensionless yaw, pitch, total pressure, and static pressure coefficients are defined as follows:

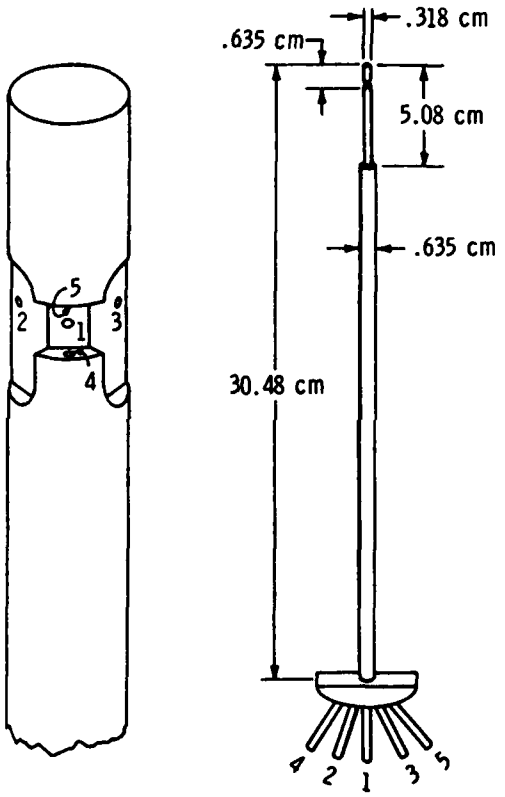

Figure 8. Five-Hole Pressure Probe

GEOMETRY OF THE PRISM PROBES

VECTOR RESOLUTION FOR A PROBE
CALIBRATED IN THE PITCH-YAW MODE

$V_x = \bar{V} \cos\alpha \cos\beta$

$V_R = \bar{V} \sin\alpha$

$V_\theta = \bar{V} \cos\alpha \sin\beta$

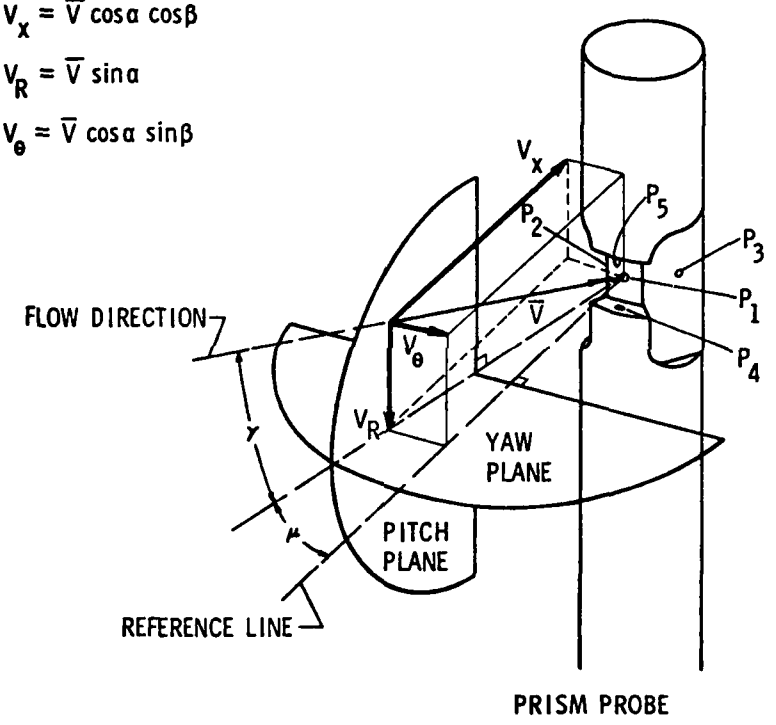

Figure 9. Geometry of the Prism Probes

$$C_{P\ yaw} = \frac{P_2 - P_3}{P_1 - \overline{P}} ,$$

$$C_{P\ pitch} = \frac{P_4 - P_5}{P_1 - \overline{P}} ,$$

$$C_{P\ total} = \frac{P_1 - P_{total}}{P_1 - \overline{P}} ,$$

and

$$C_{P\ static} = \frac{\overline{P} - P_{static}}{P_1 - \overline{P}} ,$$

where $$\overline{P} = \frac{P_2 + P_3 + P_4 + P_5}{4} ,$$

P_1 = pressure measured at the central probe hole,

P_2 and P_3 = pressures measured in the yaw plane,

and

P_4 and P_5 = pressures measured in the pitch plane.

These coefficients, which are a function of the yaw and pitch angles, completely describe the response of the probe to the flow.

The two flow angles and the true total and static pressures are calculated from the five pressures measured from the probe through the use of a detailed calibration. The probes were calibrated in air with the use of an open jet facility. To conduct the calibration of a given probe, the test velocity was maintained at a constant value. The calibration range was ±30 degrees in both the yaw and pitch planes. The probe was positioned at one of the predetermined pitch angles and then moved in prescribed increments through the yaw angle range. The pitch angle was then changed, and the probe was again moved through the yaw angle range. At each calibration point, the five pressures from the probe as well as

the known total and static pressure of the flow were recorded and then processed on an IBM 1130 computer. The data reduction program calculated the four previously defined pressure coefficients, the test section velocity, and the Reynolds number based on the probe tip diameter. Each probe was calibrated three times to verify the repeatability of the results. To reduce deviations in the calibration data, the results were averaged. All calibration data were repeatable to within two percent of the reference dynamic pressure when subjected to recalibration [36]. These data consistently described the response of a particular probe, and thus permit the successful application of five-hole probes in a non-nulling mode.

With all of the above information known, when the probe is placed in an unknown flow, the yaw and pitch angles of the unknown flow can be determined through the use of the calibration data. After the two angles are known, the total and static pressure coefficients are interpolated from the calibration data and the two pressures can then be calculated. The velocity is calculated with the Bernoulli equation and then resolved into its axial, circumferential, and radial components using the known flow angles. The derivation of the three velocity components as well as the resolution of the flow angles for the cases where the probe was rotated in the yaw plane are presented in Appendix A.

Meaningful calibration data should be independent of the measured quantities. In most five-hole probe applications, velocity is the primary parameter to be measured. It turns out that the calibration curves of a five-hole probe are usually weakly dependent on velocity or Reynolds number. Therefore, the effects of Reynolds number variations were assessed by calibrating the five-hole probes in air over a Reynolds

number range of 2000 to 7000. The results of these tests showed that the total pressure, pitch coefficient, and yaw coefficient were essentially unaffected by the Reynolds number variation [36]. On the other hand, a measurable change in the static pressure coefficient was observed. However, average correction factors were incorporated into the data reduction procedures to account for these variations in the static pressure coefficient for the range of Reynolds numbers that the probe would experience. The correction could be neglected in most cases with the error in the resulting velocity being approximately two percent. The correction was included, however, to increase the accuracy of the results.

The accuracy of the measurements made with the five-hole probes was checked by comparing the results with data obtained using other types of instrumentation. In the absence of the rotor, static pressure gradients do not exist far downstream of the distortion producing screen. Circumferential surveys of the flow in the AFRF can be conducted using a Kiel probe to measure total pressure and a wall tap in the casing to measure static pressure. The velocity measured in this manner was compared with data obtained with the five-hole probes. The agreement was found to be very good, which demonstrated the validity of the five-hole probe measurements and data reduction [37].

The accuracy of the probes in the non-nulling mode, as compared with the nulling mode, was also checked to assure that in the non-nulling mode the probe did not miss any of the details of the flow. For this check, measurements were made with the probe nulled in the plane perpendicular to its axis and the results were compared with the results obtained in the non-nulling mode. Once again the agreement was found to be quite good.

A schematic sketch showing the entire experimental system is presented in Figure 10. The ten pressure outputs from the five-hole pressure probes were directly connected by flexible Tigon tubing to a scanivalve. Channels 1 through 5 on the scanivalve read the pressure differences from the upstream or location 1-D probe, and channels 6 through 10 read the output from the downstream or location 15 probe. Channel 11 was connected to a wall static pressure tap in the outer casing of the AFRF located in the settling section of the facility, and it read the static pressure in the axial plane of measurement. Each channel was recorded individually and then automatically advanced through the use of an automatic control on the scanivalve. The scanivalve output was directly fed into a Validyne Model DP15 strain gaged differential pressure transducer. This transducer, using the ambient pressure as its reference, produced an electrical signal proportional to the difference between the probe time-mean total pressure and the ambient pressure. The electrical signal was carried, as shown schematically in Figure 10, through a Validyne Model CD15 Carrier Demodulator, a laboratory-constructed integrating digital voltmeter and data logger, and finally presented as a voltage output on punched paper tape. The paper tape output was then interpreted and analyzed on an IBM 1130 computer.

Before conducting measurements in the AFRF, the data sensing and recording system was calibrated to determine its voltage output as a function of the applied pressure differential. The calibration was conducted using the Validyne pressure transducer and carrier demodulator, an integrating digital voltmeter, and a Meriam Co. Micromanometer. With the micromanometer, a range of applied pressures, readable to 0.001 inch of water, was applied to the system, and the corresponding voltage output

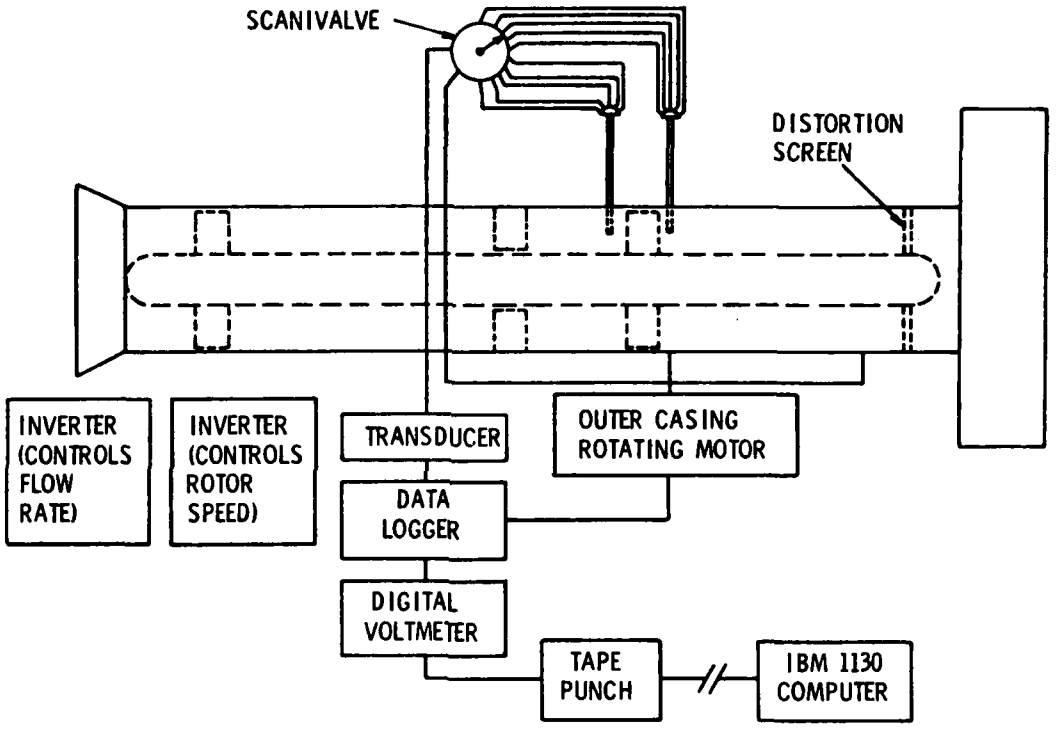

Figure 10. Schematic of Test Apparatus

was recorded. Figure 11 presents the results of this calibration and determines the voltage output per inch of water for the particular transducer employed in the experimental tests. The calibration slope defined the transducer constant which was then used in the computer analysis of the data. Shown in Figure 11 are two independent calibrations of the transducer conducted over a six-week period. These two calibrations yielded values of transducer constants which differed by 0.2 percent, thus demonstrating the repeatability of the pressure sensing system.

In addition to the pressure measurements, it was necessary to measure the rotational speed of the rotor. A conventional system employing a slotted disc rotating with the rotor, a light source, a photocell, and an electronic counter in the data acquisition system was used for this purpose. With sixty slots in the disc and a one-second sample period, the counter reading gave the rpm of the rotor directly and displayed it on the data logger.

3.3 Experimental Studies Conducted

In order to determine the influence of rotor geometrical parameters on the unsteady rotor response, two rotor configurations were employed in this investigation. The two test rotors used in the program were a zero lift, uncambered rotor which has variable solidity and stagger angle, as shown in Figure 6, and a lifting, or cambered, rotor with a fixed number of blades and stagger angle, as shown in Figure 7.

For each geometrical configuration of the test rotor, a test was conducted which involved the measurement of the steady performance of the rotor with uniform inlet flow. This information was necessary if the performance degradation caused by the flow distortions was to be determined. To determine the rotor performance, flow measurements were made

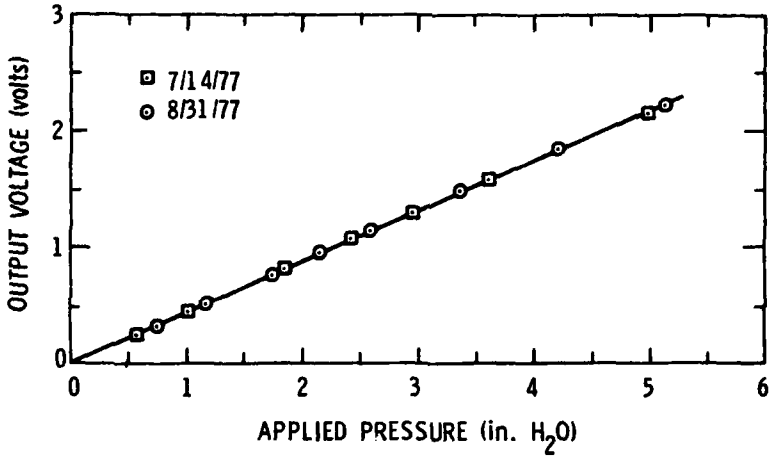

Figure 11. Two Independent Calibrations of the Pressure Transducer

upstream and downstream of the rotor over a range of flow coefficients. Incidence angles ranging from negative ten degrees up to the point where stall began were evaluated. The performance measurements were made at the mean radius, since the circumferential surveys of the distorted flow were made at the mean radius and the flow is assumed to be two-dimensional throughout the study.

The effects of rotor solidity (i.e., chord-to-spacing ratio) were studied using the zero lift rotor in its six-bladed configuration. These data can be compared to the results from the rotor in its twelve-bladed configuration obtained by A. M. Yocum in Reference [37]. For the six-bladed test rotor, stagger angle values of 35, 45, and 55 degrees were tested. At each of these stagger angles, experiments were made using the four- and six-cycle sinusoidal distortion screens and the 90 degree and 180 degree square wave distortion screens. The original intention was to test three values of blade loading for each stagger angle and distortion screen. The three blade loadings were to correspond to the design point, i.e., zero incidence angle, the condition of zero total pressure rise ($= \Delta P_T/1/2\rho U^2$), and a condition nearing stall. For the twelve-bladed rotor configuration, it was found that a zero total pressure rise requires a small positive incidence so that the pressure loss due to the viscous effects is balanced by the energy input by the rotor. However, the steady-state performance evaluations on the six-bladed rotor revealed that the conditions of zero incidence and zero total pressure rise were very nearly identical. This is due to the fact that the rotor with only six blades does not experience as large a total pressure loss as the twelve-bladed rotor.

Figure 12 shows a sample of the procedure used to determine the various operating conditions for the six-bladed rotor. The values used

V_X = axial velocity

U_m = rotor blade speed at mean radius

β_1 = inlet air angle

ξ = stagger angle

i = incidence angle

r_m = mean radius = 7.75 in.

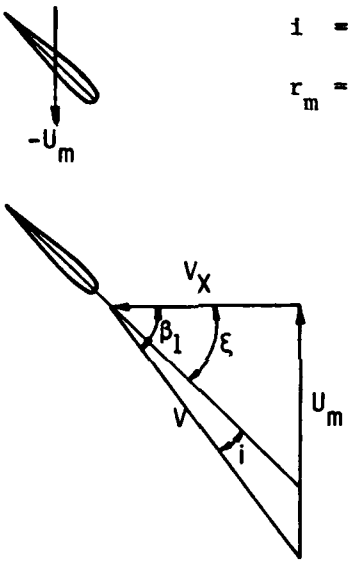

Known:

Four-cycle distortion screen → V_X = 65.911 ft/sec

Stagger angle = 45 degrees

Desired incidence angle = 8 degrees

Calculate Rotor RPM:

$\tan(\xi+i) = U_m/V_X$

$U_m = V_X \tan(\xi+i) = (65.911 \text{ ft/sec}) \tan 53 \text{ degrees}$

$U_m = 87.47$ ft/sec

$$RPM = \frac{(87.47 \text{ ft/sec})(12 \text{ in./ft})(60 \text{ sec/min})}{(2\pi \text{ rad/rev})(7.75 \text{ in./rad})}$$

RPM = 1293

Figure 12. Calculation of Test Conditions for the Six-Bladed Uncambered Rotor

for the axial velocity are circumferential-mean values which were determined by Yocum [37]. They were determined by making circumferential surveys of the distorted flow in the absence of the rotor. Thus, a value for the axial velocity was predetermined for each distortion screen used. Next, the desired value of circumferential mean incidence angle was selected. Then, by knowing the axial velocity, incidence angle, and stagger angle a value of blade speed at the mean radius is calculated and converted to revolutions per minute. This rotor rpm was the variable parameter which defined the different operating conditions for the six-bladed rotor.

A tabulated summary of the test conditions which were conducted with the six-bladed, non-lifting rotor appears in Table B.1 of Appendix B. Presented are the type of distortion tested, the stagger angle of the blades, the rotor rpm, the average flow coefficient, V_X/U_m, based on the blade speed at the mean radius, the average pressure rise coefficient, $\Delta P_T/1/2\rho V_X^2$, and a circumferentially averaged value of incidence angle at the rotor mean radius.

The next series of experiments performed in this investigation utilized a cambered test rotor with nine blades and a fixed stagger angle of 50 degrees at the mean radius. Essentially two effects were studied with the cambered rotor. First of all, the effect of rotor-stator spacing on the response of the rotor was examined. Eight cambered stator blades of the same design as the rotor blades were installed in the Axial Flow Research Fan for this purpose. In the first series of tests, the stator blade row was located twelve inches (30.48 cm), or two rotor blade chord lengths, downstream of the rotor trailing edge. Then, to look at the effects of rotor-stator spacing, another series of tests was performed

using the same operating conditions as in the first series. However, for these tests, the stator row was moved to a position three inches (7.62 cm), or one-half blade chord length, downstream of the rotor trailing edge. For all of the tests just mentioned, the one-, two-, four-, and six-cycle sinusoidal distortions and the 90 degree and 180 degree square wave distortions were used. Three values of blade loading, one at the design point, one below design, and one above design, were evaluated.

The final series of tests with the cambered rotor studied the effect of spanwise location on the inlet distortion, that is, to see what the distortion flow field looks like at radial locations other than the mean radius of the rotor blades. Four radial locations were tested; two locations were between the hub and the mean radius, and two were between the mean radius and the tip of the blade. At each radial location, the two- and four-cycle sinusoidal distortions and the 90 degree and 180 degree square wave distortions were tested, and only one incidence angle was used. A tabulated summary of the operating conditions used for all the tests conducted with the nine-bladed cambered rotor appears in Tables B.2 through B.7 of Appendix B.

It should be noted that a slightly different approach was used to determine the operating conditions for the cambered rotor as opposed to the zero lift rotor. Figure 13 shows the method used to determine the blade loadings used for the tests on the cambered rotor. In the tests with the non-lifting rotor, the values of incidence angle to be used were selected from the steady performance data, and the rotor rpm was then calculated. But for the cambered rotor, values of flow coefficient, V_X/U_m, were selected from the steady performance data. Then, by knowing the value of axial velocity, V_X, to be used for each distortion screen, the rotor rpm was calculated to give the proper flow coefficient.

V_X = axial velocity

U_m = rotor blade speed at mean radius

β_1 = inlet air angle

β_1' = inlet blade angle

ξ = stagger angle

i = incidence angle

r_m = mean radius = 7.75 in.

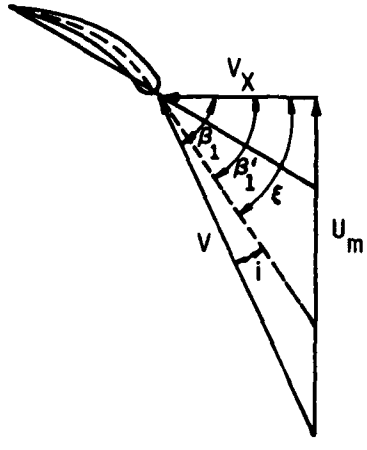

Known:

Two-cycle distortion screen → V_X = 67.533 ft/sec

Desired flow coefficient = 0.586

Calculate Rotor RPM:

$$V_X/U_m = \frac{67.533 \text{ ft/sec}}{U_m} = 0.586$$

$$U_m = 115.24 \text{ ft/sec}$$

$$\text{RPM} = \frac{(115.24 \text{ ft/sec})\ (12 \text{ in./ft})\ (60 \text{ sec/min})}{(2\pi \text{ rad/rev})\ (7.75 \text{ in./rad})}$$

RPM = 1704

Then,

$$\tan (\beta_1' + i) = U_m/V_X = (1.706)$$

$$i = \tan^{-1} (1.706) - 56 \text{ degrees}$$

i = 3.623 degrees

Figure 13. Calculation of Test Conditions for the Nine-Bladed Cambered Rotor

CHAPTER IV

EXPERIMENTAL RESULTS AND DISCUSSION

4.1 Rotor Steady Performance

When describing the performance of an axial flow fan or compressor in a uniform inflow, the performance characteristic of primary interest is the relationship between the pressure rise and the inlet flow conditions and rotor speed. For an incompessible flow, this desired relationship is adequately described by relating the total pressure rise coefficient, Ψ, defined as $(P_{T\ exit} - P_{T\ inlet})/1/2\rho U^2$ to the flow coefficient, Φ, defined as V_X/U.

For a flow with a zero circumferential velocity component upstream of the rotor, and assuming there are no losses, a relationship is described between Ψ and Φ from Euler's pump equation. This equation, which shows a direct relationship between Ψ and Φ, is as follows:

$$\Psi = 2 - 2\Phi\tan\beta_2 . \tag{32}$$

For a particular rotor configuration, β_2 will depend on the flow incidence and thus will also be related to the flow coefficient, Φ. Furthermore, the losses through the blade row, which are neglected in Equation (32), will depend primarily on the incidence or the flow coefficient. For these reasons, Ψ is expected to be a function of Φ alone, which justifies expressing the rotor performance in terms of the total pressure rise coefficient and the flow coefficient [37].

The experimental data of Ψ versus Φ measured at the mean radius is shown in Figure 14 for the six-bladed, zero steady lift rotor configurations having blade stagger angles of 35, 45, and 55 degrees, and

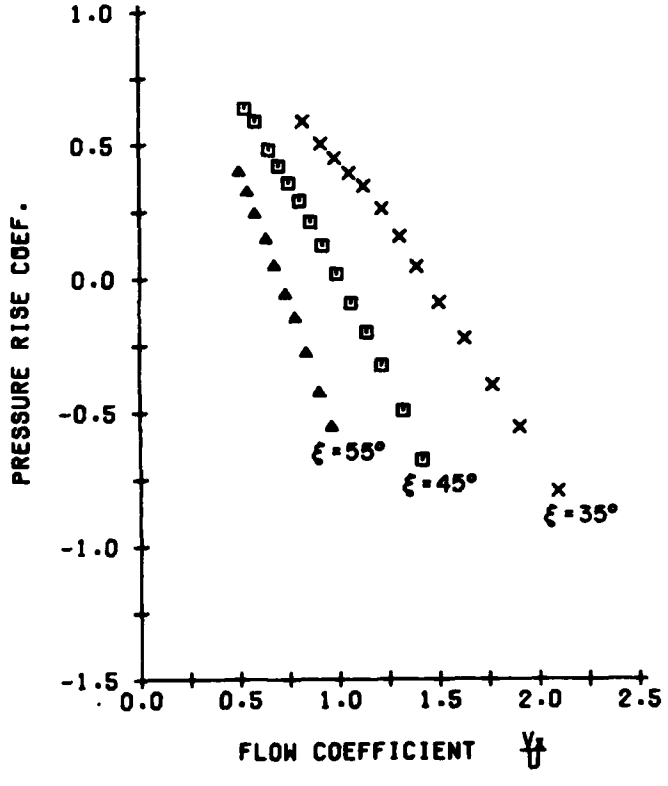

Figure 14. Steady Performance Data Measured at the Mean Radius for the Six-Bladed Uncambered Rotor

Figure 15 shows the data for the cambered rotor configuration having a fixed stagger angle of 50 degrees. For these data, which determine the steady performance of the rotors, the flow rate was set to give an average axial velocity of 67 ft/sec (20.4 m/sec). This was done to enable the probes to operate in approximately the same Reynolds number range at all times. Measurements were made only at the rotor mean radius. The rotor blade speed was then adjusted to give a range of incidence angles in two degree increments from negative ten degrees up to the point where the rotor began to stall. This range of incidence angles, and thus flow coefficients, was sufficient to completely describe the steady performance characteristics of the two rotors.

An important characteristic of the data presented in Figures 14 and 15 is the slope of the curves. In a distorted flow field, the distorted and undistorted sectors of the flow field have different axial velocities, and, thus, operate at different values of flow coefficient. From Figure 14, it can be seen that the distorted and undistorted sectors experience different amounts of total pressure rise (the distorted sector would see a higher total pressure rise than the undistorted sector). Therefore, from a quasi-steady viewpoint the slope of these curves determines the attenuation of a total pressure distortion. It is seen from Figure 14 that the slope of the performance curves becomes steeper, i.e., more negative, with increasing stagger angle for the uncambered rotor. This result can be expected by examining Equation (32). By assuming that β_2 is constant and differentiating Equation (32), it is found that $\frac{d\Psi}{d\Phi} = -2\tan\beta_2$. For the rotor with no camber, except for a small deviation angle, β_2 is approximately equal to the stagger angle and, therefore, $\frac{d\Psi}{d\Phi}$ will become more negative with higher stagger angles. This does not hold true, however, for the case of the cambered rotor. It is observed from Figure 15

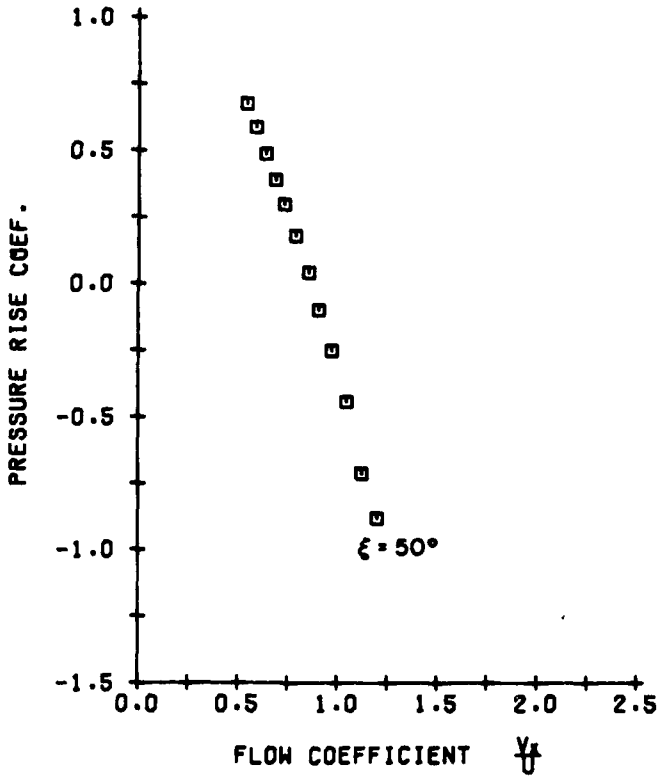

Figure 15. Steady Performance Data Measured at the Mean Radius for the Nine-Bladed Cambered Rotor

that the slope of the curve for the cambered rotor with a stagger angle of 50 degrees is more negative (steeper) than the slope of the curve for the uncambered rotor with a stagger angle of 55 degrees. For the cambered rotor, the exit blade angle, β_2, and the stagger angle are no longer approximately equal. In fact, for the nine-bladed cambered rotor used in this investigation, the angle β_2 is equal to 56 degrees. This accounts for the steeper slope for the cambered rotor despite its smaller stagger angle, and the expected result seen from the differentiation of Equation (32) is still valid.

The next important concideration to be made from the steady performance data is the amount of swirl put into the flow by the rotor. This circumferential component of velocity, or swirl, is important because it allows the energy added to the flow by the rotor, or the ideal total pressure rise, to be calculated. The ideal total pressure rise is required to determine the total pressure losses across the rotor.

In Figures 16 and 17, experimental values of $V_{\theta\ exit}/U$ measured at the mean radius are presented as a function of flow coefficient, V_X/U, for the uncambered and cambered rotors, respectively. It is observed from Figures 16 and 17 that the data are almost perfectly linear. This linear nature is not surprising, however, since the flow through a blade row usually leaves nearly tangent to the blade trailing edge (except for a small deviation angle), unless large blade loadings cause flow separation. With the flow leaving the blades at a constant relative angle, it can easily be shown that the swirl should vary linearly with flow coefficient. At low values of flow coefficient which correspond to large blade loadings, a slight deviation from the linear behavior of the curves is seen in Figures 16 and 17. This is the point at which the rotor begins

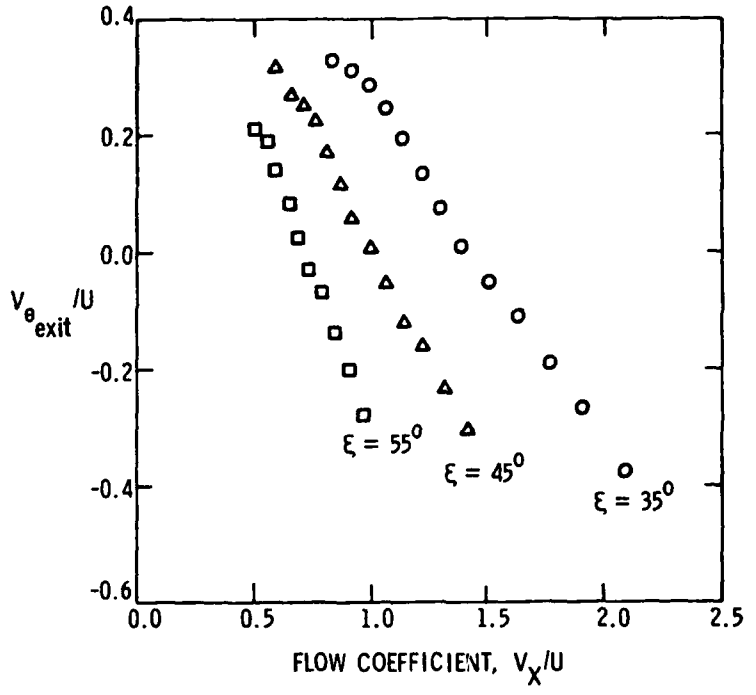

Figure 16. A Comparison of $V\theta_{exit}/U$ versus V_X/U Obtained Experimentally in Uniform Flow at the Mean Radius for the Uncambered Rotor

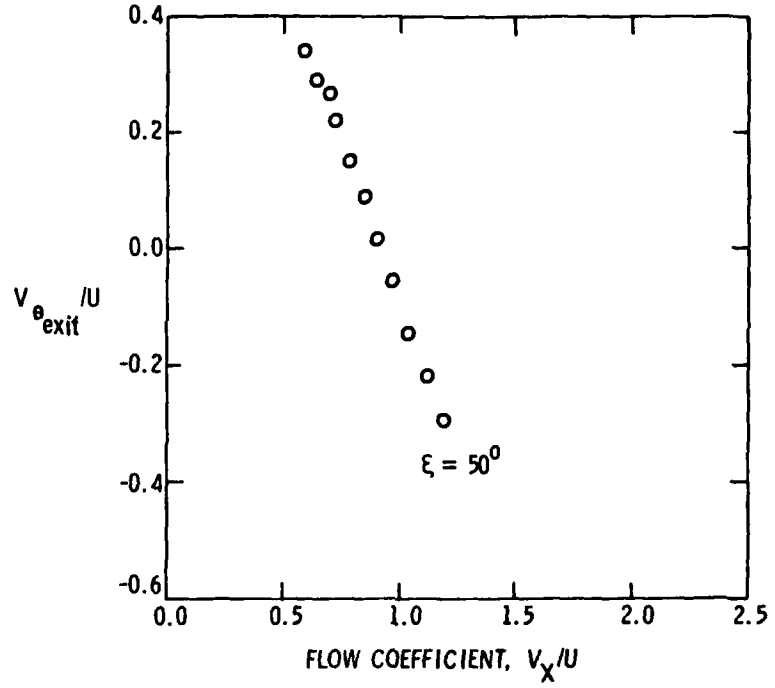

Figure 17. A Comparison of $V_{\theta\ exit}/U$ versus V_X/U Obtained Experimentally in Uniform Flow at the Mean Radius for the Cambered Rotor

to operate in the stall region and local flow separation on the blades begins to occur.

To complete the study of the steady performance of the rotors, the data of the ideal and actual total pressure rise must be interpreted. From these data the total pressure losses are also obtained. The steady losses are needed not only to evaluate the rotor performance in a uniform flow, but are also needed as a reference to evaluate the losses associated with the distorted flow. The ideal total pressure rise is obtained from Euler's pump equation and is expressed non-dimensionally as follows:

$$\Psi_{ideal} = \frac{\Delta P_{T\ ideal}}{1/2\rho U^2} = \frac{2(V_{\theta\ exit} - V_{\theta\ inlet})}{U} . \qquad (33)$$

As stated previously and as seen from Equation (33), the ideal total pressure rise is a measure of the energy added to the flow by the rotor, and it depends upon the amount of swirl put into the flow by the rotor. Upstream of the rotor, the inlet flow has no angular momentum, and, therefore, has no component of circumferential velocity or swirl. Therefore, the inlet component of circumferential velocity was assumed to be zero in the calculations of ideal total pressure rise from Equation (33). In reality, since the upstream probe is located very close to the leading edge of the rotor, there is a small component of circumferential velocity observed at the upstream location which is induced by the rotor. However, for the calculations of ideal pressure rise, this small value of inlet swirl is assumed to be zero.

The actual pressure rise coefficient, Ψ, is simply the difference between the total pressures measured upstream and downstream of the rotor. The difference between the ideal and actual pressure rise represents the

total pressure losses across the rotor. A loss coefficient, $C_{P_{t\ loss}}$, is defined in this manner as it is expressed in the following equation:

$$C_{P_{t\ loss}} = \frac{\Delta P_{T\ ideal} - \Delta P_{T\ actual}}{1/2\rho U^2} = \Psi_{ideal} - \Psi \ . \qquad (34)$$

The value of loss coefficient must necessarily be greater than zero since the ideal pressure rise represents the highest value of pressure rise which can be achieved for the given operating conditions, since any losses across the rotor are neglected. However, it was initially found that in some cases of the cambered rotor losses, the actual total pressure rise coefficient exceeded the ideal total pressure rise coefficient. After a thorough investigation of the data, the problem was determined to be in the components of the measured circumferential velocity which were used to determine the ideal pressure rise coefficients. A probable cause for the problem was that the five-hole probes were not properly aligned perpendicular to the axial flow direction in the yaw plane.

Independent calibrations of the disturbance generating screens were performed at certain intervals during this experimental investigation. These screen calibrations involve making circumferential surveys of the distorted flow produced by the screens in the absence of the rotor. Since there is no rotor present to put any turning into the flow, the circumferential component of velocity is expected to be zero at both upstream and downstream measuring locations. The periods at which the screen calibrations were carried out were carefully logged, and the tests were made with the probes aligned as they were for the present investigation. Thus, it was proposed that an examination of the screen calibration data

would yield a correction wich could be applied to the yaw angle alignment of the probes. The data revealed that significant components of circumferential velocity occurred at both measurement locations used in the tests made with the cambered rotor and at the upstream measurement location used in the studies with the non-lifting rotor. These values of circumferential velocity determined from tests without the rotor installed were found to be from two to five percent of the axial free-stream velocity, and they were consistent for a number of tests done at values of axial velocity corresponding to those used in this study. Based on the relationship $\tan\alpha_2 = V_\theta/V_X$, the amount of deviation from the normal direction in the yaw angle of the probes could be found. For the tests done with the nine-bladed cambered rotor, the upstream and downstream probes were out of alignment by 1.23 and 2.75 degrees, respectively. For the tests done with the six-bladed uncambered rotor, the downstream probe was aligned properly and the upstream probe deviated from the normal direction by 3.49 degrees. It should be noted that a correction of this type need not be applied to the upstream probe in order to calculate the ideal total pressure rise since the inlet component of circumferential velocity was assumed to be zero.

This method of arriving at a correction factor to be applied to the data proved to be clean and acceptable for two reasons. First, the screen calibrations were made at times coinciding with the tests made in the present investigation, and the experimental apparatus, particularly the alignment of the probes, remained unchanged. Secondly, the rotor was not present to disrupt the flow, making the determination of an angular deflection in the yaw plane quite simple and accurate.

The effect of the yaw angle correction was minimal on the axial velocity, radial velocity, and static pressure; only the circumferential

component of velocity was significantly altered. The total pressure was completed unchanged because the total pressure is determined from the center hole on the five-hole probe, and the readings on the center hole will not change over a range of ±10 degrees in the yaw plane (as determined from the calibration of the five-hole probe [37]).

Figures 18, 19, and 20 present the ideal (with yaw angle corrections) and actual total pressure rise coefficient and the total pressure loss coefficient as a function of incidence angle for the six-bladed uncambered rotor configurations having blade stagger angles of 35, 45, and 55 degrees, respectively. Figure 21 shows the three pressure coefficients as a function of incidence for the nine-bladed cambered rotor having a blade stagger angle of 50 degrees. Typically, the losses are lowest at the low absolute values of incidence. As the incidence increases in both the positive and negative directions the losses also increase. The loss data for the non-lifting rotor with a stagger angle of 45 degrees and for the cambered rotor with a 50 degree stagger angle show similar trends, but a slight dip in the loss curve is evident at higher incidence angles. For the 45 degree stagger configuration, the dip occurs at approximately twelve-degree incidence; for the 50 degree stagger configuration, the dip occurs at a much lower value of approximately two-degree incidence angle. The loss curve for the 55 degree stagger angle appears to begin to dip slightly at an incidence angle of roughly eight degrees, and for the 35 degree stagger configuration, the dip begins to occur slightly at an incidence of 15 degrees.

The dip in the loss data which is most evident in Figures 19 and 21 for the 45 degree and 50 stagger configurations was also observed in the steady performance data measured with the twelve-bladed uncambered rotor presented in Reference [37]. As pointed out in Reference [37], the dip

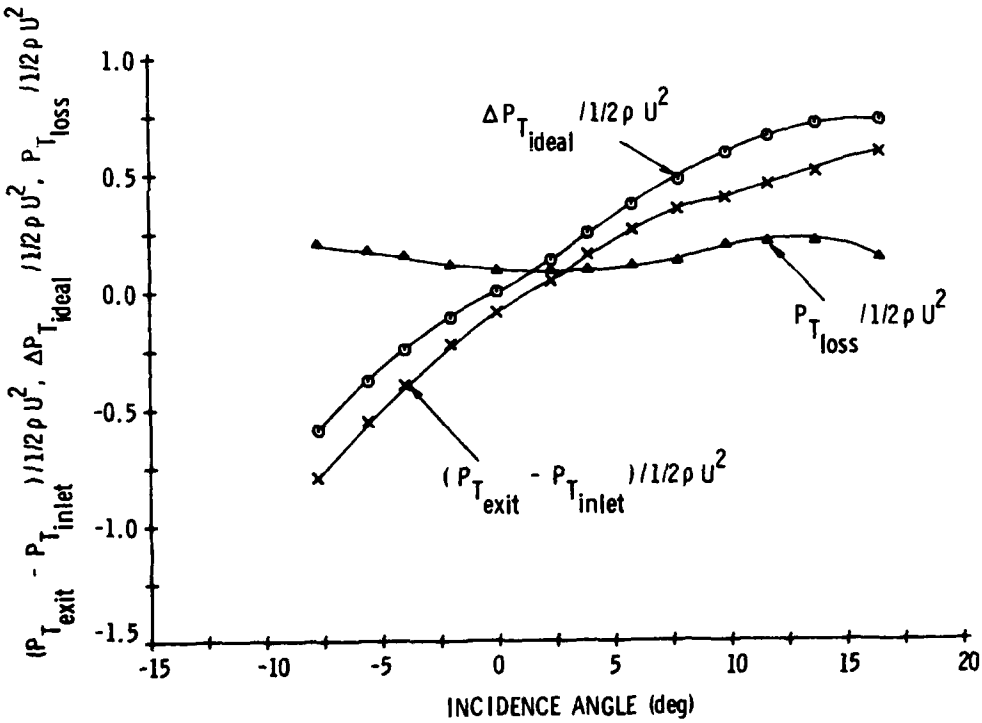

Figure 18. The Ideal and Actual Total Pressure Rise Coefficient and the Total Pressure Loss Coefficient as a Function of Incidence Angle for the Uncambered Rotor with a Blade Stagger Angle of 35 Degrees

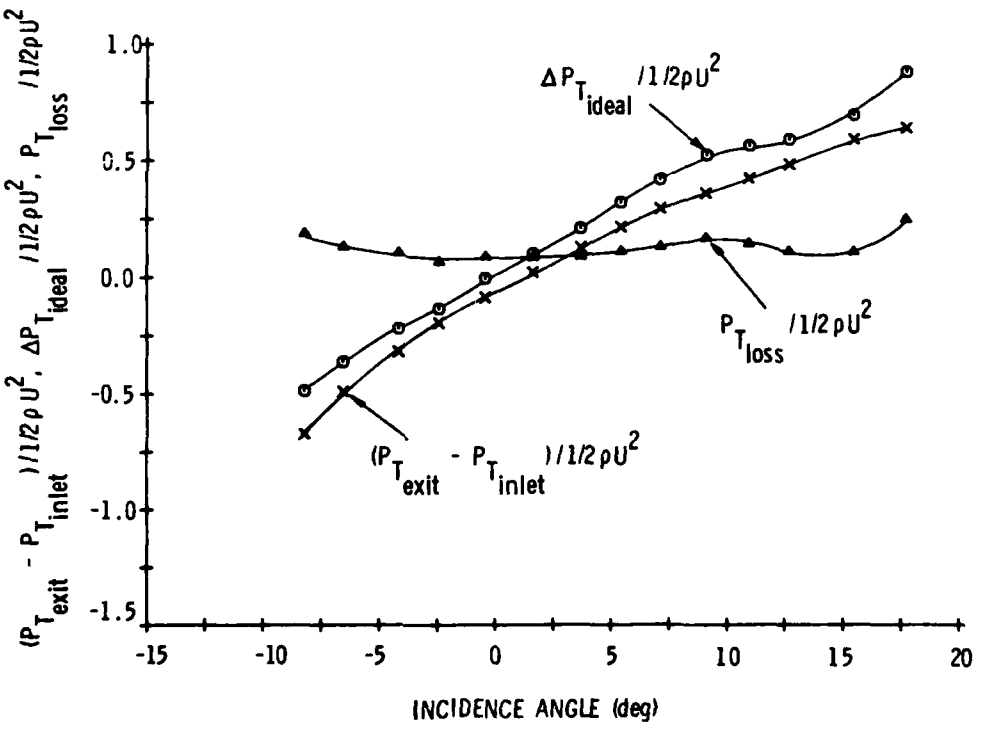

Figure 19. The Ideal and Actual Total Pressure Rise Coefficient and the Total Pressure Loss Coefficient as a Function of Incidence Angle for the Uncambered Rotor with a Blade Stagger Angle of 45 Degrees

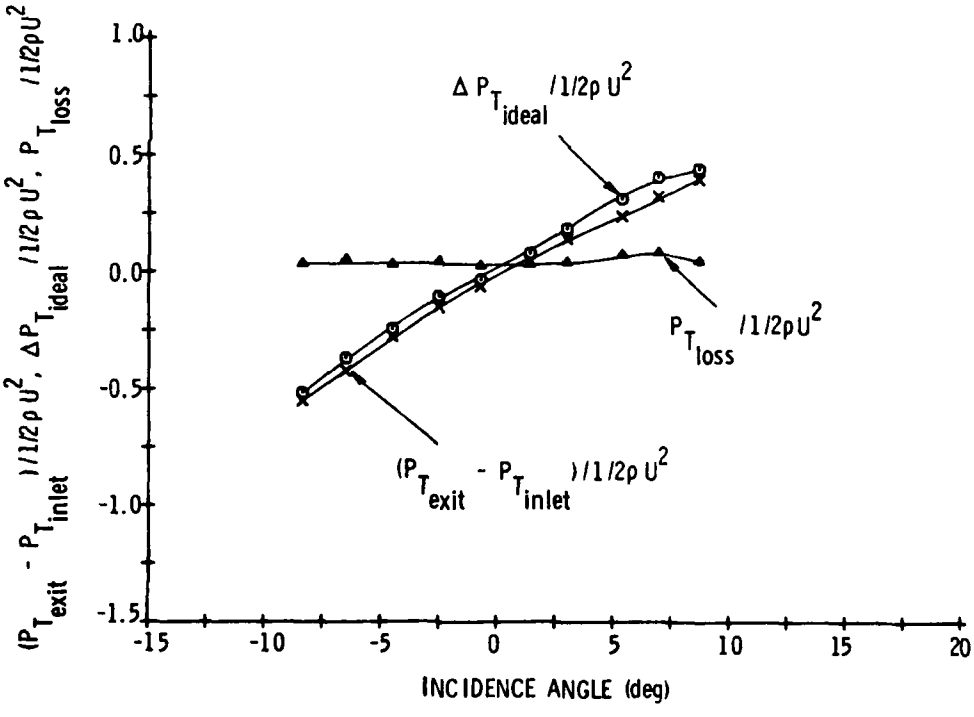

Figure 20. The Ideal and Actual Total Pressure Rise Coefficient and the Total Pressure Loss Coefficient as a Function of Incidence Angle for the Uncambered Rotor with a Blade Stagger Angle of 55 Degrees

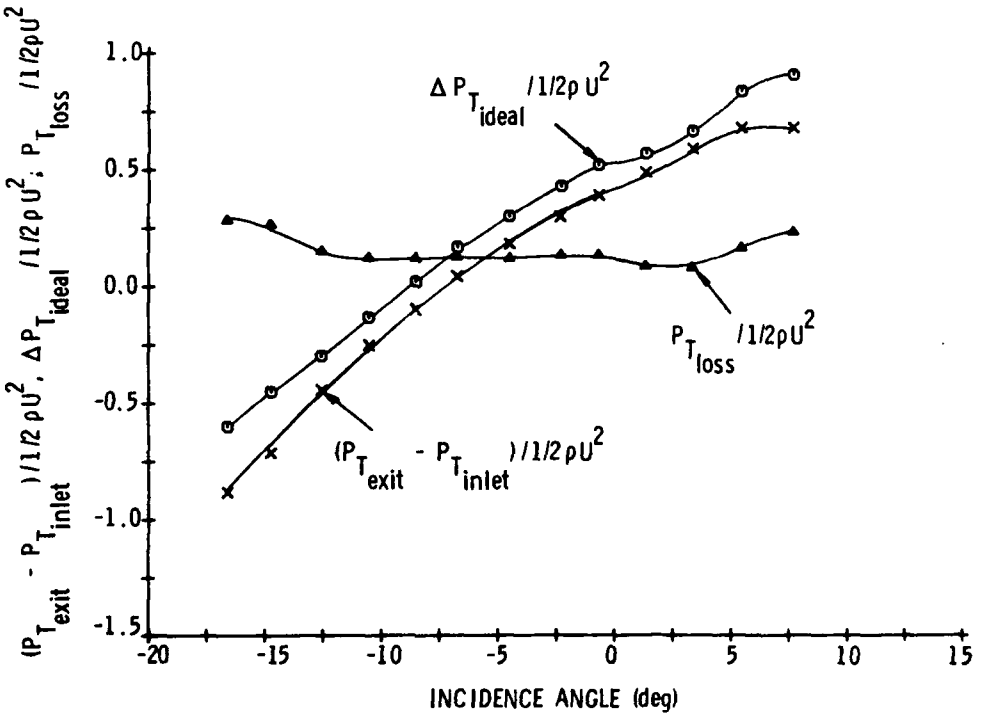

Figure 21. The Ideal and Actual Total Pressure Rise Coefficient and the Total Pressure Loss Coefficient as a Function of Incidence Angle for the Cambered Rotor with a Blade Stagger Angle of 50 Degrees

in the loss data was not important enough to warrant the additional experimentation which would be required to find the cause. However, several possible causes were proposed to explain the existence of the dip in the loss curves. For the nine-bladed rotor with camber, the dip in the loss curve can be explained by the fact that the dip occurs at a point which corresponds to the minimum-loss incidence angle for a circular arc blade blade in a two-dimensional cascade [38]. It can also be seen in both Figures 19 and 21 that the decrease in the losses at the higher incidence angles is due primarily to a change in the ideal pressure rise, which is calculated from the measured circumferential velocity components. Referring to Figures 16 and 17, where the measured circumferential velocity components at the exit of the rotor are plotted, a small dip is evident in the data of $V_{\theta\ exit}/U$ versus Φ at the values of Φ corresponding to the incidences where the dip is found in the loss curves. A change in the V_θ component caused by experimental error could be small and still cause the observed dip in the loss data. But since the dip is observed for both the 45 and 50 degree stagger configurations and also appears to begin to occur for the 35 and 55 degree stagger configurations, it is unlikely that this phenomenon can be attributed to experimental error.

As the incidence angle increases, the pressure gradient across the blade row becomes more adverse and the losses in the boundary layer on the blades become larger. This trend will eventually lead to separation of the flow and a very rapid increase in the pressure losses. Therefore, a proposed explanation for the observed behavior in the loss data is that the flow initially undergoes a laminar separation causing an increase in losses, but at higher incidence, the flow either reattaches or the laminar separation is eliminated completely due to the increased turbulence with

the larger relative velocities at higher rotor speeds. Reference [37] suggests that laminar separation is not likely to have occurred since the Reynolds numbers corresponding to the operating conditions at which the dips occur in the loss data are not within the Reynolds number range where laminar separation may take place. The lower Reynolds number limit where laminar separation may occur is between 3×10^5 and 2×10^5, where the Reynolds number is based on the chord length of the blades and the relative flow velocity. In Figure 18, for example, the losses first become large at an incidence angle of approximately 9.5 degrees. The Reynolds number corresponding to this operating condition is 2.9×10^5, which suggests that laminar separation is not likely to have occurred. Then, since laminar separation does not occur, another possible explanation for the deflection in the loss curve is turbulent separation, but verification of turbulent separation would require additional experimentation.

4.2 Distortion Measurements With the Rotor Installed

The major phase of the experiments consisted of measuring the distorted flow field upstream and downstream of the operating rotor. As discussed in Section 3.3, a parametric study was conducted in which the response of the rotor to an inlet distortion was obtained as a function of various design and operating conditions. These distortion measurements could then be compared to the measurements made by Yocum in Reference [37] of the distorted flow field in the absence of the rotor. This is an important comparison since it shows how the rotor alters the inlet and exit flows. Aside from comparing the distortion measurements made with and without the rotor installed, this section also demonstrates the type of data which was obtained and explains some of the more noticeable features of the distortion shapes both upstream and downstream of the

AD-A084 446 PENNSYLVANIA STATE UNIV UNIVERSITY PARK APPLIED RESE--ETC F/G 21/5
THE UNSTEADY RESPONSE OF AN AXIAL FLOW TURBO-MACHINERY ROTOR TO--ETC(U)
OCT 78 L C BARR N00017-73-C-1418
UNCLASSIFIED ARL/PSU/TM-78-253 NL

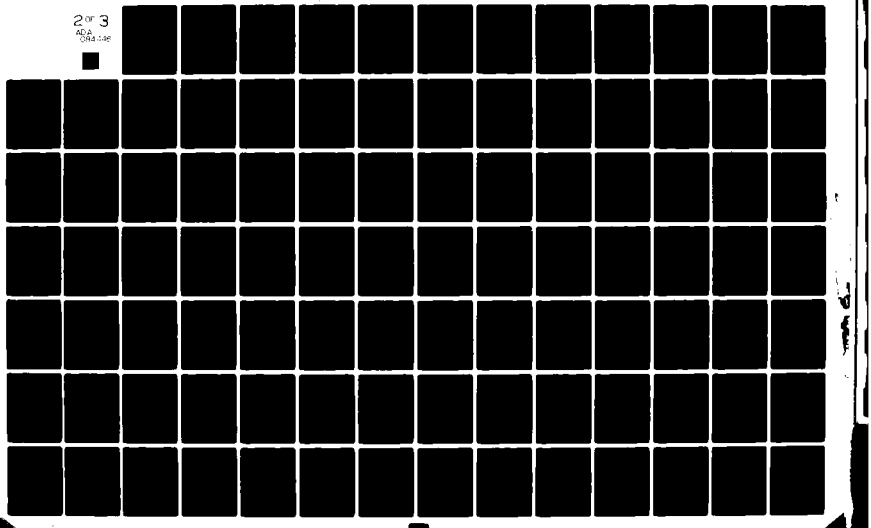

rotor. Due to the excessively large amount of data obtained in this study, it was not practical to document all of the data here. A complete collection of all the data can be found in Reference [39], which includes all the circumferential survey measurements for both the six-bladed uncambered and nine-bladed cambered rotors. In Appendix B, tables of the run conditions for all the tests conducted in this investigation are presented.

The results of the distortion measurements made without the rotor installed for a four-cycle sinusoidal distortion are presented in Reference [37]. Circumferential flow surveys were conducted at the same axial locations as the experiments when the rotor was installed (i.e., stations 1-D and 15), thus providing a direct reference with which to determine the changes caused by the rotor. As mentioned previously, the determination of the flow field characteristics without the rotor is very important since the rotor will affect the flow field. A true measure of the velocity distortion attenuation requires a knowledge of the flow in the absence of the rotor.

The results of the measurements made in the absence of the rotor are presented in Reference [37] as graphs of the dimensionless axial, circumferential, and radial velocities as well as the dimensionless total and static pressures as a function of the circumferential location. It is seen from these results that no changes occur in the flow between the two measurement locations and there are also no static pressure variations. For these reasons, it can be concluded that any flow redistribution caused by the screen occurs upstream of the measurement locations, and the viscous effects due to the shearing nature of the flow are not important over the short distance between the measurement locations [37].

Therefore, any change observed when the rotor is installed will be due to the rotor alone.

4.2.1 Results for the Six-Bladed Zero Steady Lift Rotor. Typical results from the measurements made of the distorted flow field with the six-bladed uncambered rotor operating in a four-cycle distortion appear in Figures 22 through 27, where the axial, circumferential, and radial velocities, total and static pressures, and incidence angle are plotted, respectively. The data for the two axial locations are presented on the same figure, location 1-D being 0.137 chord length upstream of the rotor and location 15 being 0.82 chord length downstream of the rotor. These figures reveal the usual characteristics observed in distortion measurements. A comparison of the axial velocity with and without the rotor present shows that the axial velocity distortion was attenuated upstream of the rotor. Downstream of the rotor, the axial velocity distortion is seen to have undergone a further reduction in amplitude. It is seen that the rotor creates a variation in the circumferential component of velocity upstream of the rotor. Downstream of the rotor, the circumferential velocity is nearly uniform. The radial velocity distribution presented in Figure 24 shows that the radial component of velocity is less than ten percent of the axial free-stream velocity for this condition of large incidence angle, 8.5 degrees. This demonstrates the basis of the assumption made throughout the study that the flow field is two-dimensional. At lower values of incidence angle, the radial velocities were less. It is observed in Figure 26 that a static pressure gradient arises at the upstream location. This is due to the presence of the rotor since a gradient in static pressure at the upstream location was not observed without the rotor operating. Downstream of the rotor, as seen in Figure

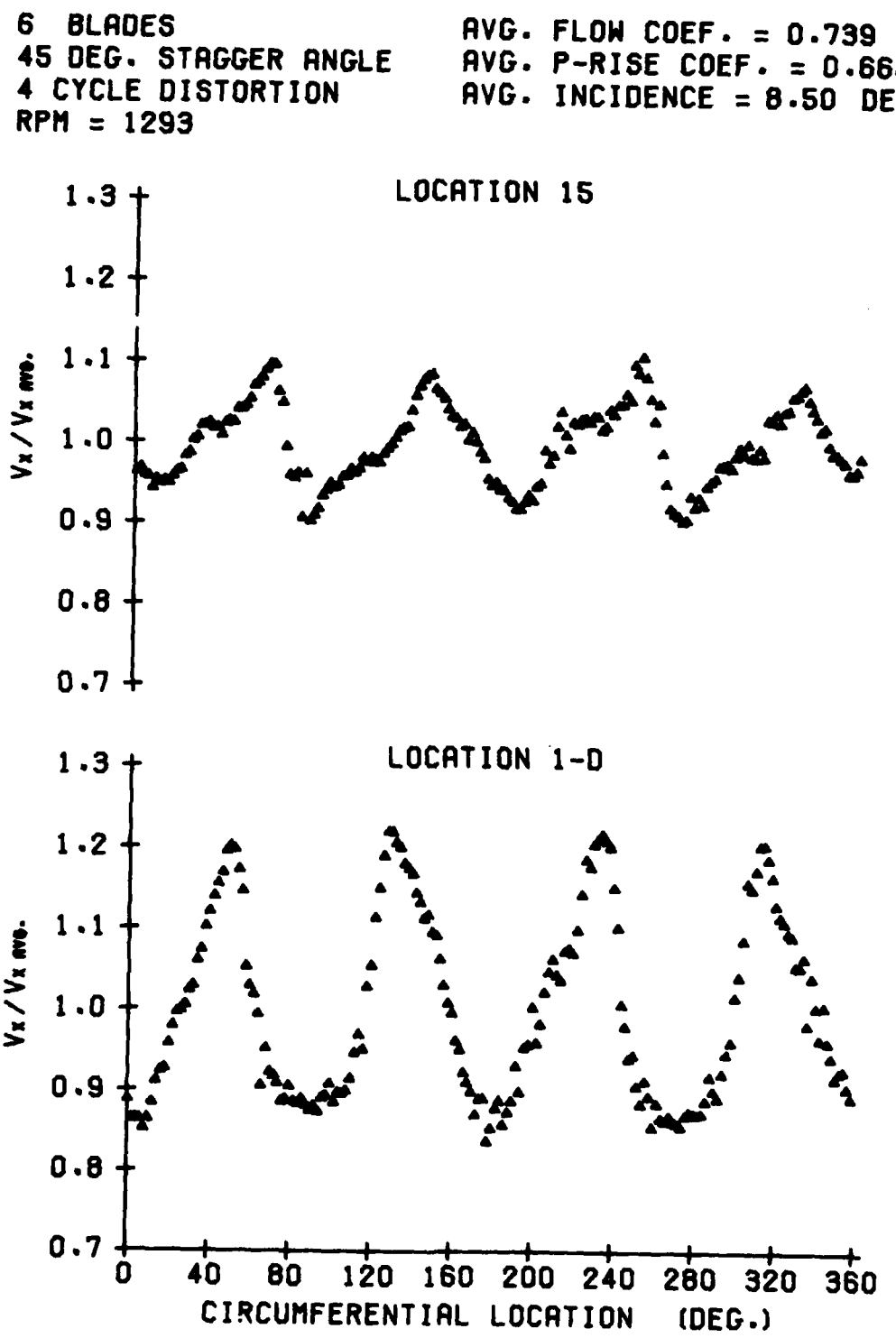

Figure 22. Dimensionless Axial Velocity Variation for the Four-Cycle Distortion with the Six-Bladed Uncambered Rotor

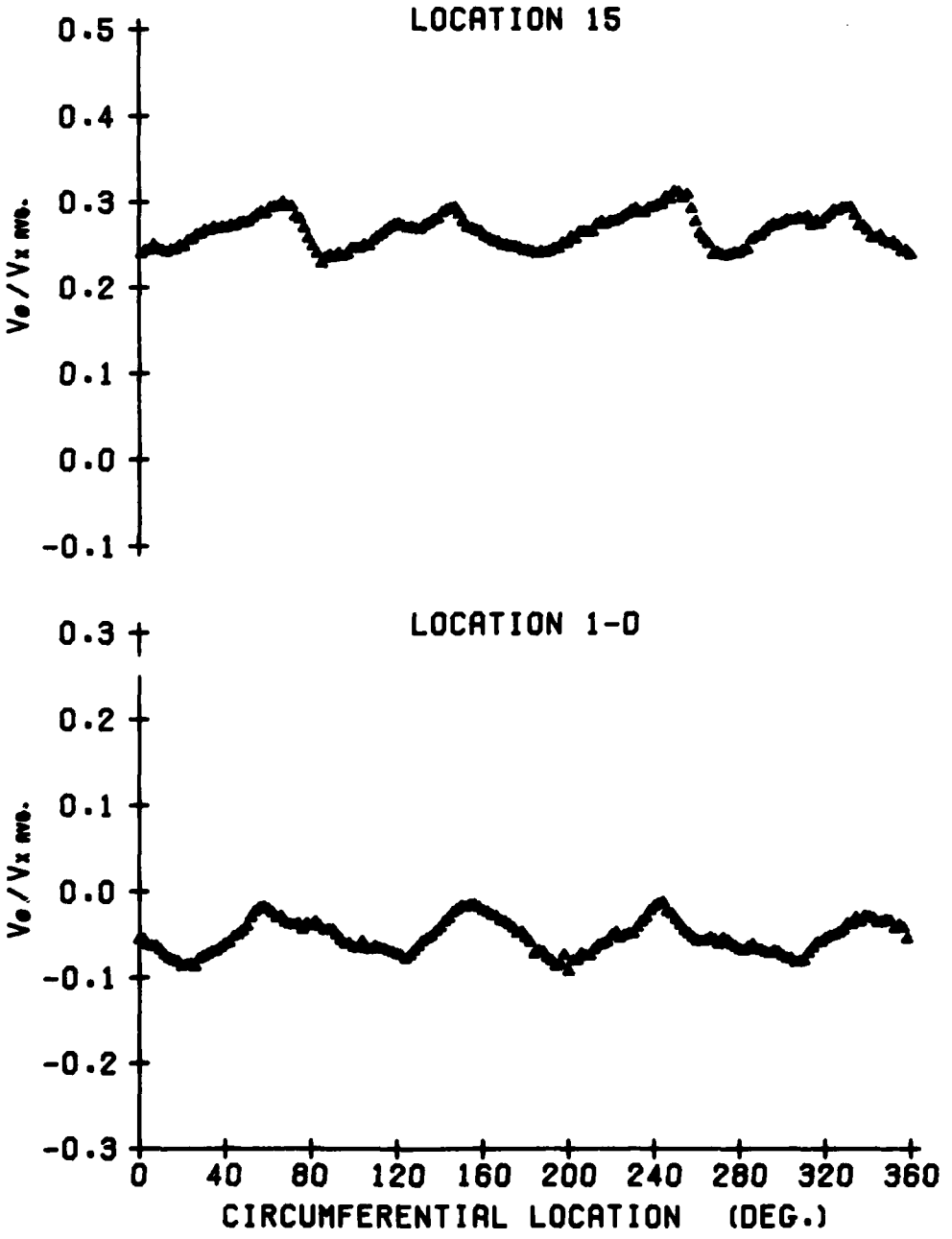

Figure 23. Dimensionless Circumferential Velocity Variation for the Four-Cycle Distortion with the Six-Bladed Uncambered Rotor

6 BLADES
45 DEG. STAGGER ANGLE
4 CYCLE DISTORTION
RPM = 1293

AVG. FLOW COEF. = 0.739
AVG. P-RISE COEF. = 0.660
AVG. INCIDENCE = 8.50 DEG.

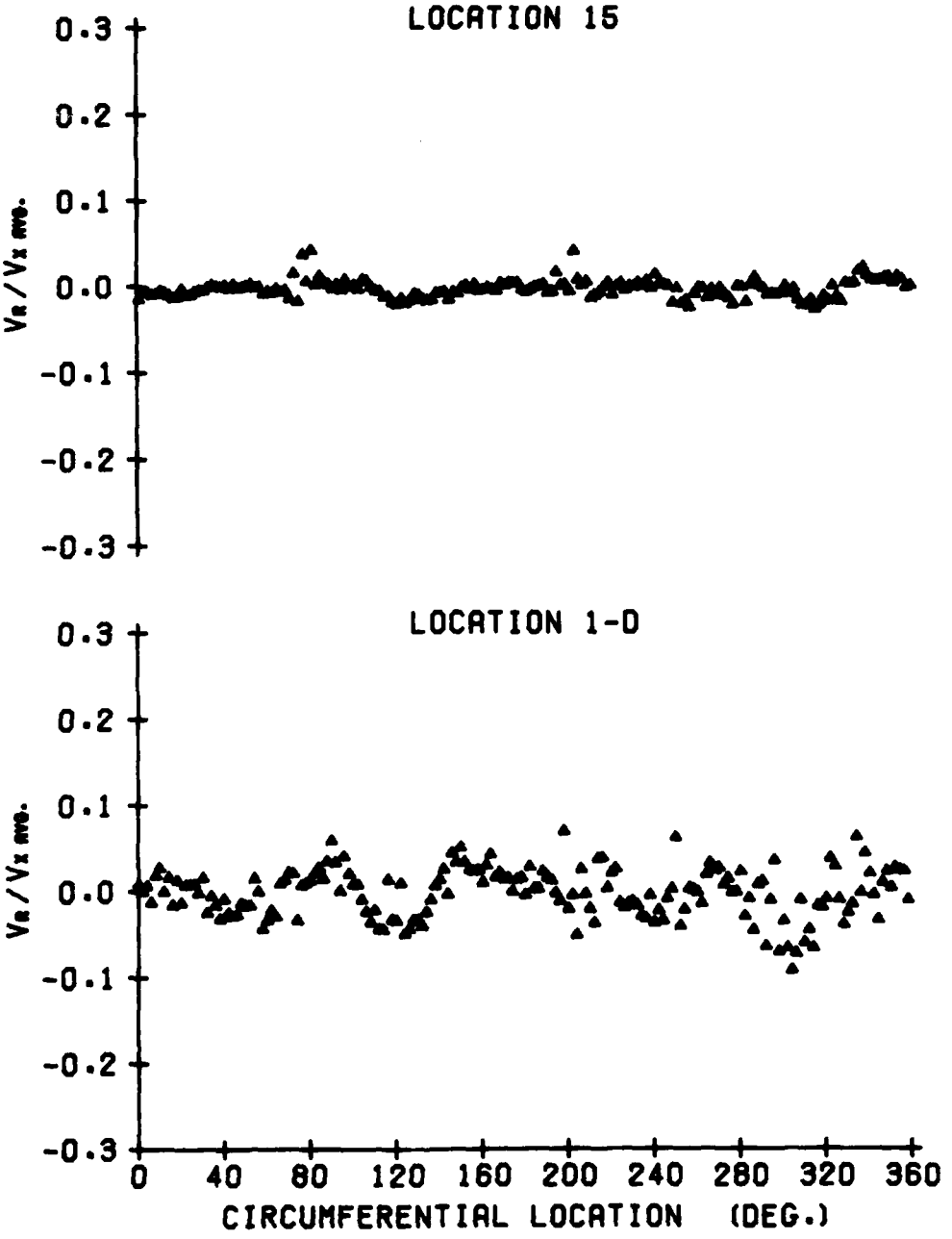

Figure 24. Dimensionless Radial Velocity Variation for the Four-Cycle Distortion with the Six-Bladed Uncambered Rotor

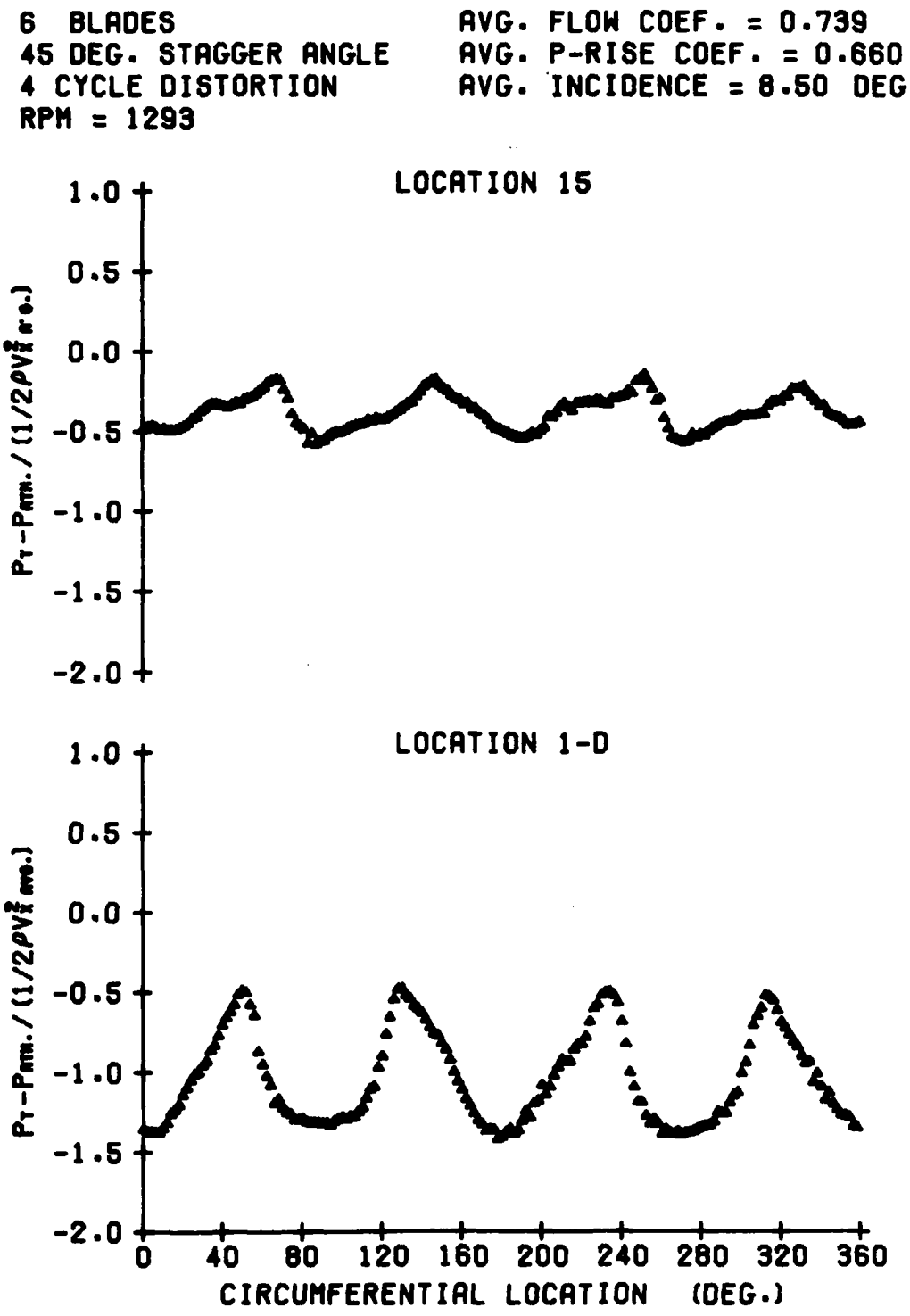

Figure 25. Dimensionless Total Pressure Variation for the Four-Cycle Distortion with the Six-Bladed Uncambered Rotor

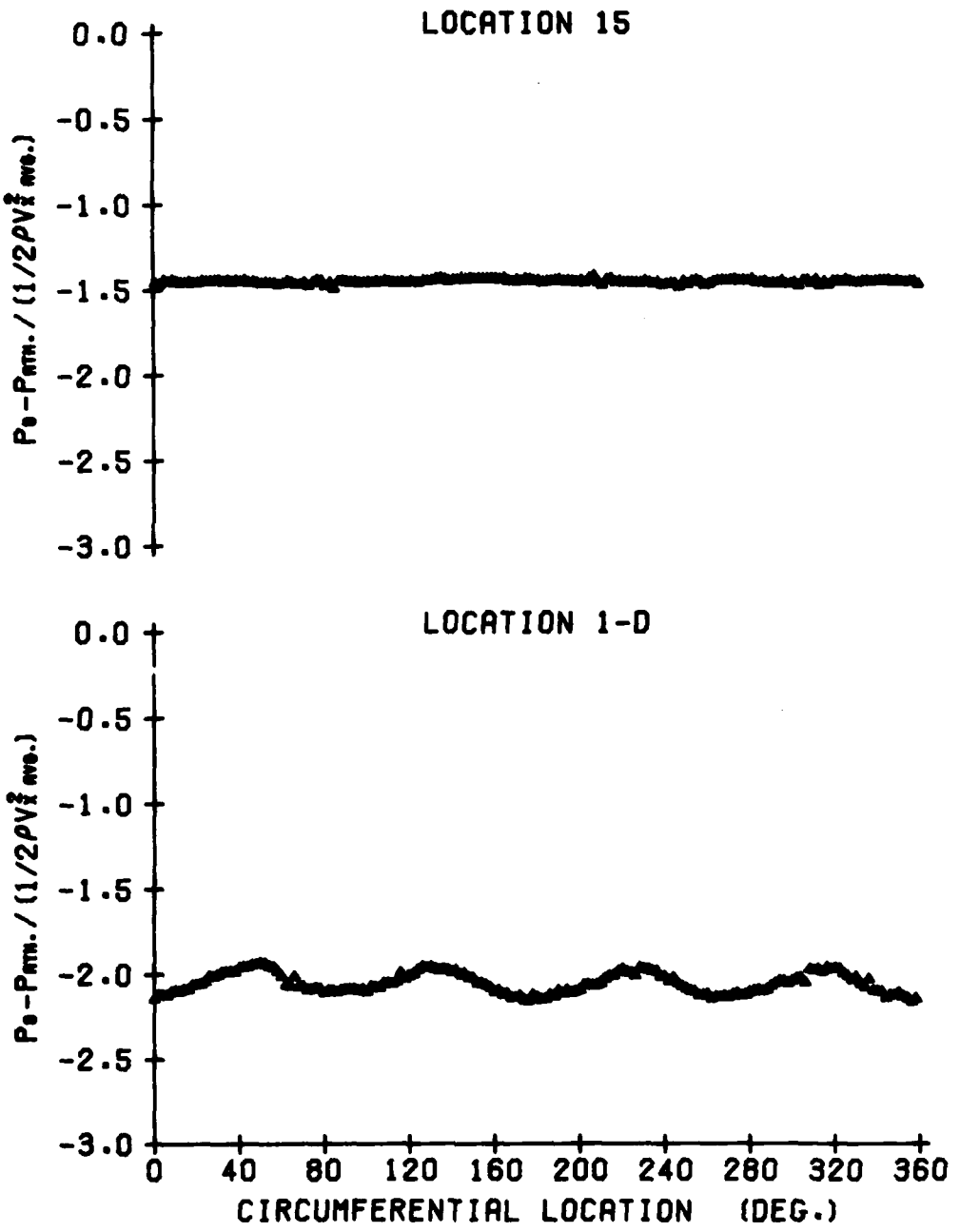

Figure 26. Dimensionless Static Pressure Variation for the Four-Cycle Distortion with the Six-Bladed Uncambered Rotor

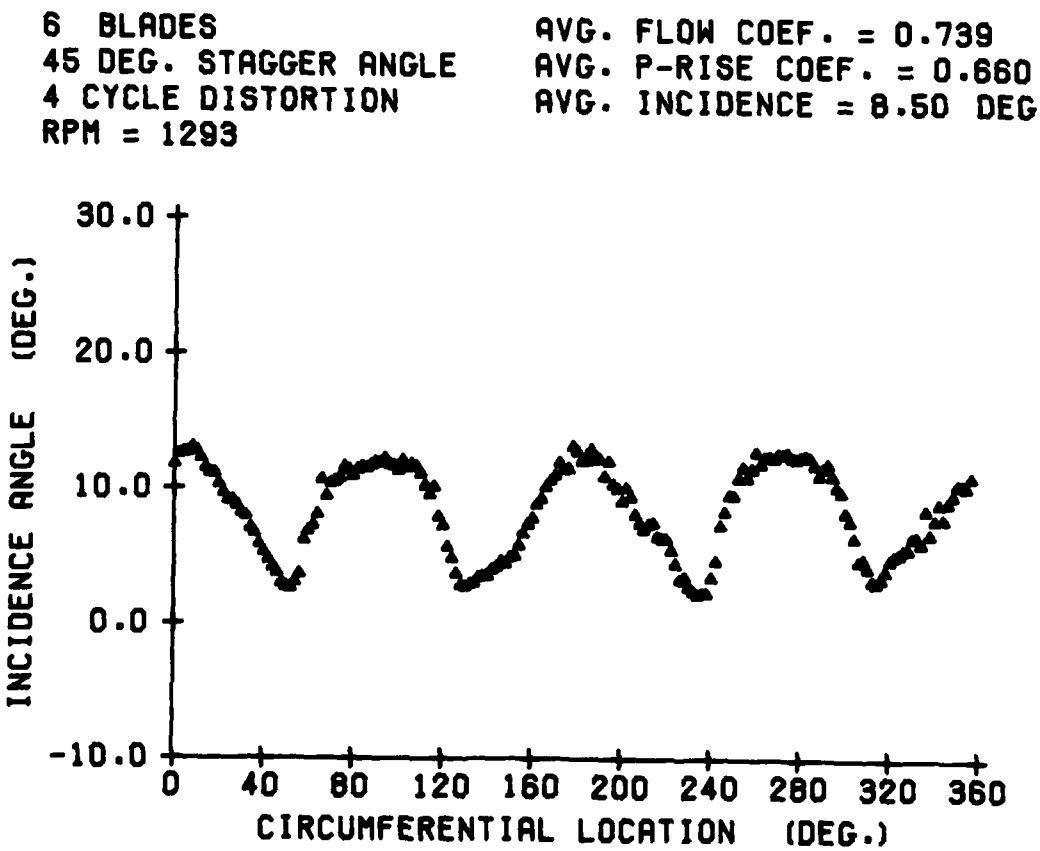

Figure 27. Circumferential Variation of the Flow Incidence on the Blades for the Four-Cycle Distortion with the Six-Bladed Uncambered Rotor

26, the static pressure is constant. A comparison of the total pressure distortion data with and without the rotor operating reveals that the total pressure distortion upstream of the rotor is basically unchanged since no work has been done on the flow. However, as the flow passes through the rotor, the amplitude of the total pressure distortion is significantly reduced. Finally, Figure 27 shows the incidence angle on the blades as a function of circumferential location. From a quasi-steady viewpoint, the local incidence determines the fluctuating forces on the blades.

Presented in Figures 28 through 33 are the distortion data obtained in the AFRF for a 90 degree square distortion with the six-bladed rotor operating. Once again, the dimensionless velocity and pressure components as well as the local blade incidence angle are plotted as functions of circumferential location. In Reference [37], the results are included of the distortion measurements made with the 90 degree square distortion without the rotor installed. It is found from a comparison of these data with Figures 28, 29, and 32 that the changes in the axial velocity, circumferential velocity, and static pressure caused by the rotor are the same as those just discussed for a four-cycle sinusoidal distortion. However, the total pressure distortion behaves differently since it is found from a comparison of Figure 31 and the data in Reference [37] that the magnitude of the distortion upstream of the rotor has increased. Although the change was small, no change was expected because, from a two-dimensional viewpoint, the total pressure at the mean radius can only be changed by doing work on the fluid or if a change in the mixing losses occurs. The rotor obviously cannot do work on the fluid (or remove energy) upstream from itself. It is possible that the mixing losses could increase due to the

6 BLADES
45 DEG. STAGGER ANGLE
90 DEG. SQ. DISTORTION
RPM = 1375

AVG. FLOW COEF. = 0.722
AVG. P-RISE COEF. = 0.800
AVG. INCIDENCE = 9.18 DEG.

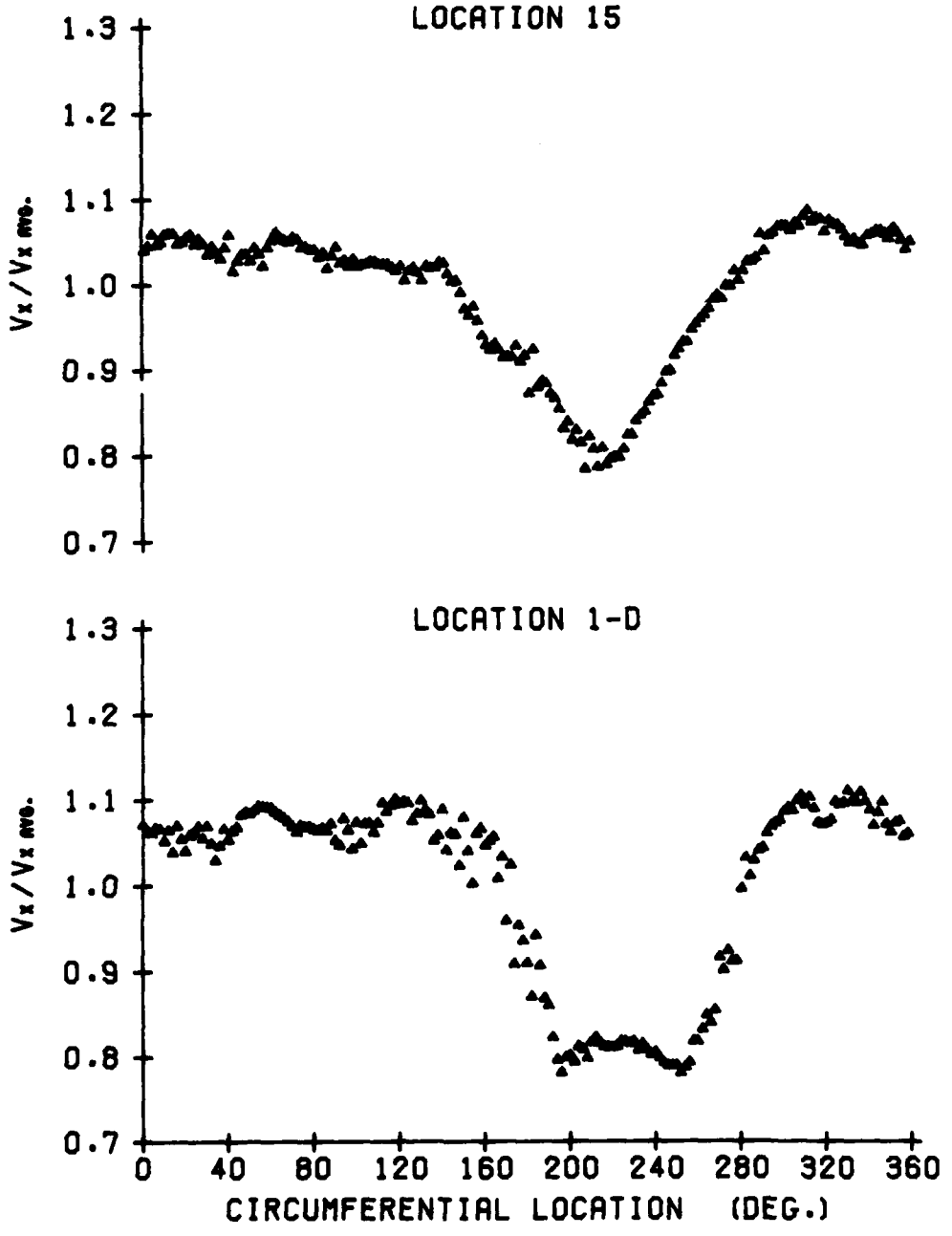

Figure 28. Dimensionless Axial Velocity Variation for the 90 Degree Square Distortion with the Six-Bladed Uncambered Rotor

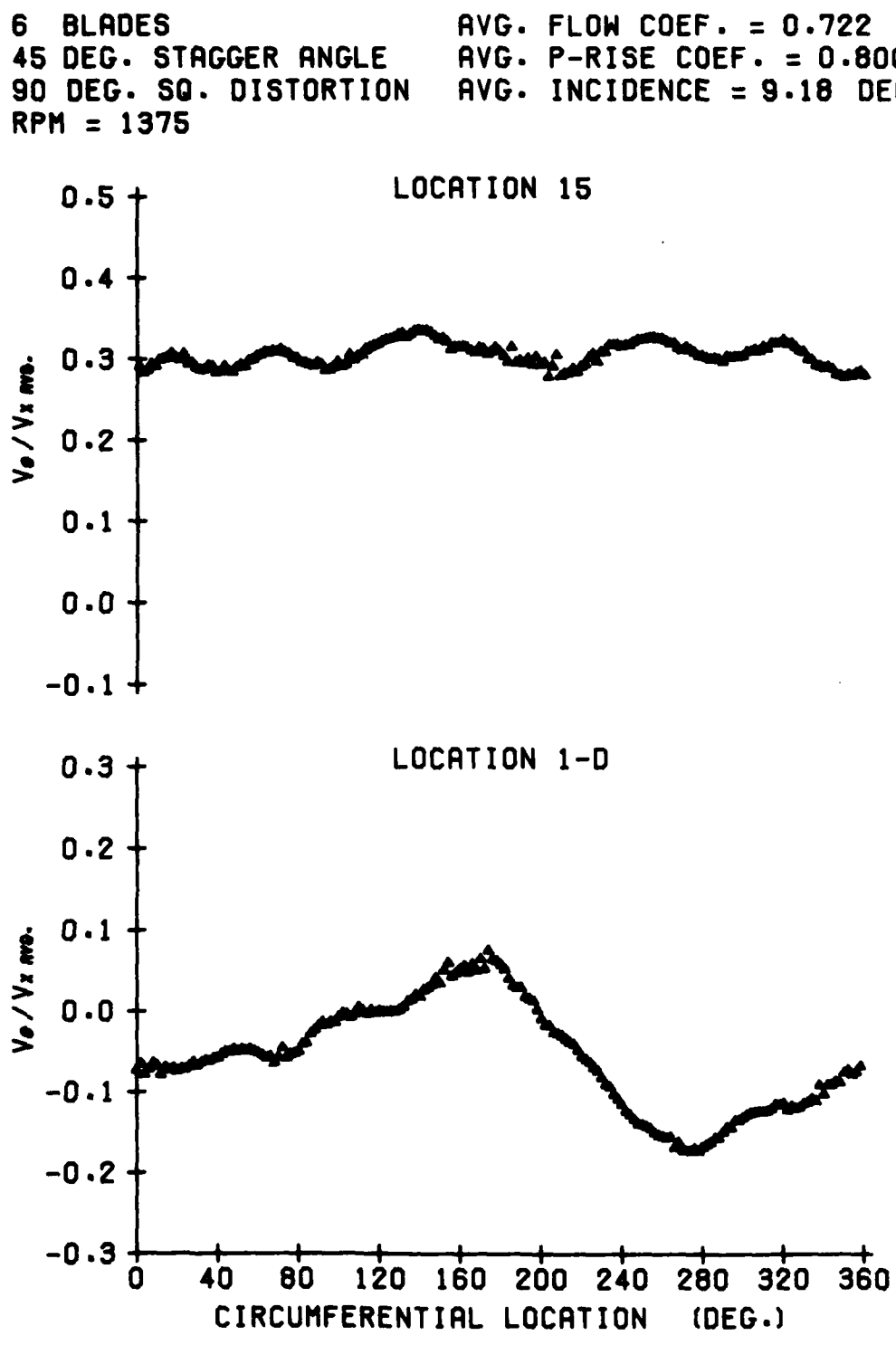

Figure 29. Dimensionless Circumferential Velocity Variation for the 90 Degree Square Distortion with the Six-Bladed Uncambered Rotor

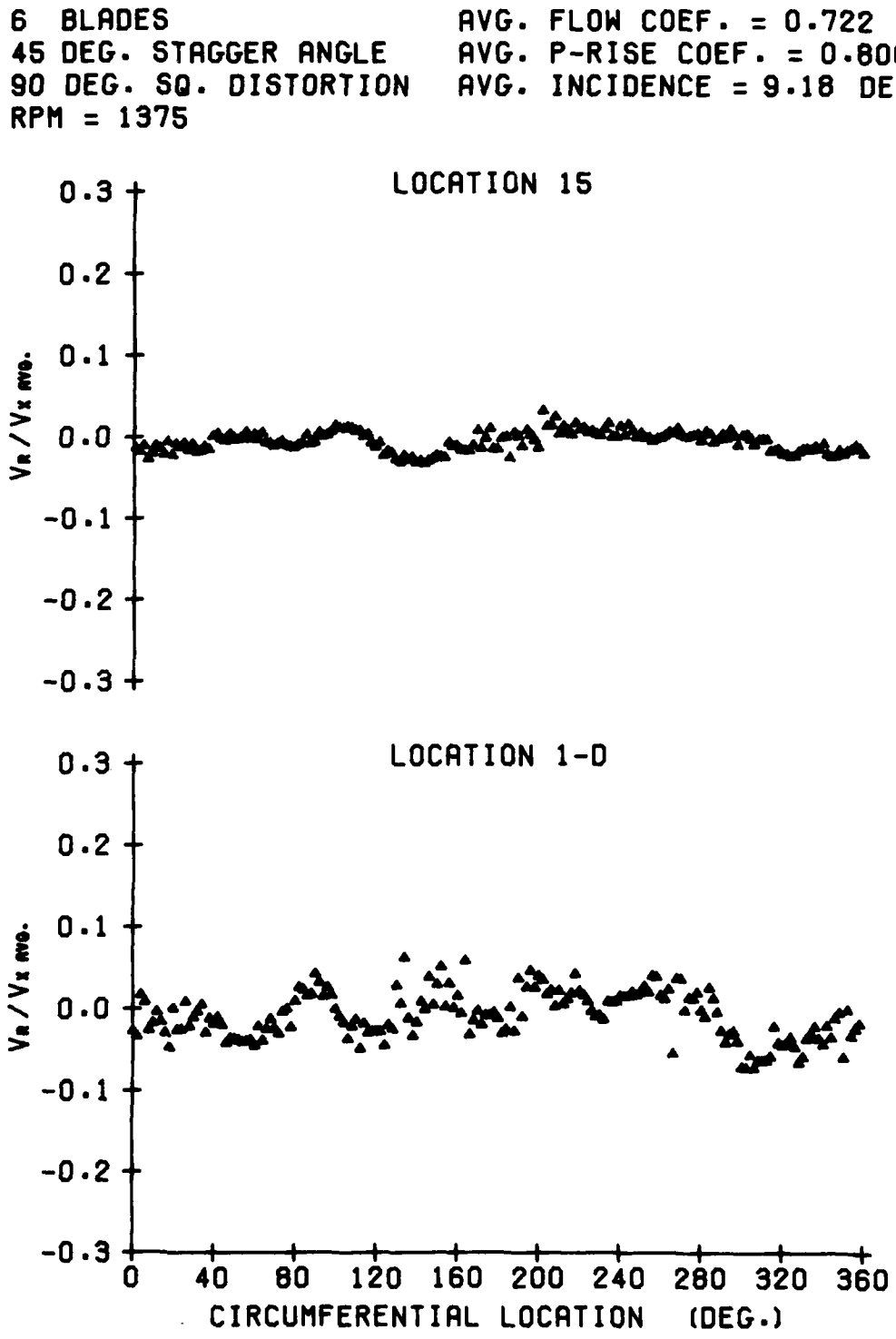

Figure 30. Dimensionless Radial Velocity Variation for the 90 Degree Square Distortion with the Six-Bladed Uncambered Rotor

6 BLADES
45 DEG. STAGGER ANGLE
90 DEG. SQ. DISTORTION
RPM = 1375

AVG. FLOW COEF. = 0.722
AVG. P-RISE COEF. = 0.800
AVG. INCIDENCE = 9.18 DEG.

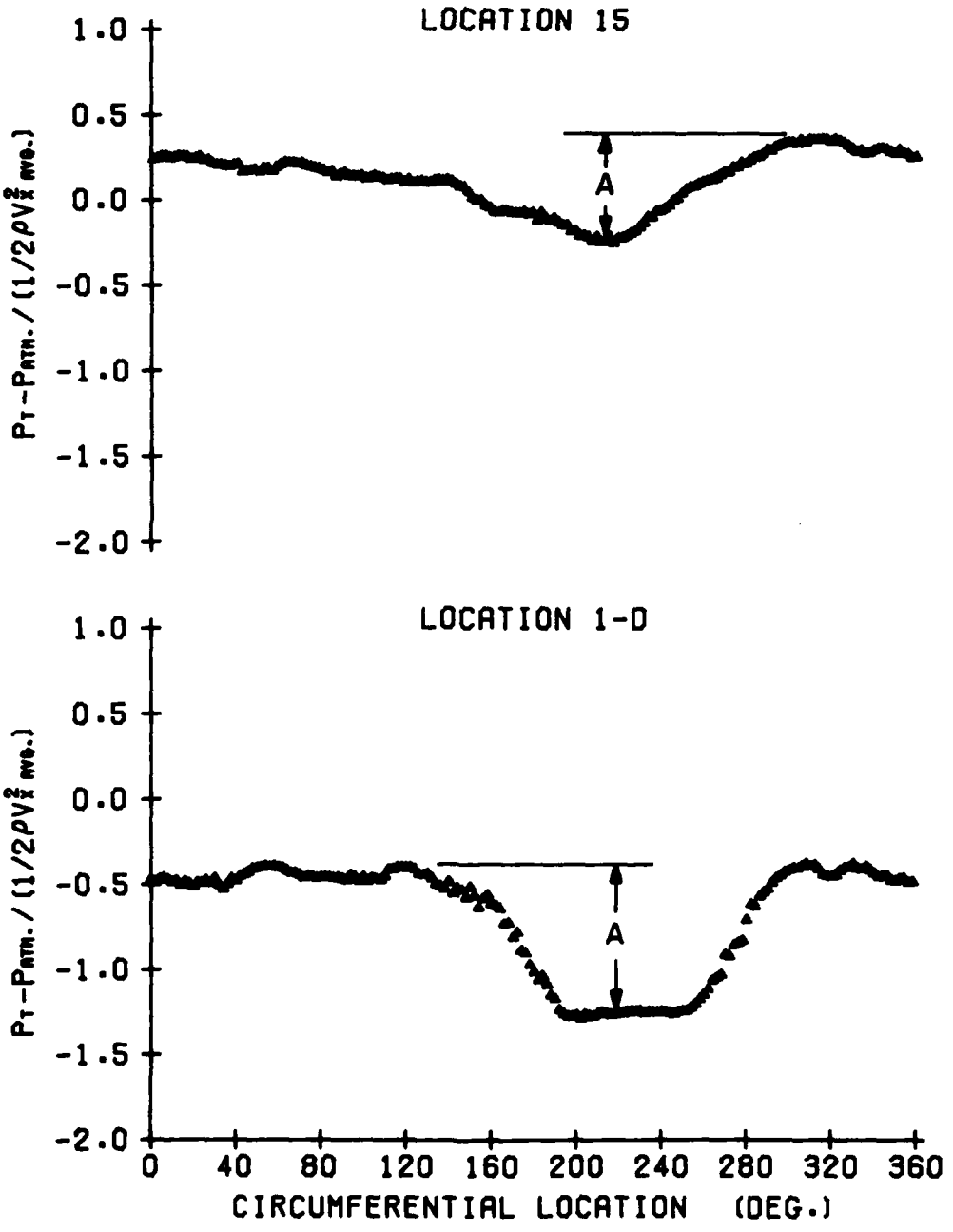

Figure 31. Dimensionless Total Pressure Variation for the 90 Degree Square Distortion with the Six-Bladed Uncambered Rotor

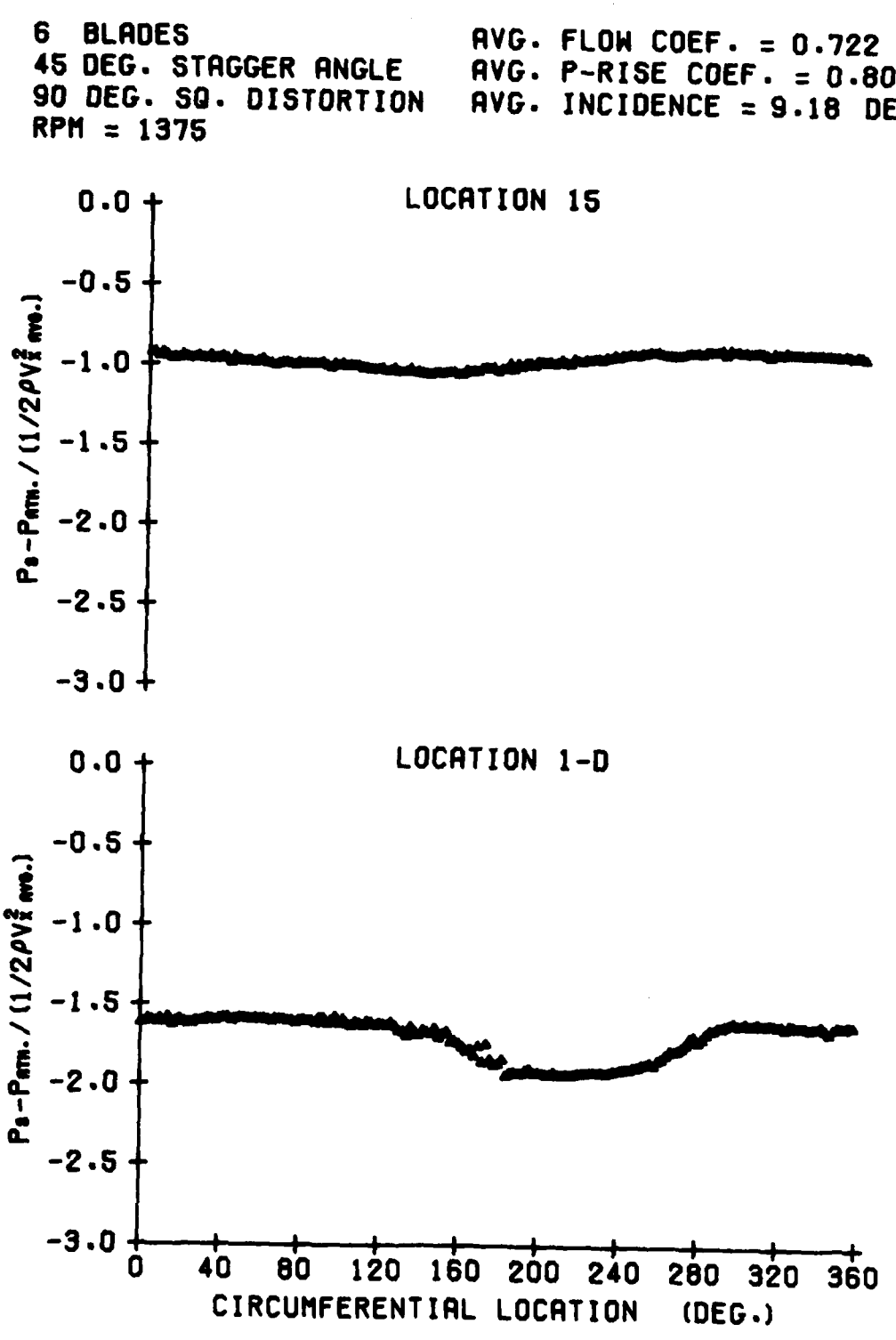

Figure 32. Dimensionless Static Pressure Variation for the 90 Degree Square Distortion with the Six-Bladed Uncambered Rotor

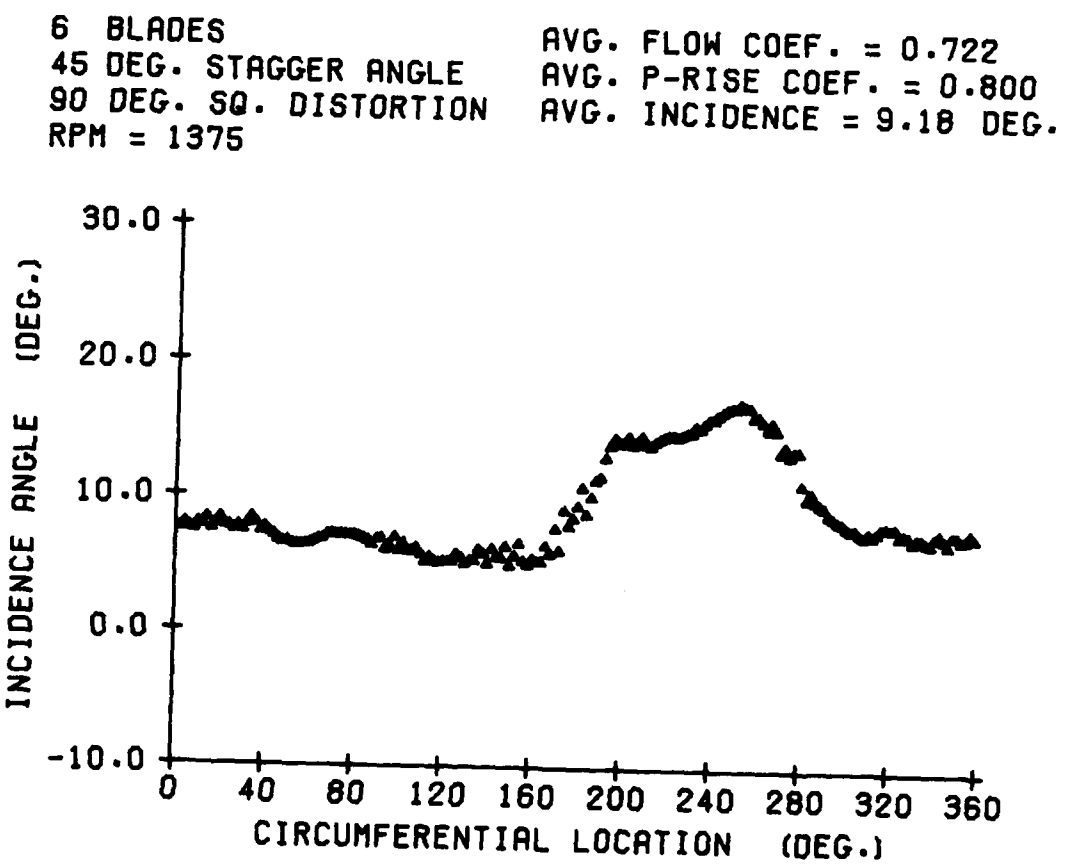

Figure 33. Circumferential Variation of the Flow Incidence on the Blades for the 90 Degree Square Distortion with the Six-Bladed Uncambered Rotor

flow redistribution which takes place. However, the symmetry of the distortion and the magnitude of the change makes this unlikely. Therefore, as pointed out in Reference [37], the most likely cause of the observed change in the total pressure distortion amplitude is a radial total pressure gradient produced by the screens, followed by a radial shift in the streamlines due to the flow redistribution which takes place near the rotor. This radial shift would apparently invalidate the two-dimensional flow assumption made throughout this study, but the change in the total pressure distortion is sufficiently small so that the radial shift may be neglected.

4.2.2 Results for the Nine-Bladed Cambered Rotor. A series of distortion measurements was also made using a nine-bladed cambered rotor with a fixed stagger angle of 50 degrees at the mean radius. In order to determine the effect of the rotor on the inlet distortion at different radial or spanwise locations along the blade, tests were conducted with the probes located at the following radial positions: 9.333 inches (23.708 cm), 8.417 inches (21.381 cm), 6.583 inches (11.829 cm), and 5.667 inches (14.396 cm). The mean radius of the blade is 7.75 inches (19.685 cm), so the tests were made at two radii greater than the mean radius and two radii less than the mean radius. As before, the probes were axially located at stations 1-D and 15.

Figures 34, 35, 36, and 37 show the axial velocity, circumferential velocity, total pressure, and static pressure variations, respectively, for the measurements made for a four-cycle distortion with the probes located at the radial position closest to the outer casing wall. In order to examine the effects of different radial locations, Figures 38 through 41 show the velocity and pressure distributions for approximately

9 BLADES
50 DEG. STAGGER ANGLE
4 CYCLE DISTORTION
RPM = 1663

AVG. FLOW COEF. = 0.534
AVG. P-RISE COEF. = 2.313
AVG. INCIDENCE = 5.77 DEG.

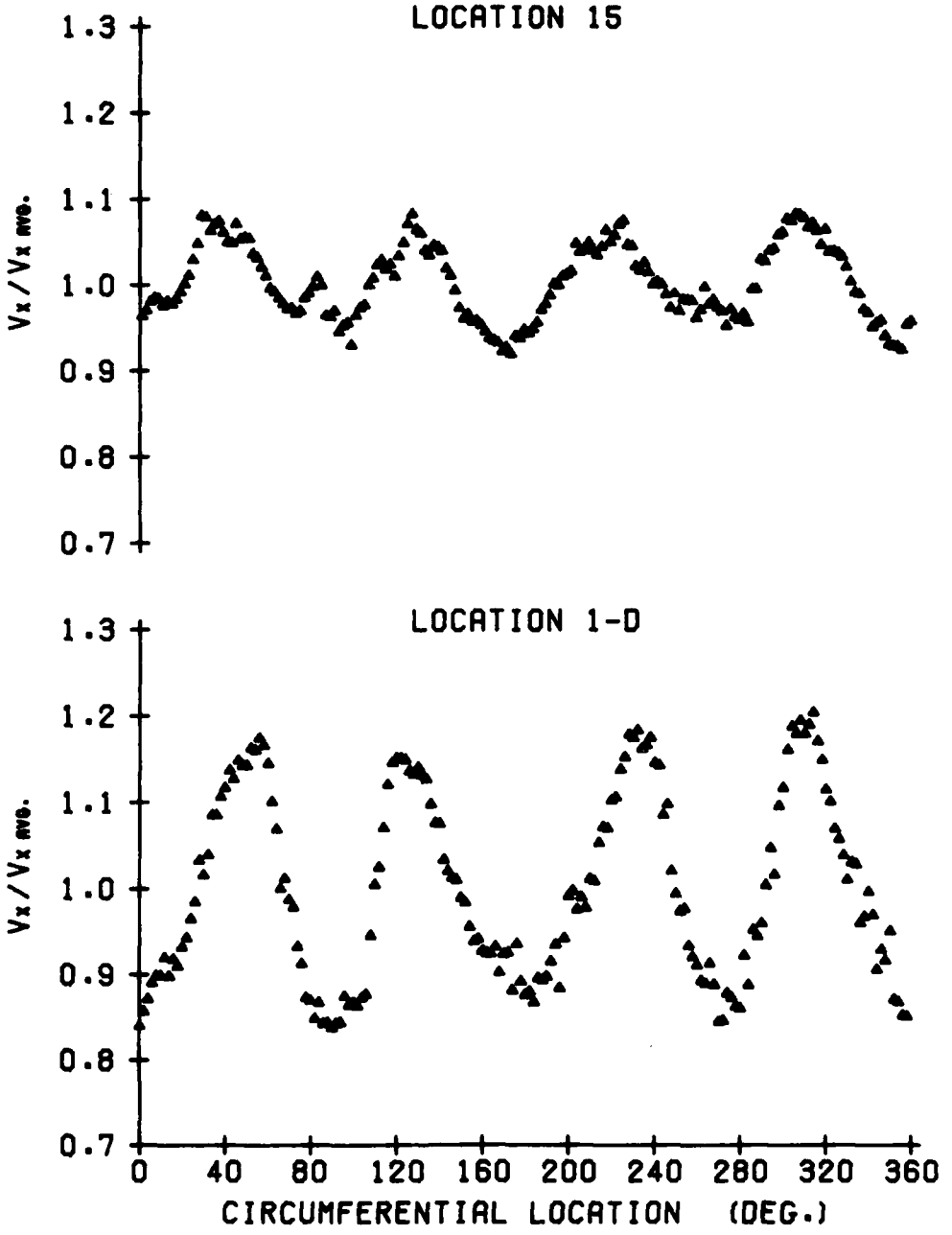

Figure 34. Axial Velocity Distribution for the Four-Cycle Distortion with the Nine-Bladed Cambered Rotor, Measured at a Radial Distance of 11.642 cm from the Hub Surface

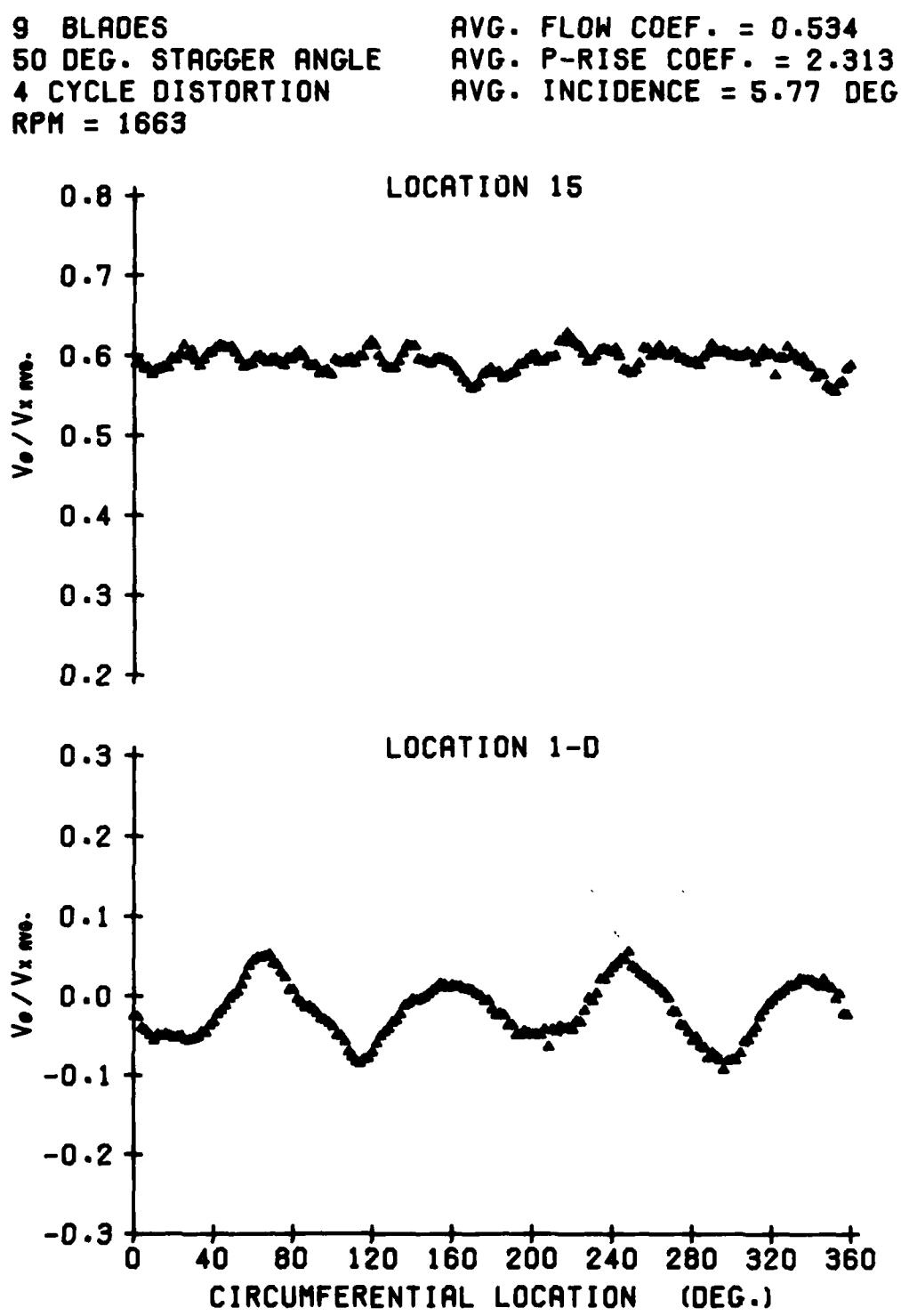

Figure 35. Circumferential Velocity Distribution for the Four-Cycle Distortion with the Nine-Bladed Cambered Rotor, Measured at a Radial Distance of 11.642 cm from the Hub Surface

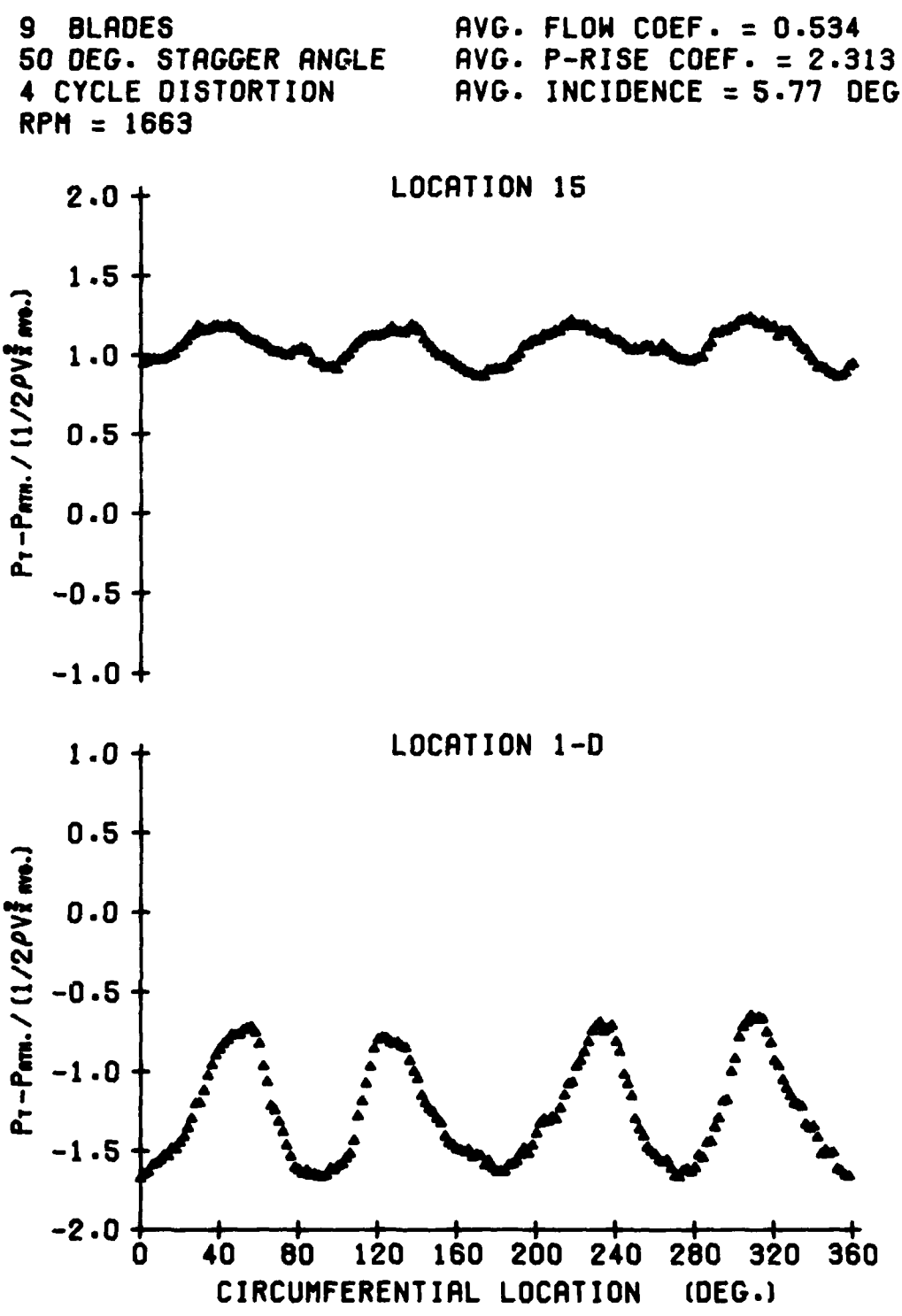

Figure 36. Total Pressure Distribution for the Four-Cycle Distortion with the Nine-Bladed Cambered Rotor, Measured at a Radial Distance of 11.642 cm from the Hub Surface

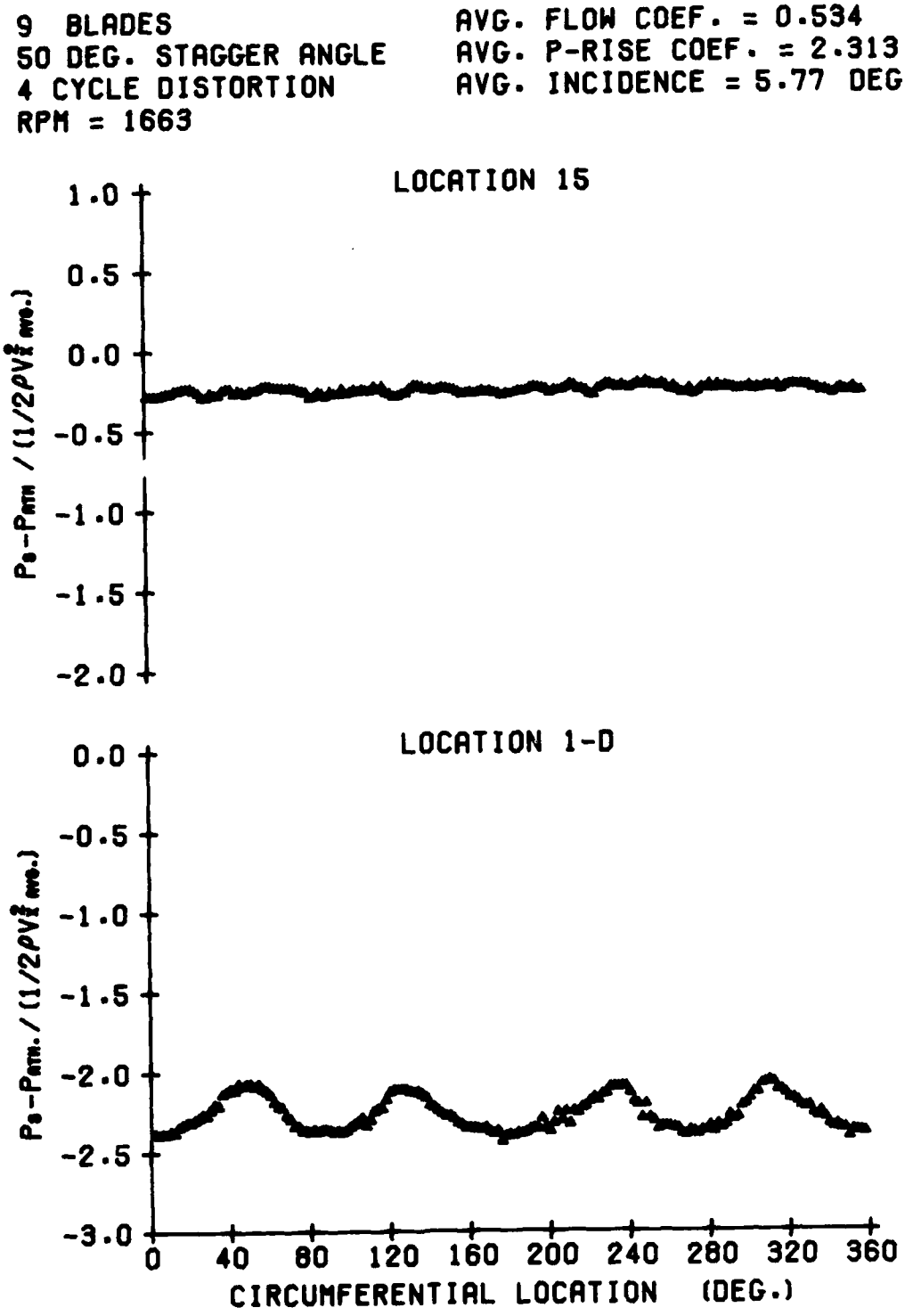

Figure 37. Static Pressure Distribution for the Four-Cycle Distortion with the Nine-Bladed Cambered Rotor, Measured at a Radial Distance of 11.642 cm from the Hub Surface

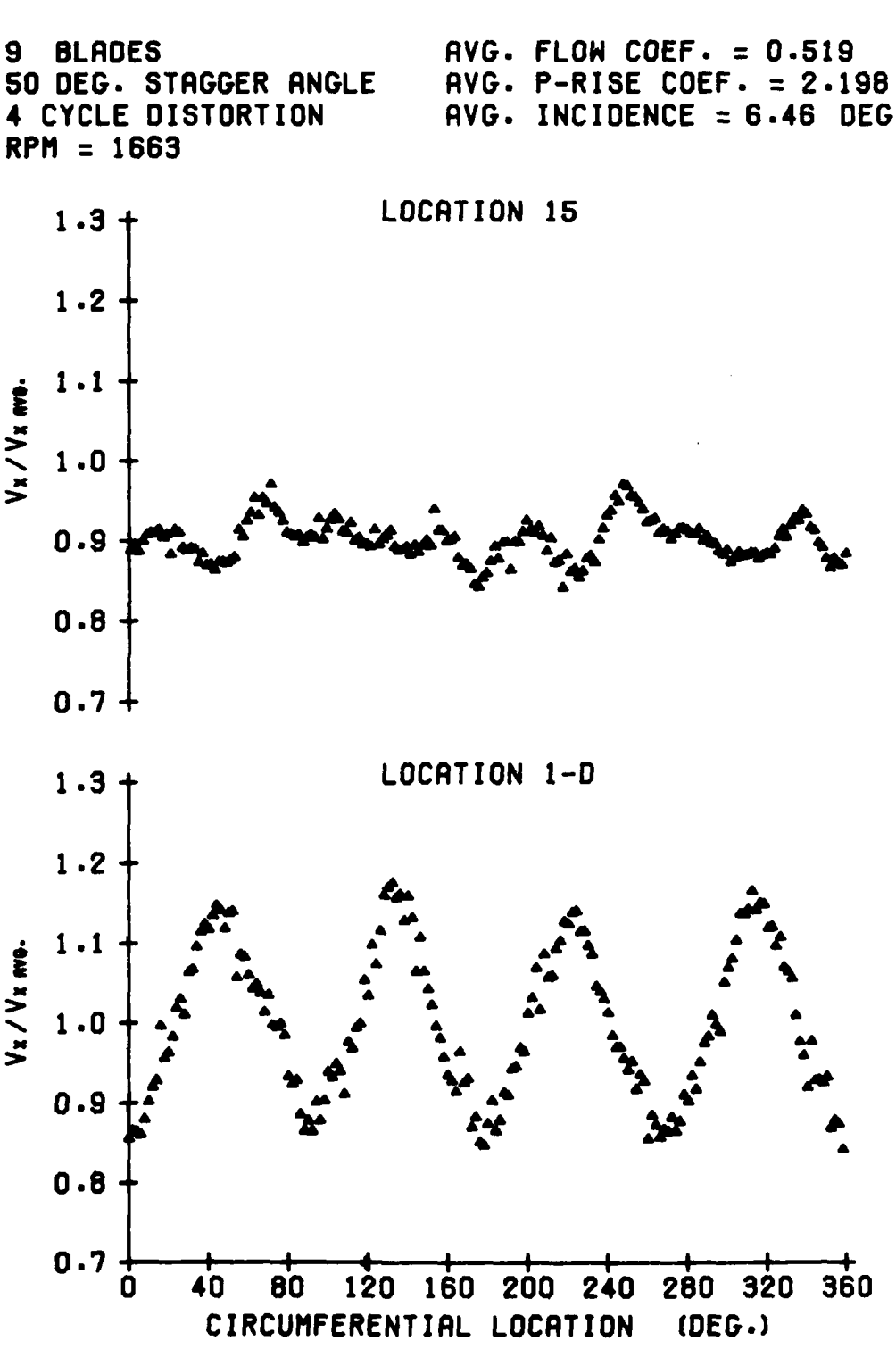

Figure 38. Axial Velocity Distribution for the Four-Cycle Distortion with the Nine-Bladed Cambered Rotor, Measured at a Radial Distance of 2.328 cm from the Hub Surface

9 BLADES
50 DEG. STAGGER ANGLE
4 CYCLE DISTORTION
RPM = 1663

AVG. FLOW COEF. = 0.519
AVG. P-RISE COEF. = 2.198
AVG. INCIDENCE = 6.46 DEG.

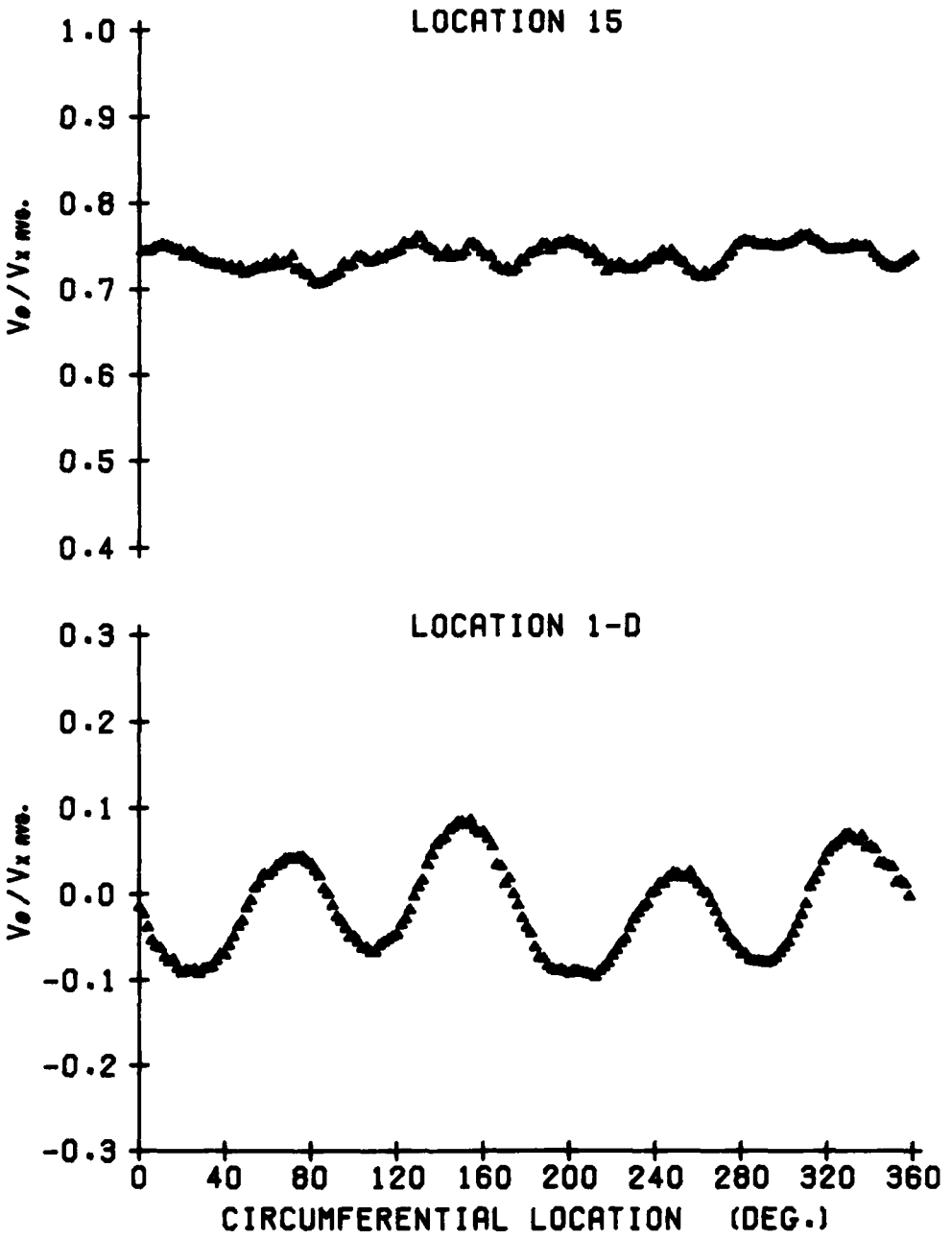

Figure 39. Circumferential Velocity Distribution for the Four-Cycle Distortion with the Nine-Bladed Cambered Rotor, Measured at a Radial Distance of 2.328 cm from the Hub Surface

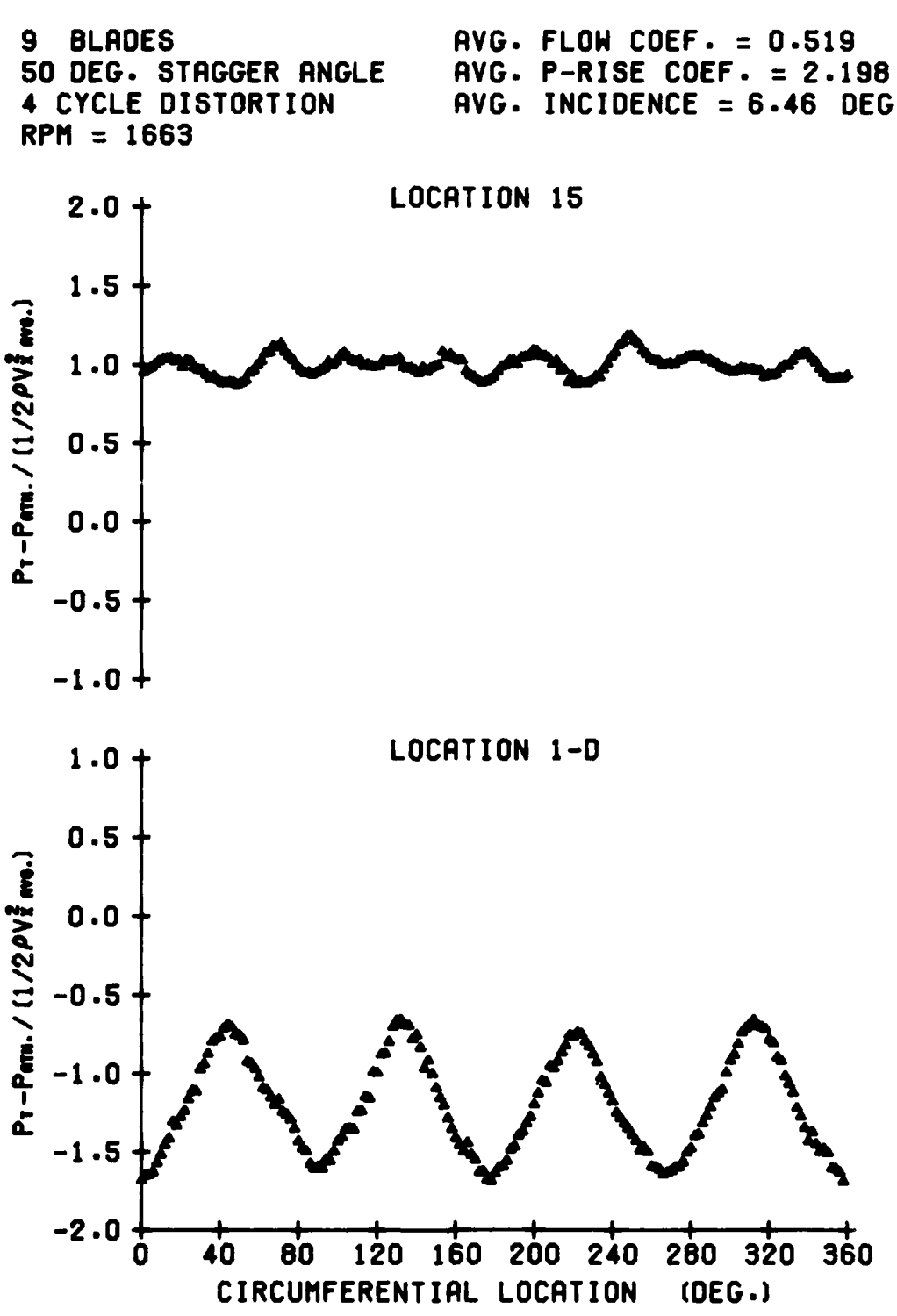

Figure 40. Total Pressure Distribution for the Four-Cycle Distortion with the Nine-Bladed Cambered Rotor, Measured at a Radial Distance of 2.328 cm from the Hub Surface

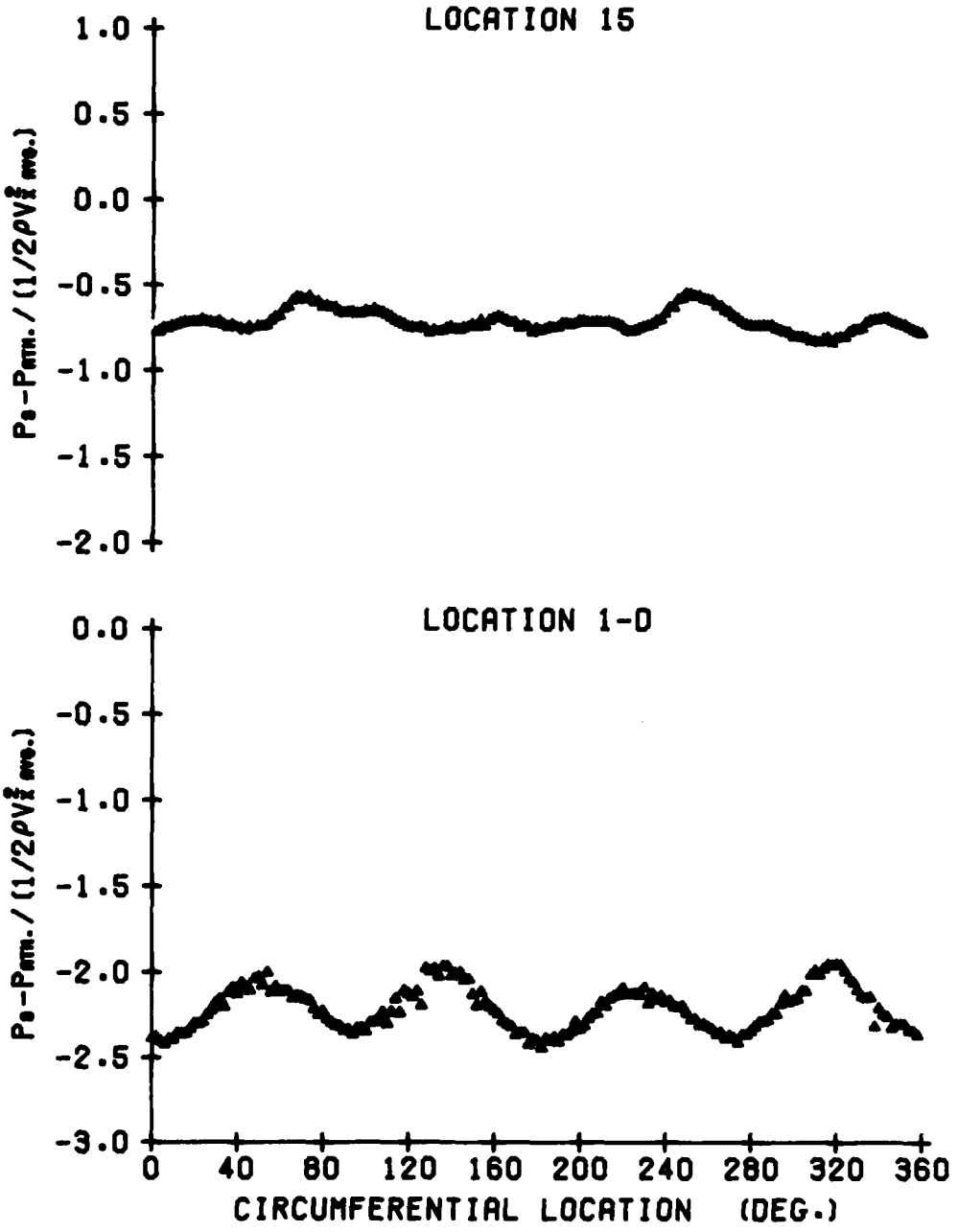

Figure 41. Static Pressure Distribution for the Four-Cycle Distortion with the Nine-Bladed Cambered Rotor, Measured at a Radial Distance of 2.328 cm from the Hub Surface

the same run conditions as tested in Figures 34 through 37, but these measurements were taken at the radial probe location nearest to the hub surface. Once again, the same distortion shapes and phenomena are observed that were discussed in the case of the six-bladed uncambered rotor in Section 4.2.1. By comparing the two sets of graphs, it is noticed that the magnitudes of the circumferential-mean axial and circumferential velocities and total and static pressures are similar but not identical upstream of the rotor for the various radial locations at which the measurements were taken. The slight changes observed in the magnitudes are due to the radial amplitude variations of the distortion screens as seen in Reference [35]. The probes were positioned far enough away from the solid boundaries so that the measurements were not affected by the boundary layers from the casing wall and the hub surface. Therefore, the changes in magnitude of the velocity and pressure distributions upstream of the rotor are caused by the design of the screens, and they exist in the absence of the rotor as well.

By examining Figures 36 and 40, it is seen that at the different radial locations, there is a minor difference, ten percent, in the magnitude of the circumferentially averaged total pressure downstream of the rotor. It is also noticed that the fluctuations in total pressure are greater at the tip than at the hub, and the frequency or harmonic content of the distortions is quite different. The fact that the magnitudes of the circumferentially averaged total pressure distributions downstream of the rotor are different at the two extreme spanwise locations is not too surprising since the solidity of the blades is different at these two locations, which also is a possible explanation for the observed changes in the total pressure variations at the two radial measurement locations.

Figure 39 shows an increase in magnitude of the local values of circumferential velocity downstream of the rotor near the hub over the circumferential velocity near the outer casing as shown in Figure 35. This merely indicates that the rotor turns the flow more near the hub than at the tip. The higher turning near the hub is a result of the rotor design which utilizes a free vortex spanwise loading.

Comparing Figures 34 and 38, it is seen that the magnitude of the circumferential-mean axial velocity distribution is greater at the measurement location near the tip than near the hub downstream of the rotor, location 15. This is due to the hub wall boundary layer since $V_{X\ avg}$ is the circumferentially averaged axial velocity at station 1-D. Figures 34 and 38 also show a noticeable difference in the harmonic content of the axial velocity distortion downstream of the rotor. The more random nature of the V_X variation in Figure 38 could be due to greater turbulent mixing near the hub of the rotor.

It is seen from Figures 37 and 41 that the magnitude of the static pressure downstream of the rotor is larger near the tip than near the hub of the rotor. The gradient in static pressure between the two radial locations is due simply to the spanwise loading on the blades.

A second series of distortion measurements was made with the nine-bladed cambered rotor to identify the effects of rotor-stator spacing on the inlet disturbance. For this purpose, eight cambered stator blades were installed in the AFRF, and a study was performed employing various distortion types and blade loadings. The measurements in this series of tests were all taken at the mean radius of the blades. One set of data was obtained with the leading edge of the stator blade row located two blade chord lengths (30.48 cm) behind the trailing edge of the rotor blade

row. As in the tests conducted previously, the probes were located at axial stations 1-D and 15. Another set of data was obtained with the stator row positioned one-half of a blade chord length (7.62 cm) downstream of the rotor trailing edge. For this series of tests, the upstream probe was located at station 1-D, but the downstream probe was moved forward to a new axial position designated as location 15-A. Location 15-A was positioned at an axial distance of 0.40 chord length downstream of the rotor trailing edge. This change in probe location was necessary so that the downstream probe remained upstream of the stator blade row.

Figures 42 through 45 present the axial velocity, circumferential velocity, total pressure, and static pressure distributions as a function of circumferential location for the two-cycle sinusoidal distortion with the stator row located two blade chord lengths behind the trailing edge of the rotor. In contrast to these, Figures 46 through 49 show the axial and circumferential velocities and the total and static pressures measured using the same operating conditions with the stator blades located one-half of a blade chord length behind the rotor.

It is quickly observed that the different rotor-stator spacings had no effect whatsoever on the data measured upstream of the rotor, location 1-D. The energy added to the flow was the same in both cases since the measurements were all made at the mean radius and the same operating conditions were tested. Thus, the total pressure variation is unchanged downstream of the rotor as seen in Figures 44 and 48. The most important characteristic of the flow field which is observed by changing the rotor-stator spacing is the shapes of the axial velocity, circumferential velocity, and static pressure distributions in Figures 46, 47, and 49, respectively. A periodic fluctuation in these distributions occurs

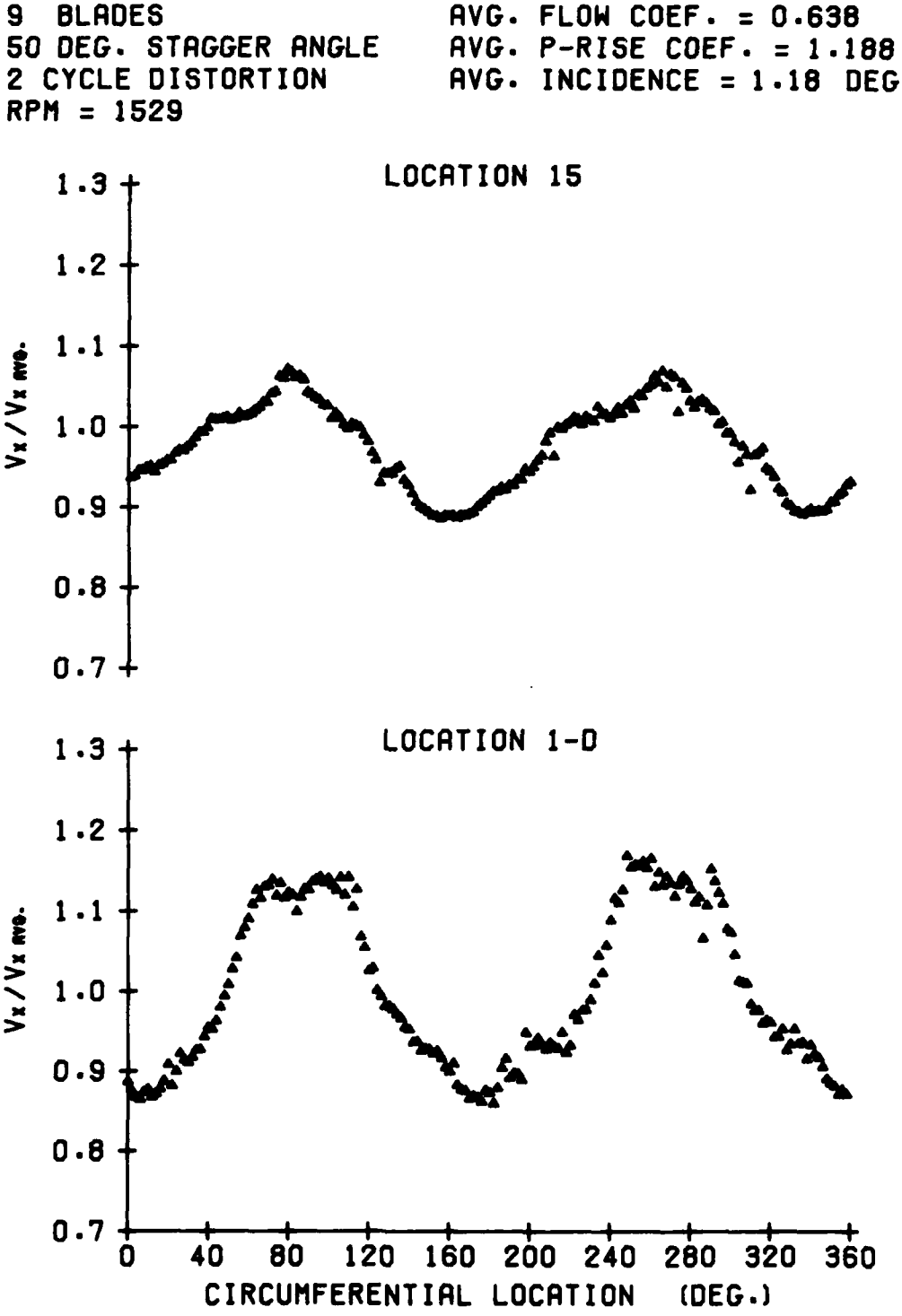

Figure 42. Axial Velocity Distribution for the Two-Cycle Distortion with the Nine-Bladed Cambered Rotor for a Rotor-Stator Spacing of Two Blade Chord Lengths (30.48 cm)

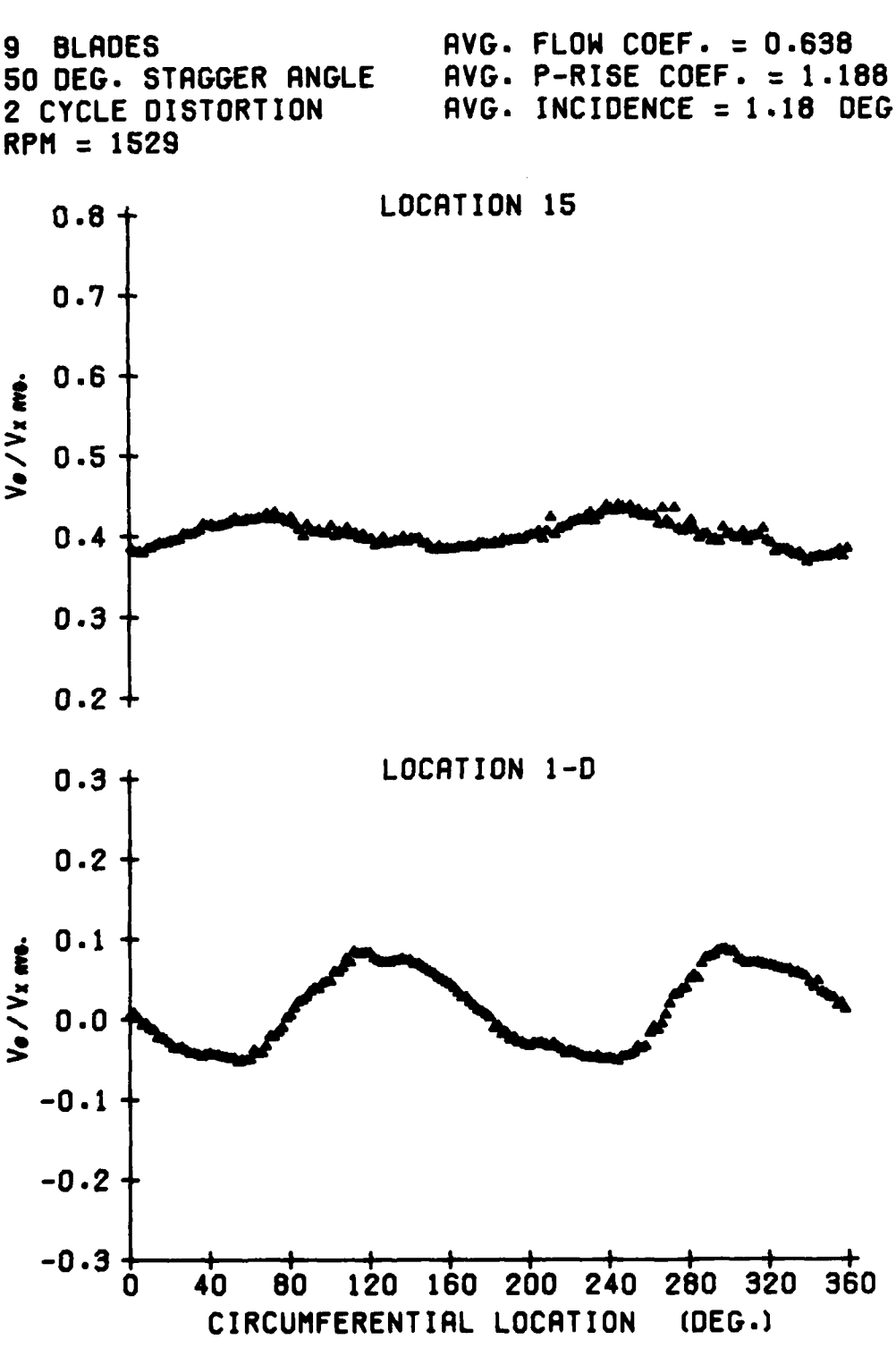

Figure 43. Circumferential Velocity Distribution for the Two-Cycle Distortion with the Nine-Bladed Cambered Rotor for a Rotor-Stator Spacing of Two Blade Chord Lengths (30.48 cm)

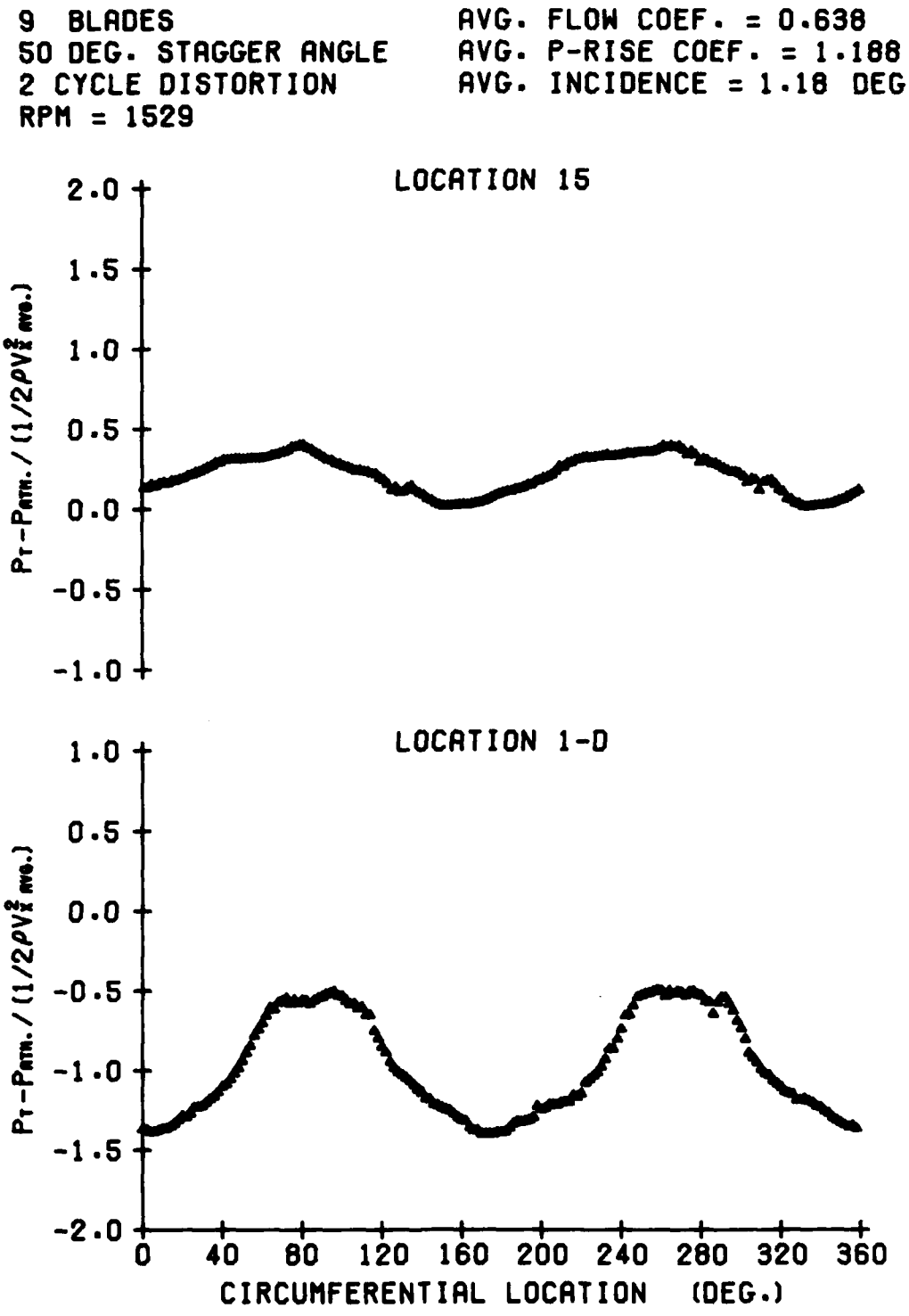

Figure 44. Total Pressure Distribution for the Two-Cycle Distortion with the Nine-Bladed Cambered Rotor for a Rotor-Stator Spacing of Two Blade Chord Lengths (30.48 cm)

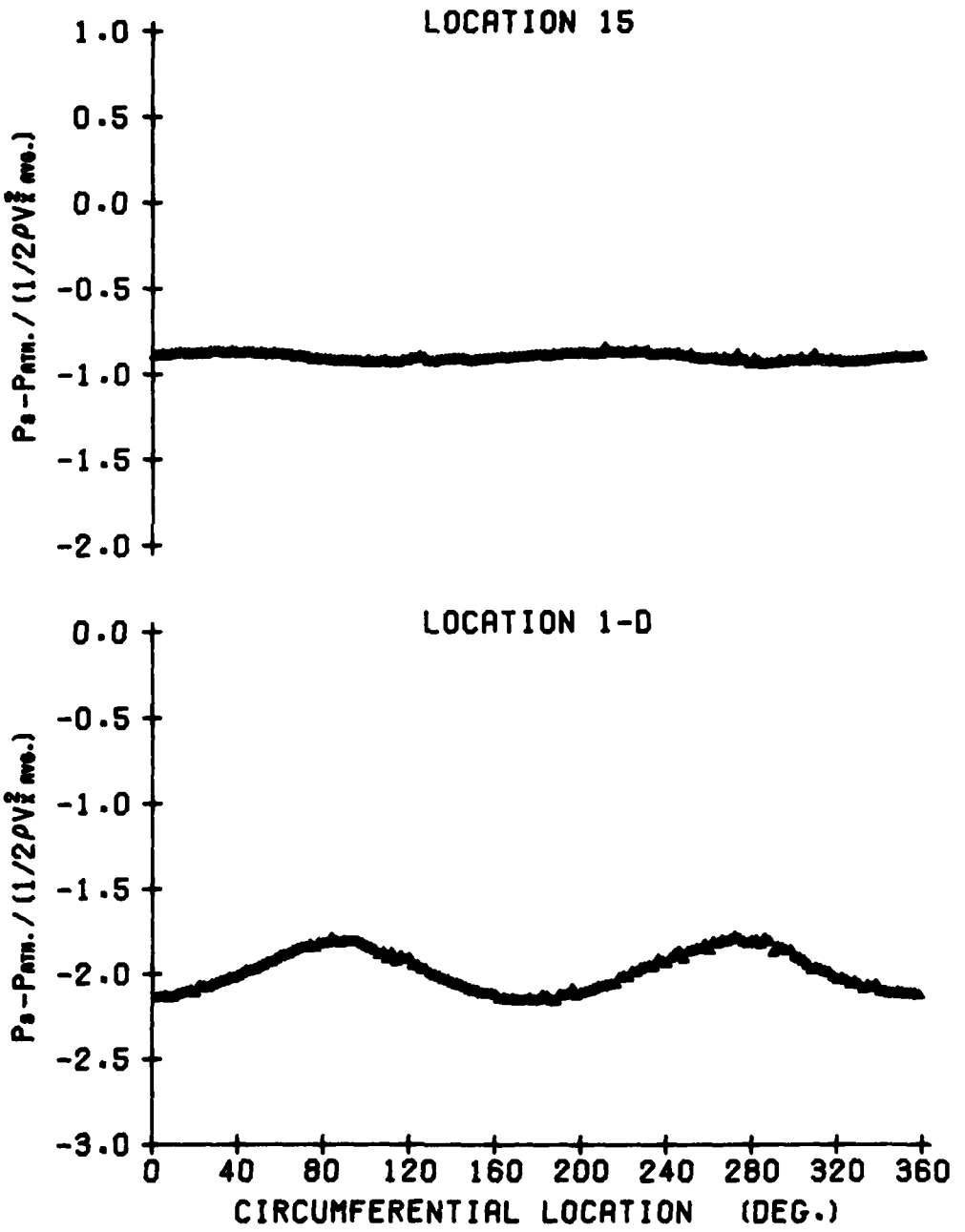

Figure 45. Static Pressure Distribution for the Two-Cycle Distortion with the Nine-Bladed Cambered Rotor for a Rotor-Stator Spacing of Two Blade Chord Lengths (30.48 cm)

9 BLADES
50 DEG. STAGGER ANGLE
2 CYCLE DISTORTION
RPM = 1529

AVG. FLOW COEF. = 0.632
AVG. P-RISE COEF. = 1.210
AVG. INCIDENCE = 1.56 DEG.

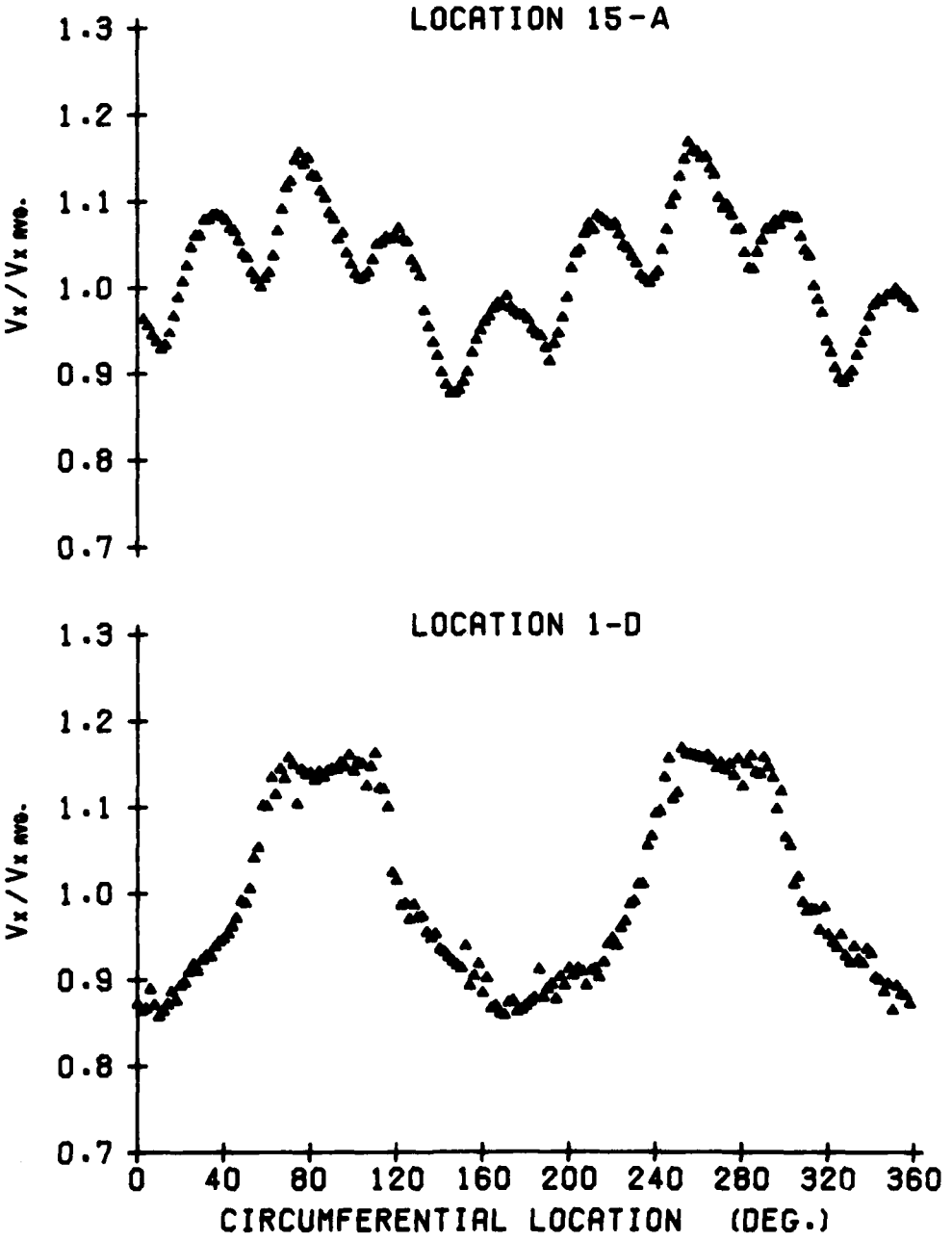

Figure 46. Axial Velocity Distribution for the Two-Cycle Distortion with the Nine-Bladed Cambered Rotor for a Rotor-Stator Spacing of 0.5 Blade Chord Lengths (7.62 cm)

9 BLADES
50 DEG. STAGGER ANGLE
2 CYCLE DISTORTION
RPM = 1529

AVG. FLOW COEF. = 0.632
AVG. P-RISE COEF. = 1.210
AVG. INCIDENCE = 1.56 DEG.

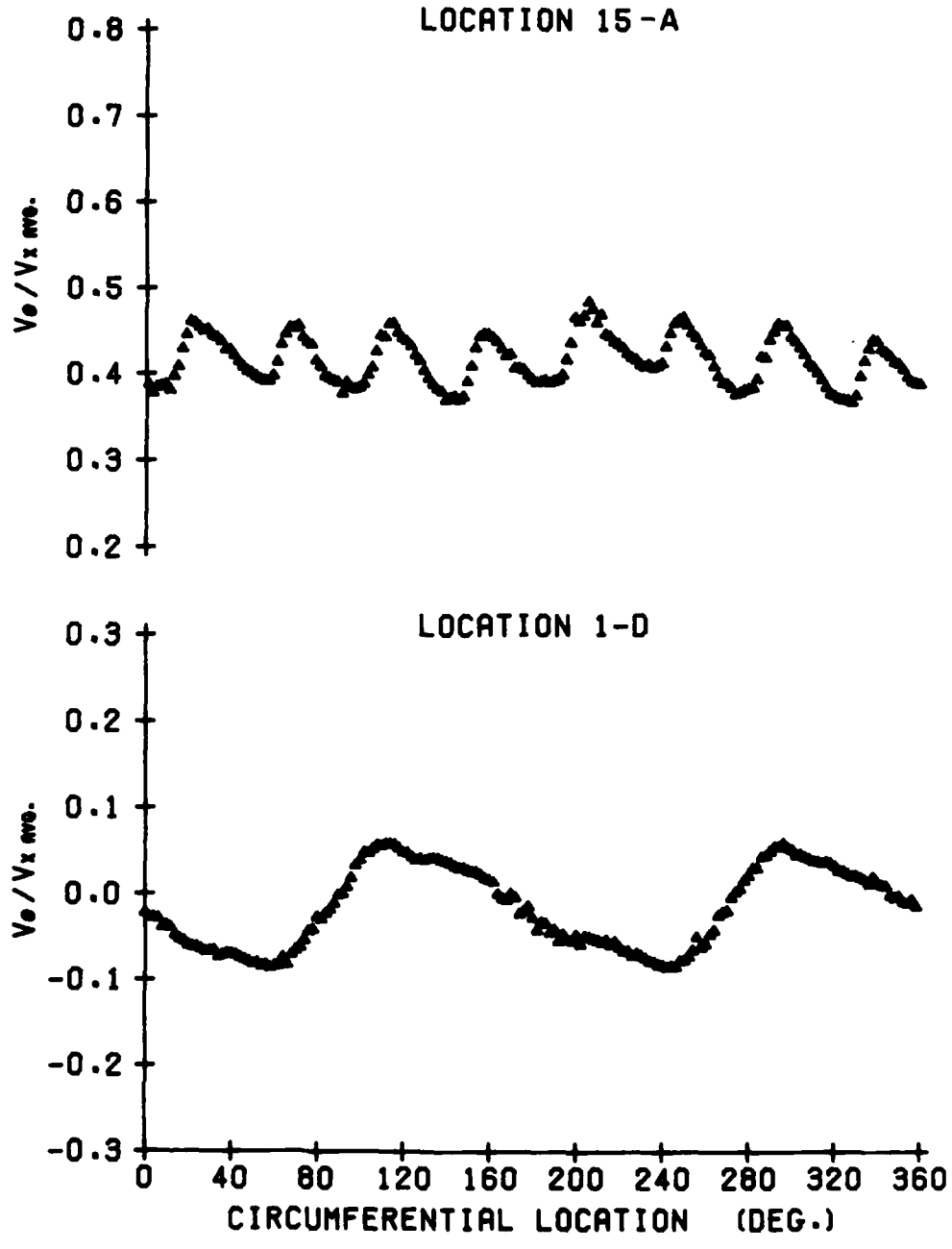

Figure 47. Circumferential Velocity Distribution for the Two-Cycle Distortion with the Nine-Bladed Cambered Rotor for a Rotor-Stator Spacing of 0.5 Blade Chord Length (7.62 cm)

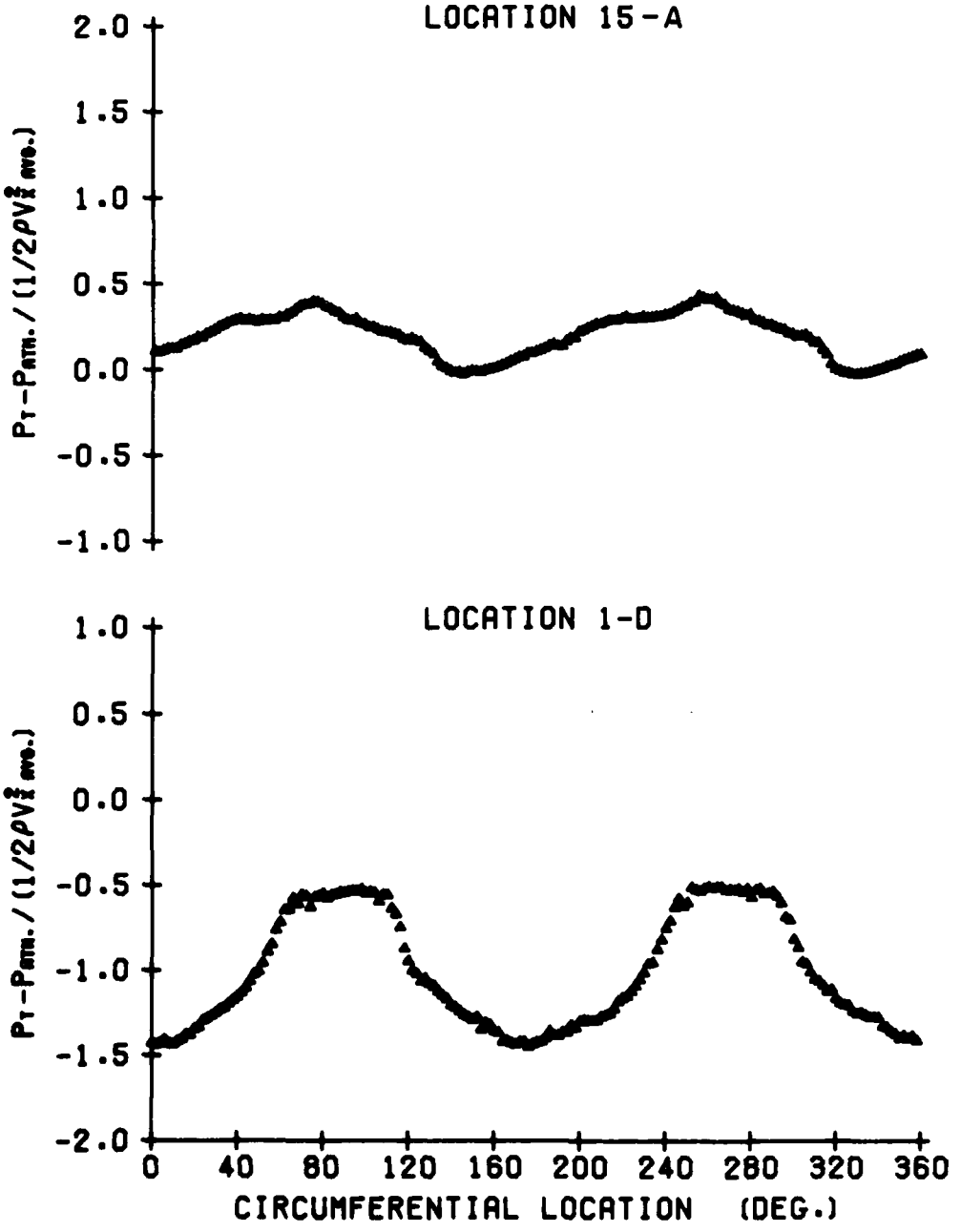

Figure 48. Total Pressure Distribution for the Two-Cycle Distortion with the Nine-Bladed Cambered Rotor for a Rotor-Stator Spacing of 0.5 Blade Chord Lengths (7.62 cm)

9 BLADES
50 DEG. STAGGER ANGLE
2 CYCLE DISTORTION
RPM = 1529

AVG. FLOW COEF. = 0.632
AVG. P-RISE COEF. = 1.210
AVG. INCIDENCE = 1.56 DEG.

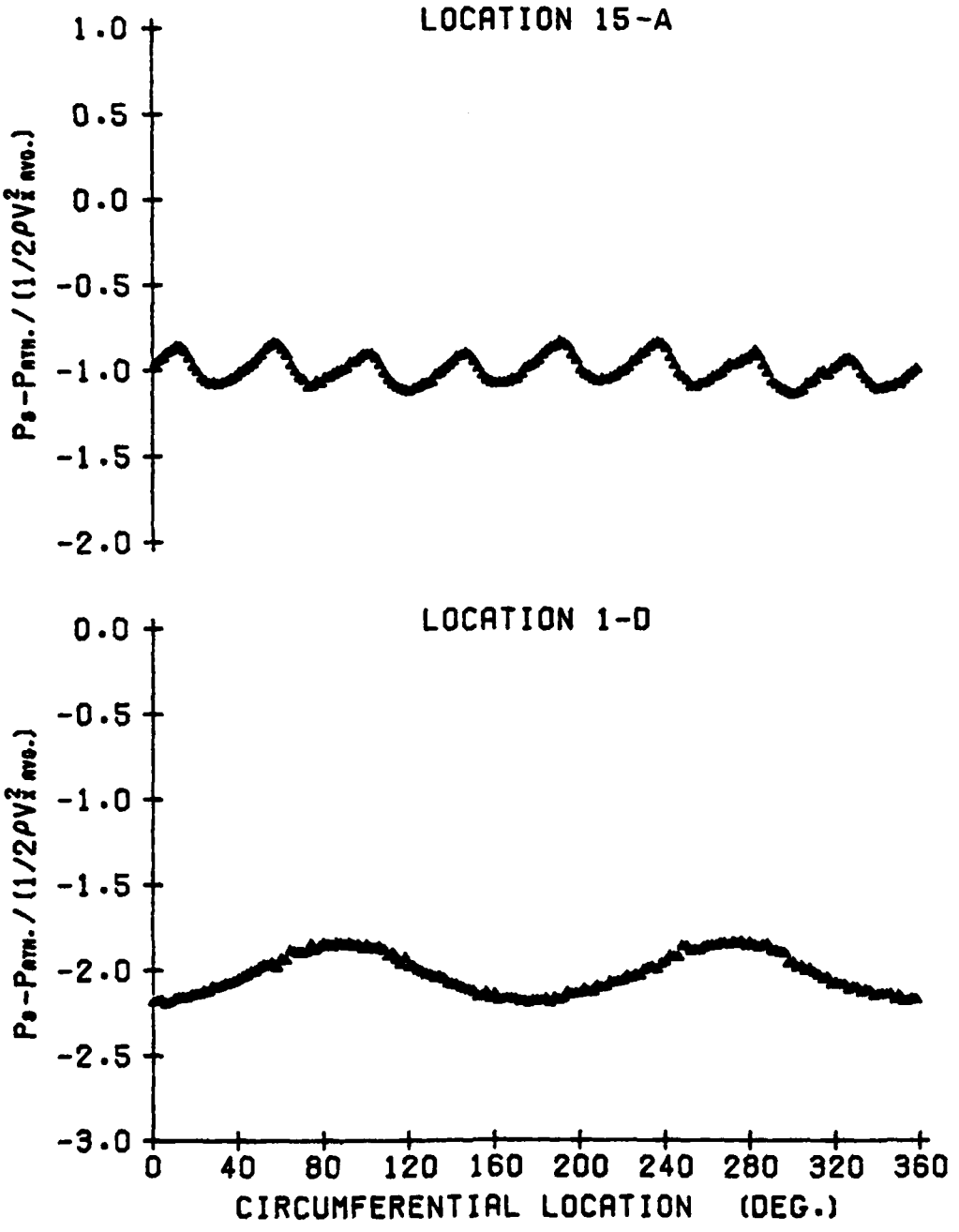

Figure 49. Static Pressure Distribution for the Two-Cycle Distortion with the Nine-Bladed Cambered Rotor for a Rotor-Stator Spacing of 0.5 Blade Chord Lengths (7.62 cm)

downstream of the rotor. It is also important to note that the fluctuation goes through eight cycles in a complete circumferential survey of 360 degrees. By looking at Figures 46 and 49, the axial velocity and static pressure variations downstream of the rotor are seen to be directly out of phase which is expected from Bernoulli's equation. The eight-cycle periodic type of fluctuation is attributed to a blockage effect due to the close proximity of the downstream probe to the stator blades when the stator blades are located in the forward position, only one-half of a chord length behind the rotor. With the stator row in the forward position, the probe was placed an axial distance of only 0.6 inch (1.524 cm) in front of the stator blades. The eight troughs in the axial velocity fluctuation (i.e., the peaks in the static pressure distribution) represent the points at which the probe was positioned directly in front of the stator blades. Between the blades, the velocity is accelerated and this is shown by the peaks in the axial velocity variation at location 15-A in Figure 46.

4.3 Distortion Attenuation

The purpose of this section is to examine some of the overall trends observed in the distortion data as a function of the type of distortion screen and rotor operating variables. Because of the large amount of data associated with the objective of providing a data base for subsequent studies, it is not possible to examine and evaluate all of the distortion characteristics in this paper. For this reason, only the attenuation (or amplification) of the axial velocity and total pressure will be discussed. An attempt has been made to point out the most significant parameters involved, and this should serve as an aid in conducting future studies in this area.

Information concerning the attenuation of an inlet distortion through a blade row is important when designing a multi-stage turbomachine, since the latter stages will be subjected to the exit flow of the upstream stages. It may be desirable, if possible, to completely eliminate a distortion in the first few stages of a compressor so that the latter stages can operate in a uniform flow with improved performance and stability. The rate and amount of attenuation, however, may be limited by unsteady forces or losses in the early stages.

The fact that a total pressure distortion will be attenuated by a rotor is easily understood from a quasi-steady viewpoint. Higher incidence angles in the low velocity region will result in a larger total pressure rise (unless separation occurs) than in the remaining regions and thus make up some of the total pressure defect. However, the effects of the distortion frequency, rotor design, and operating conditions on the distortion attenuation are not easily assessed theoretically and therefore, the experiments of this study can provide some of this information.

In order to quantify the attenuation of a distortion, a means of representing the amplitude of the distortion is necessary. One method of quantifying the size of a distortion is to represent the data as a Fourier series so that the amplitudes of the various harmonics can be examined and compared. For this reason, the dimensionless axial velocity and total pressure data were Fourier analyzed by computing the coefficients of a conventional Fourier series by using a numerical integration scheme. The Fourier analysis routine was written and programmed by Yocum for use on the IBM 1130 Computing System. The coefficients of the series were then converted to an amplitude and a phase angle so that the data could be represented in the following form:

$$\frac{P_T}{1/2\rho V_{x\ avg}^2} \text{ OR } \frac{V_X}{V_{X\ avg}} = \frac{A_o}{2} + \sum_{n=1}^{\infty} A_n \sin(n\theta - \phi n) \ . \qquad (35)$$

The use of Equation (35) for representing the data is especially convenient for describing the sinusoidal distortions, where one harmonic will be dominant and can be used to represent the distortion amplitude. Figure 50 contains plots of the amplitudes, A_n, of the dimensionless total pressure and axial velocity distortions versus the harmonic number, n, for a four-cycle distortion. Three sets of data are presented on each graph; one set describes the distortion without the rotor installed, while the other two describe the distortions at locations 1-D and 15 when the uncambered rotor is operating. This type of plot is useful for demonstrating the harmonic content of the distortion and for identifying the dominant harmonics. The figure also shows how each harmonic is affected by the presence of the rotor. As expected for the four-cycle distortion, Figure 50 shows that the fourth harmonic is very dominant, and, thus, the amplitudes of the fourth harmonics can be used to describe the distortion size. Similarly, the fundamental harmonic of the one-, two-, and six-cycle sinusoidal distortions can be used to represent their distortion amplitudes.

The square-wave distortions were also represented in the form of Equation (35) so that the harmonic content could be examined and the attenuation of the individual harmonics compared with the attenuation observed for the sinusoidal distortions. Plots similar to those in Figure 50 are presented for a 90 degree square distortion in Figure 51. In this case, it is found that the first two harmonics are significant. Although both of these harmonics could be used to analyze the attenuation

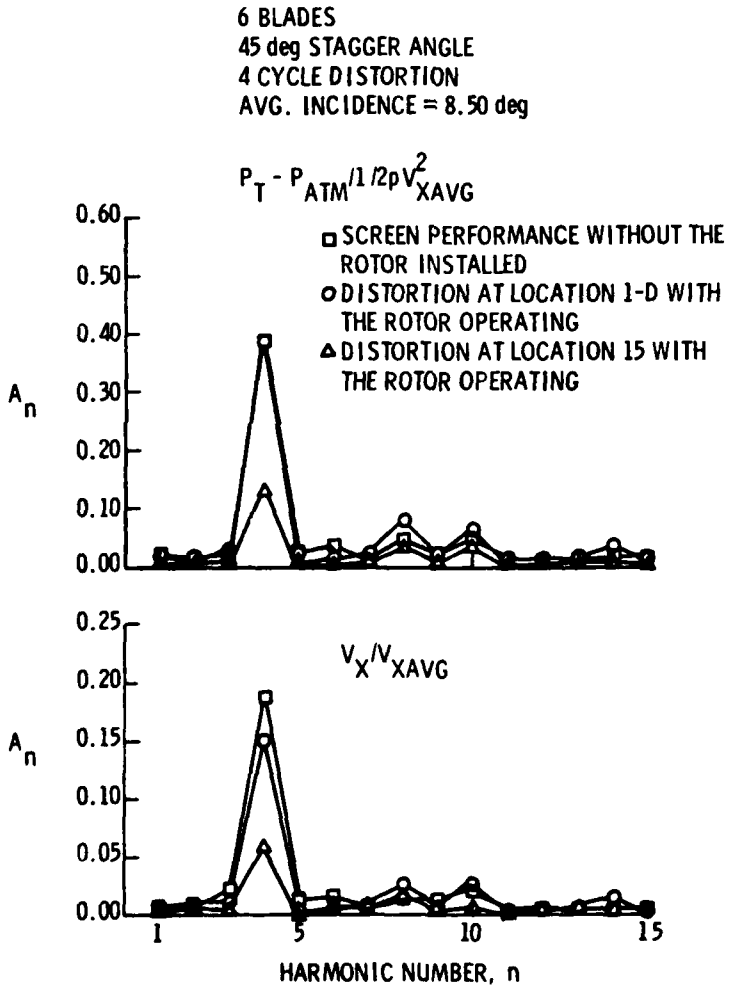

Figure 50. Dimensionless Total Pressure and Axial Velocity Harmonic Amplitudes as a Function of the Harmonic Number, n, for a Four-Cycle Distortion

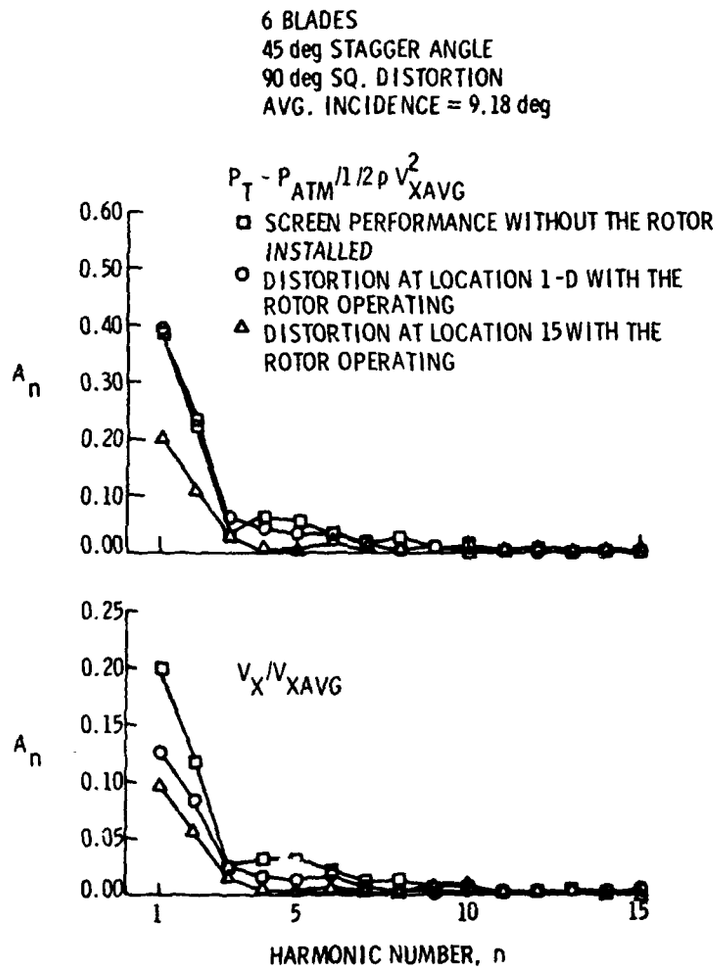

Figure 51. Dimensionless Total Pressure and Axial Velocity Harmonic Amplitudes as a Function of the Harmonic Number, n, for a 90 Degree Square Distortion

of the square distortions, no single parameter from the Fourier series can be used to properly represent the distortion size. Therefore, in addition to Fourier analyzing the data, a single parameter representing the amplitude of the square distortions was calculated by taking the difference between the maximum and minimum values of the axial velocity and total pressure. Thus, the amplitudes of the square inlet distortions were defined as:

$$A_{P_T} = \frac{P_{T\ max} - P_{T\ min}}{1/2\rho V_{X\ avg}^2} \tag{36}$$

and

$$A_{V_X} = \frac{V_{X\ max} - V_{X\ min}}{V_{X\ avg}} \tag{37}$$

These definitions may appear to be obvious ones since, for a perfect square distortion, A is simply the difference in magnitude between the distorted and undistorted sectors. However, it is necessary to define A with the maximum and minimum values because downstream of the rotor the remaining distortion is no longer square. This fact is shown in Figure 31 where the total pressure variation for a square inlet distortion is plotted and the amplitude as defined by Equation (36) is indicated.

For both the sinusoidal and the square distortions, the attenuation is presented as a ratio of the distortion amplitude with the rotor operating to the amplitude of the distortion at the same axial location without the rotor operating. With the data presented in this manner, the amplitude ratio can range from a value of zero, indicating the distortion was completely eliminated, to a value of one, indicating no attenuation. Values greater than one mean that the distortion was amplified.

4.3.1 Results for the Six-Bladed Uncambered Rotor. Figure 52 presents the attenuation for the six-cycle sinusoidal distortion in the form of the amplitude ratio of the sixth harmonic versus the circumferential average incidence angle for the various stagger angles tested. Both the axial velocity and total pressure amplitude ratios are presented for both upstream and downstream locations, with the three symbols for each location indicating the different blade stagger angles. It is seen from Figure 52 that both the total pressure and axial velocity attenuation upstream of the rotor are not strongly influenced by a change in incidence, or mean blade loading. Downstream of the rotor, the V_X and P_T distortions show increasing attenuation (i.e., a decreasing amplitude ratio) as the incidence angle is increased for the rotor configurations having all three blade stagger angles. In Reference [37], incidence angle was found to have very little effect on the distortion attenuation with the twelve-bladed uncambered rotor. Thus, it is believed that an influence due to the space-to-chord ratio is causing the observed dependence of incidence on the attenuation for the six-bladed rotor. In the present study, there is not a sufficient amount of data to prove this hypothesis.

The most important characteristic of the data revealed in Figure 52 is the influence of the blade stagger angle on the amount of attenuation occurring downstream of the rotor. The rotor configurations with the higher blade stagger angles produce a larger attenuation of both the total pressure and axial velocity. The increase in attenuation of the total pressure distortion can be partially attributed to the steepening of the pressure rise versus incidence performance curve which occurs for the higher stagger angles.

With the exception of the effect of incidence on the distortion attenuation, the general trends observed and discussed here for the

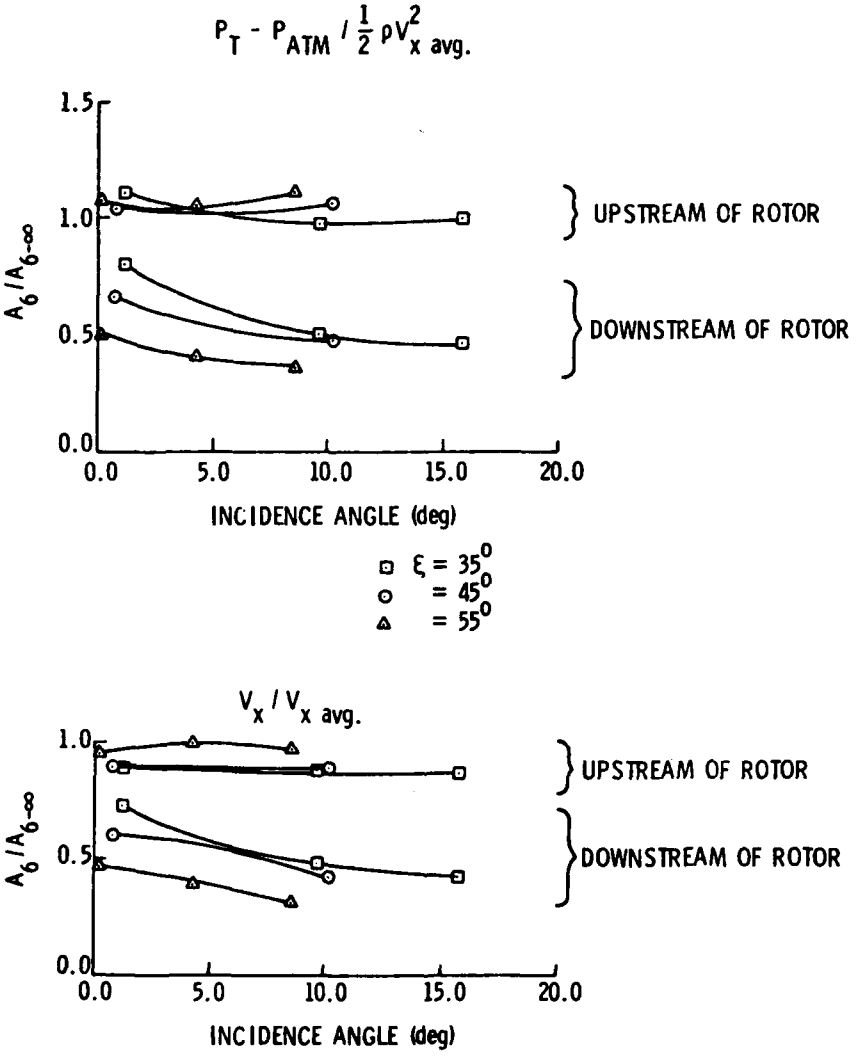

Figure 52. Measured Axial Velocity and Total Pressure Distortion Attenuation versus Incidence Angle for a Six-Cycle Sinusoidal Distortion with the Uncambered Rotor

six-bladed uncambered rotor were also observed for the uncambered rotor with twelve blades, as discussed in Reference [37]. By comparing the two sets of data, it is found that the magnitudes of both the total pressure and axial velocity amplitude ratios are greater for the six-bladed rotor than for the twelve-bladed rotor. Thus, the effect of decreasing the rotor space-to-chord ratio from 1.356 to 0.676 is to increase the amount of attenuation of the total pressure and axial velocity inlet distortions downstream of the rotor.

The next set of attenuation data to be presented for the uncambered rotor is the amplitude ratios of the total pressure and axial velocity distortions as a function of incidence angle for the two square-shaped inlet distortions tested. These data are presented in Figures 53 and 54 for the 90 degree and 180 degree distortions, respectively. The total pressure distortion amplitude is defined by Equation (36), and the axial velocity distortion amplitude is defined by Equation (37). As done previously for the sinusoidal distortion, the data on the figures are presented with the symbols representing the various blade stagger angles.

Figures 53 and 54 show that the effect of incidence or blade loading on the attenuation of the axial velocity and total pressure distortions is minor. The distortions undergoe approximately a five to ten percent change in attenuation over the range of incidence angles tested. It is also found that the stagger angle does not significantly affect the attenuation upstream or downstream of the rotor for the square distortions.

One important observation to be made in Figure 53 for the 90 degree square distortion is the change in the total pressure distortion amplitude upstream of the rotor. It was pointed out in Section 4.2.1 that the magnitude of the total pressure distortion upstream of the rotor had

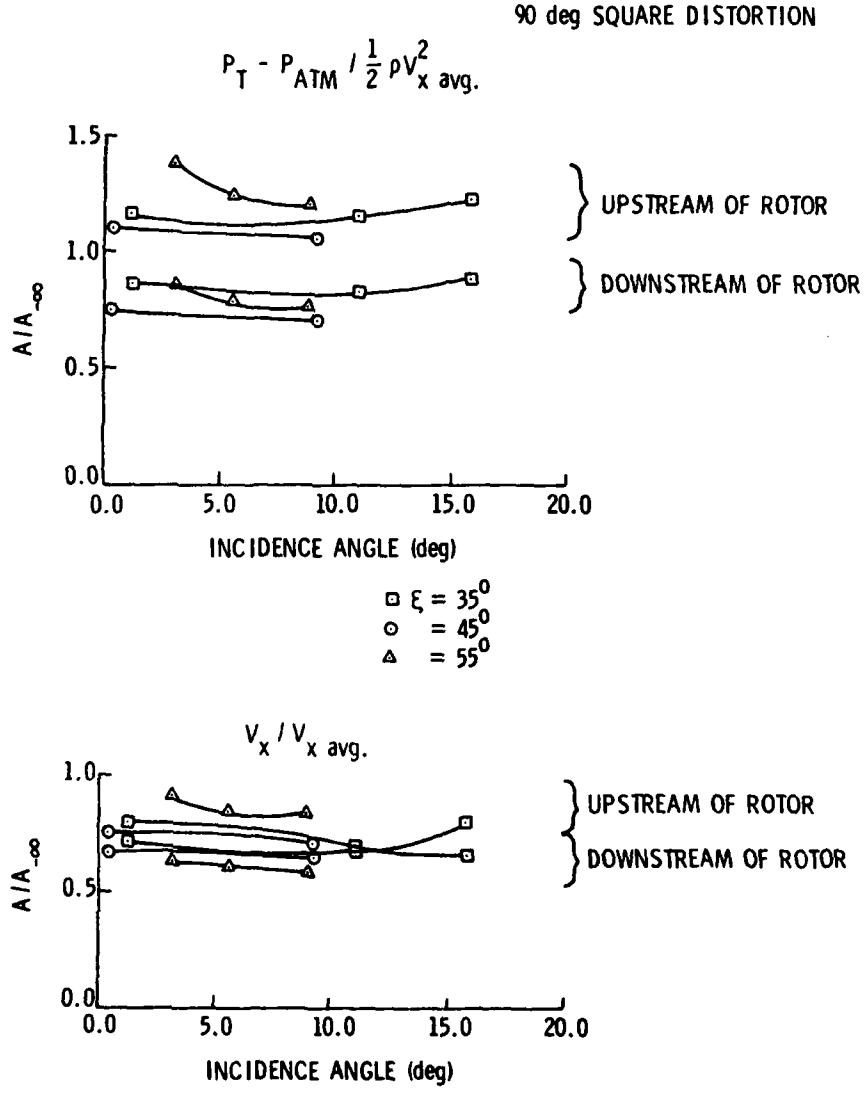

Figure 53. Measured Axial Velocity and Total Pressure Distortion Attenuation versus Incidence Angle for a 90 Degree Square Distortion with the Uncambered Rotor

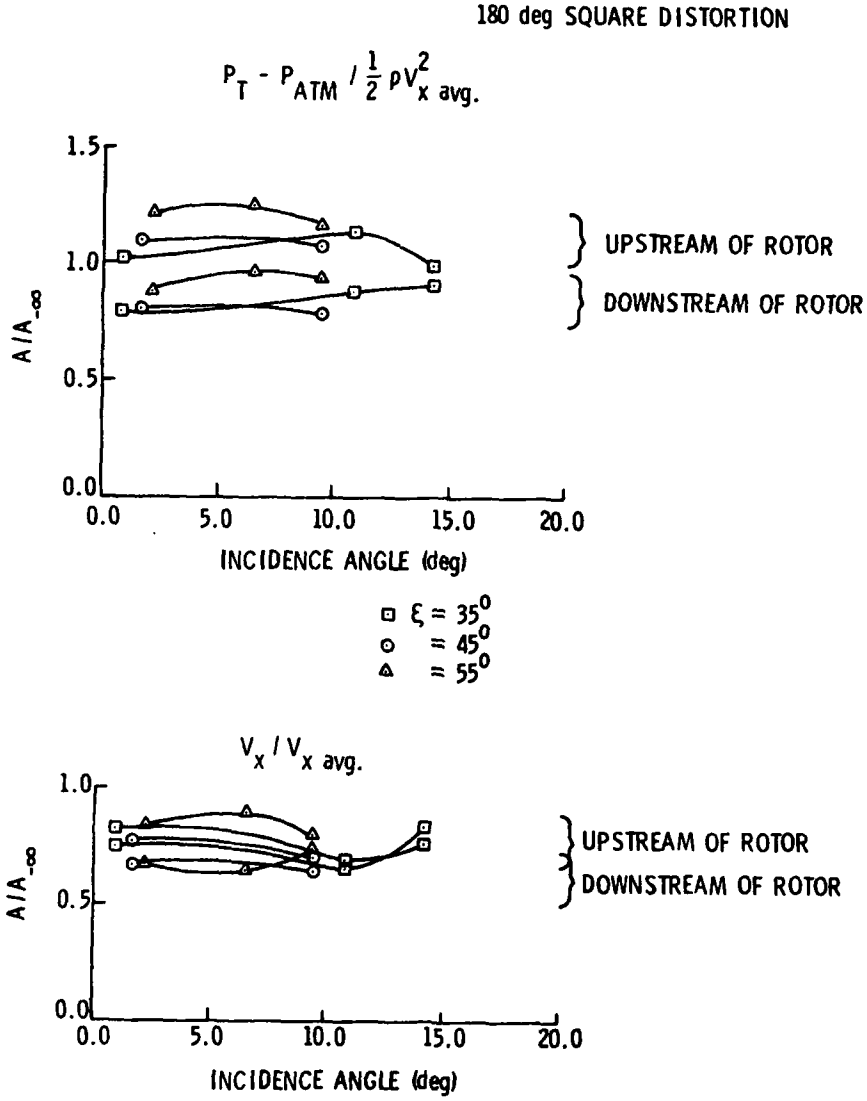

Figure 54. Measured Axial Velocity and Total Pressure Distortion Attenuation versus Incidence Angle for a 180 Degree Square Distortion with the Uncambered Rotor

increased with the rotor installed in the case of a 90 degree square distortion. This phenomenon is shown clearly in Figure 53 where the total pressure amplitude ratios upstream of the rotor are greater than one. It was suggested in Section 4.2.1 that the increase in amplitude is due to a radial total pressure gradient produced by the screen followed by a radial shift in the streamlines upstream of the rotor. However, for the sinusoidal distortions, the variation is not significantly large and the mean amplitude ratio is approximately 1.0 (see Figure 52).

The main observation which can be made from Figures 53 and 54 is the influence of the circumferential extent or the width of the distortion. It is seen that the magnitudes of the axial velocity amplitude ratios upstream and downstream of the rotor are quite similar for both the 90 degree and 180 degree square distortions. The total pressure amplitude ratios downstream of the rotor also have approximately the same magnitude. However, it appears from the figures that the 90 degree total pressure distortion has undergone a greater amplification upstream of the rotor than the 180 degree distortion. The attenuation of the two square distortions across the rotor is approximately the same since the axial velocity and total pressure amplitude ratios downstream of the rotor are the same. Due to the hypothesis that three-dimensional flows are involved in amplifying the inlet distortion, it cannot be concluded from this data that a larger amplification of the total pressure distortion upstream of the rotor will always be observed for smaller width distortions.

From the data taken with the sinusoidal distortions, the variation in the attenuation was found to be much greater as a function of distortion frequency than the variation observed with changes in incidence angle. Therefore, the remaining data with the uncambered rotor for the sinusoidal

distortions will be presented as a function of the reduced frequency, which is a dimensionless frequency parameter defined as:

$$\omega = \frac{2\pi}{\ell_c} \cdot \frac{c}{2} \quad . \tag{38}$$

This definition stems from unsteady aerodynamic theory and is represented as a ratio of the blade chord length to the wavelength of the disturbance along the chord. The typical definition of reduced frequency is based on the half-chord, not the chord length, as shown in Equation (38). The wavelength of the disturbance along the chord, ℓ_c, is related to the wavelength along the pitch, ℓ, in the following manner:

$$\ell_c = \frac{\ell}{\sin \xi} \quad , \tag{39}$$

where ξ is the stagger angle. The relation in Equation (39) assumes that the gust or disturbance is convected, i.e., it moves past the blade at the same velocity as the free-stream velocity. Substituting Equation (39) into Equation (38), the reduced frequency becomes:

$$\omega = \frac{\pi c}{\ell} \sin \xi \quad . \tag{40}$$

Equation (40) is the definition of ω which is used throughout this study. As a physical interpretation of ω, it can be shown that the reduced frequency represents the number of distortion cycles across the blade chord.

Figures 55 and 56 present the amplitude ratio of the total pressure and axial velocity distortions versus ω for constant values of incidence angle of zero and eight degrees, respectively. It is seen from both Figures 55 and 56 that an increase in reduced frequency decreases the

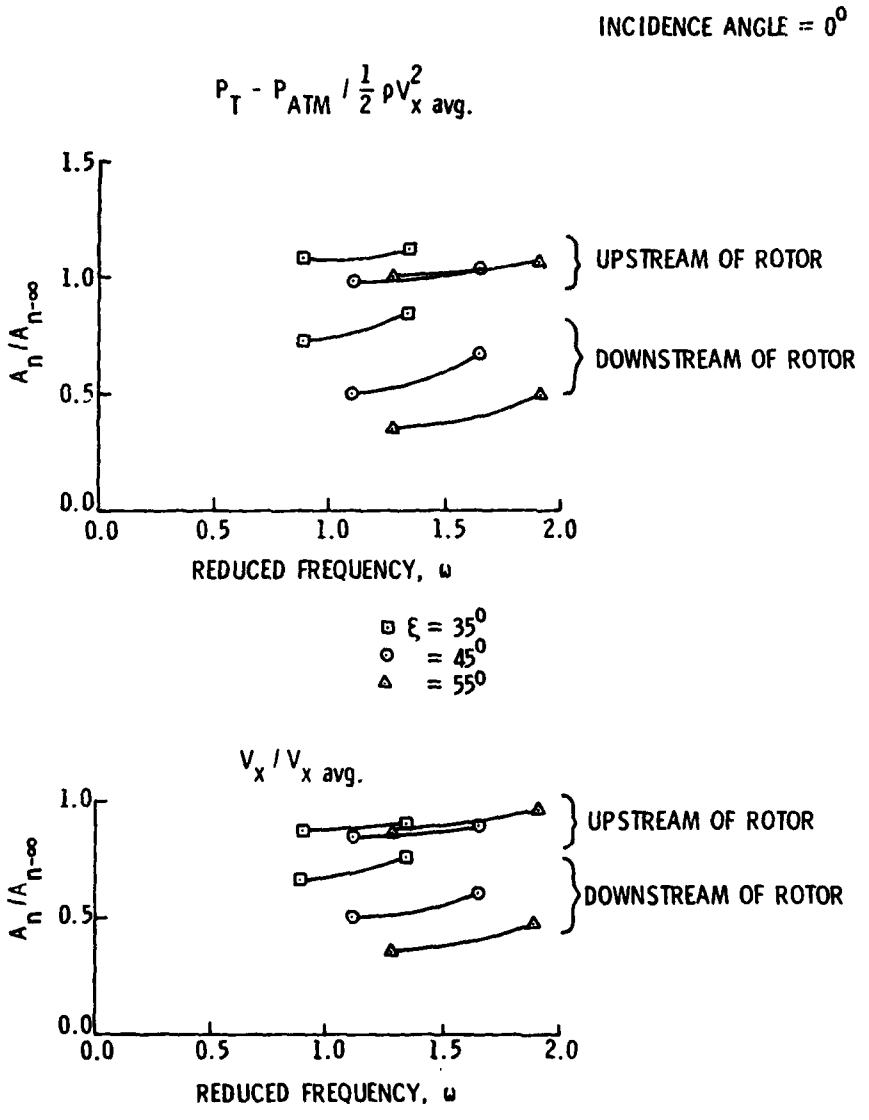

Figure 55. Amplitude Ratio versus Reduced Frequency for a Constant Mean Incidence Angle of Zero Degrees with the Uncambered Rotor

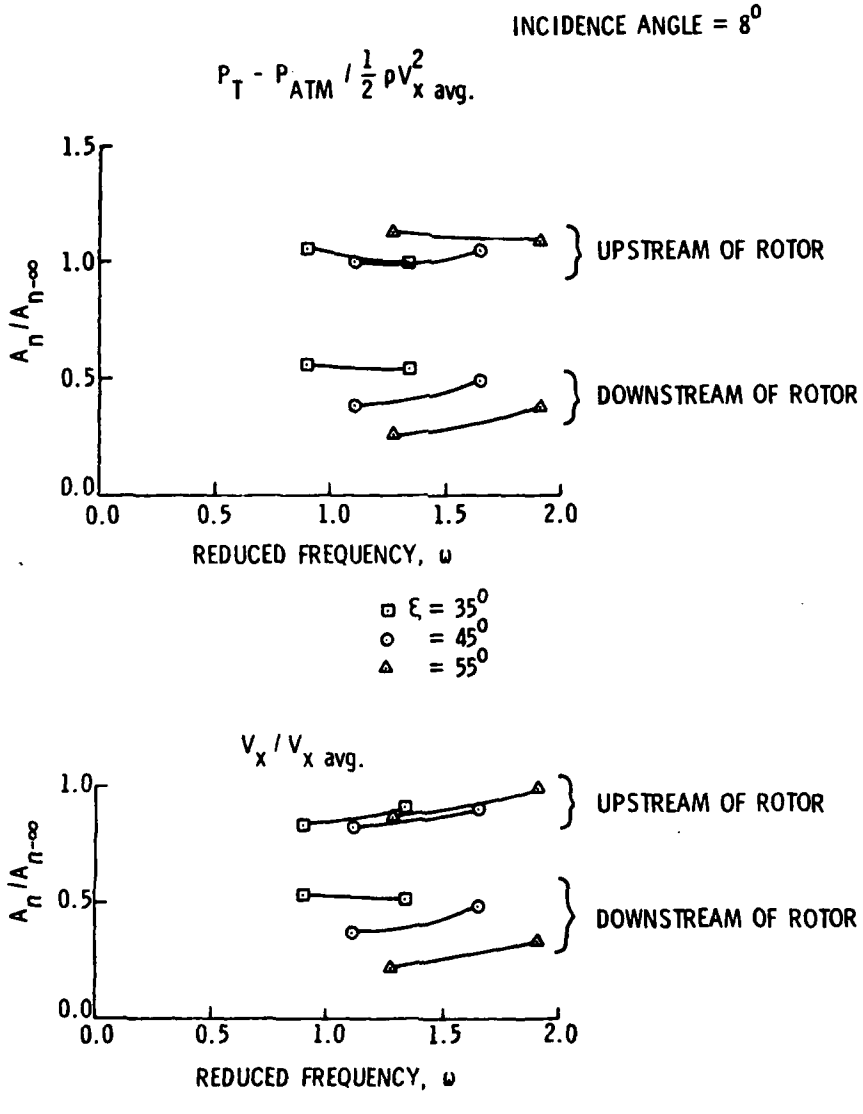

Figure 56. Amplitude Ratio versus Reduced Frequency for a Constant Mean Incidence Angle of Eight Degrees with the Uncambered Rotor

attenuation of the total pressure and axial velocity distortions downstream of the rotor. In the case of an eight-degree incidence angle, there is a slight increase in the attenuation of the total pressure distortion upstream of the rotor configurations having blade stagger angles of 35 and 55 degrees. The decrease in the distortion attenuation downstream of the rotor with increasing values of ω is contrary to the results obtained with the twelve-bladed rotor in Reference [37].

It is suggested that this decrease in attenuation occurs because the reduced frequency is changing to give the situation where the number of blades on the rotor and the number of distortion cycles are equal, i.e., the six-bladed rotor and six-cycle distortion. In this case, the wavelength of the disturbance along the pitch direction is equal to the blade spacing, and each blade will experience the same disturbance velocity at a given time. It is hypothesized that if higher values of reduced frequency (for instance, nine-cycle and twelve-cycle sinusoidal distortions) had been tested in this investigation, an increase in attenuation would be observed at the higher values of ω. It is further hypothesized that if a twelve-cycle sinusoidal distortion had been tested in the study in Reference [37], a decrease in attenuation would have been observed at the corresponding value of reduced frequency. These hypotheses seem to be supported by the attenuation data for the nine-bladed cambered rotor which will be presented in the following section, but further experimentation with the six-bladed rotor would be required to completely verify the assumption.

4.3.2 Results for the Nine-Bladed Cambered Rotor. The next series of attenuation data to be presented shows the results obtained with the nine-bladed cambered rotor. These data are presented in a manner similar to the data for the uncambered rotor. The effect of stagger angle can no longer be considered since the cambered rotor has a fixed stagger angle of 50 degrees at its mean radius. The effects of rotor-stator spacing and radial probe location were studied with the cambered rotor; therefore, the influence of these variables on the attenuation of the axial velocity and total pressure distortions will now be discussed.

Figure 57 shows the attenuation for the four-cycle sinusoidal distortion in the form of the amplitude ratio of the fourth harmonic versus the circumferential-mean incidence angle for the two rotor-stator spacings investigated. Both the axial velocity and total pressure amplitude ratios are presented for both locations, with the circles indicating a rotor-stator spacing of two blade chord lengths (30.48 cm) and the squares denoting a rotor-stator spacing of 0.5 blade chord length (7.62 cm). All measurements were taken at the mean radius of the blade. The first thing to be noticed in Figure 57 is that rotor-stator spacing has no effect on the total pressure and axial velocity distortions downstream of the rotor. This indicates that the inlet distortion is attenuated within at least 0.4 chord length of the rotor. Once again, it is seen that the total pressure distortion is slightly amplified upstream of the rotor, and this amplification is very small. Another important observation to be made from Figure 57 is the large amount of attenuation experienced between the upstream and downstream locations for both the axial velocity and total pressure distortions. The cambered rotor is seen to almost completely

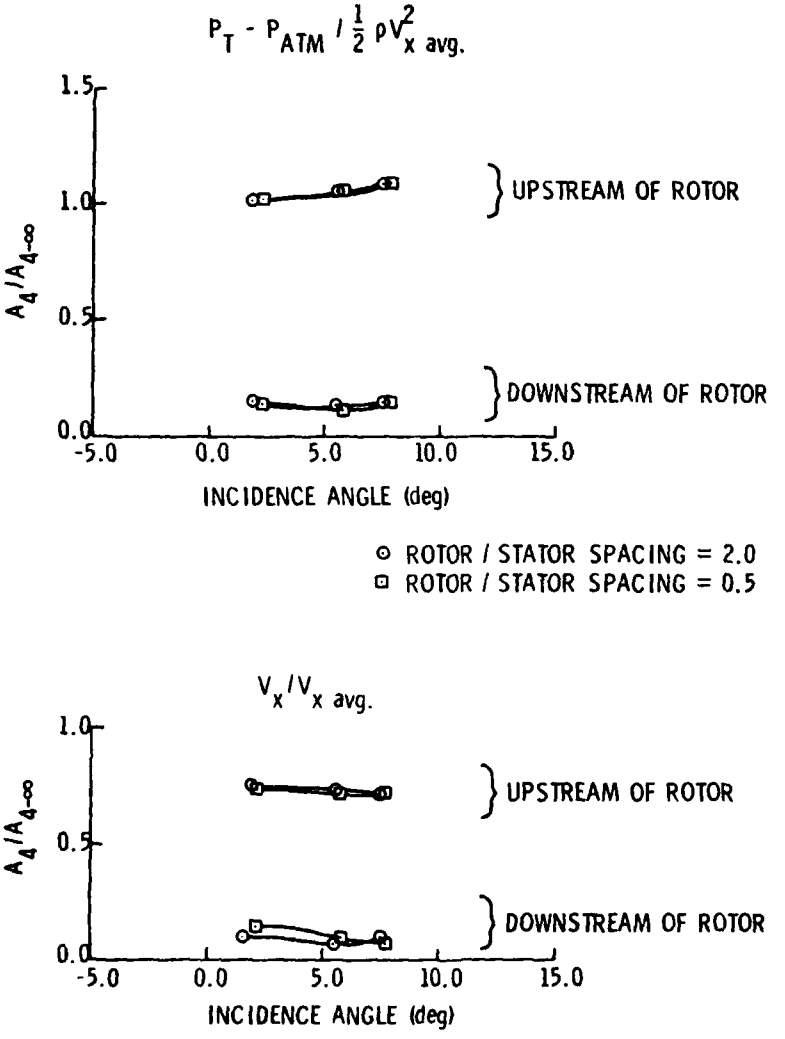

Figure 57. Measured Axial Velocity and Total Pressure Distortion Attenuation versus Incidence Angle for a Four-Cycle Sinusoidal Distortion with the Cambered Rotor

eliminate the four-cycle sinusoidal inlet distortion. It can be pointed out that this large amount of attenuation downstream of the rotor was also observed for the six-cycle distortion; however, it was not found to occur for the one- and two-cycle sinusoidal distortions. In all cases, however, it was commonly observed that both the incidence angle and the rotor-stator spacing had a negligible effect on the distortion attenuation. The negligible effect of incidence or blade loading on the attenuation is attributed to the linear nature of the performance curve corresponding to the range of operating conditions used in this series of tests.

The next set of attenuation data for the cambered rotor shows the total pressure and axial velocity amplitude ratios as a function of incidence angle for the two square-shaped inlet distortions tested. Figures 58 and 59 present the results for the 90 degree and 180 degree distortions, respectively. It can be seen that the incidence angle again does not significantly influence the attenuation of the axial velocity and total pressure distortions. In the case of the square distortions, it is observed that the effect of rotor-stator spacing on the distortion attenuation downstream of the rotor is no longer insignificant. Figure 58 shows approximately a 20 percent difference between the attenuation of the axial velocity distortion produced with a rotor-stator spacing of 2.0 chord lengths and that produced with a rotor-stator spacing of 0.5 chord length. A similar difference in the total pressure distortion downstream of the rotor is shown in Figure 59 for the 180 degree distortion. The reason for this effect of rotor-stator spacing is not known. The observation was made for the uncambered rotor that the total pressure distortion upstream of the rotor had been amplified more for the 90 degree

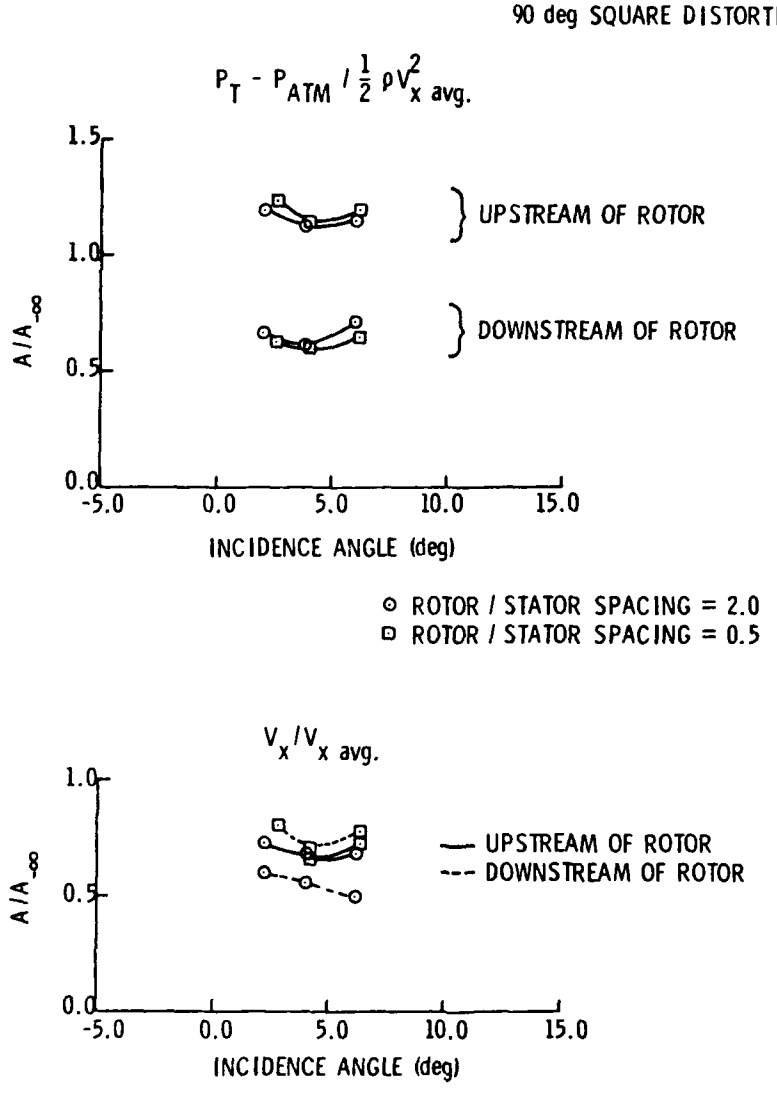

Figure 58. Measured Axial Velocity and Total Pressure Distortion Attenuation versus Incidence Angle for a 90 Degree Square Distortion with the Cambered Rotor

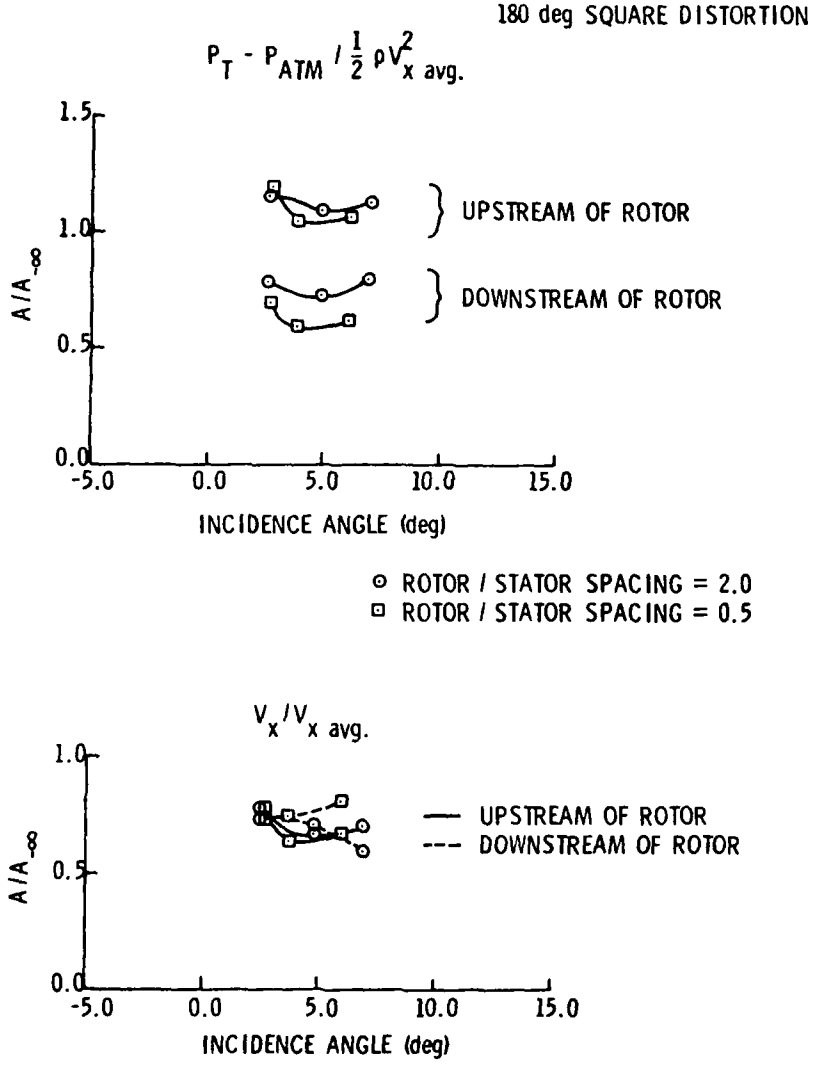

Figure 59. Measured Axial Velocity and Total Pressure Distortion Attenuation versus Incidence Angle for a 180 Degree Square Distortion with the Cambered Rotor

distortion than for the 180 degree distortion. This is also true for the case of the cambered rotor as can be seen in Figures 58 and 59

One final important characteristic of the data in Figures 58 and 59 concerns the amplitude ratios upstream and downstream of the rotor. The total pressure amplitude ratio for both the 90 degree and 180 degree distortions show that the distortion is amplified upstream of the rotor and then undergoes a considerable amount of attenuation downstream of the rotor. However, it is seen from the figures that the attenuation of the axial velocity distortion for a rotor-stator spacing of 0.5 chord length actually decreases as the distortion passes through the rotor. As discussed in Section 4.2.2, periodic fluctuations in the axial velocity distribution appeared downstream of the rotor due to a blockage effect when the stator row was in its forward position. The amplitude of the square distortions is defined as the difference between the maximum and minimum values of the distortion. Since the axial velocity distribution upstream of the rotor did not experience high peaks and low valleys due to a blockage effect, it is concluded that the amplitude of the axial velocity distortion is greater downstream than upstream of the rotor. This phenomenon was not observed with the sinusoidal distortions because the amplitudes were defined in terms of the fundamental harmonic of the Fourier series.

In a manner similar to the case of the uncambered rotor, the attenuation data for the cambered rotor was also plotted as a function of reduced frequency. Figures 60 and 61 present the amplitude ratio of the total pressure and axial velocity distortions versus ω for two constant values of incidence, $i = 0$ degrees and $i = 5$ degrees, respectively. The values of reduced frequency correspond to the one-, two-, four-, and six-cycle

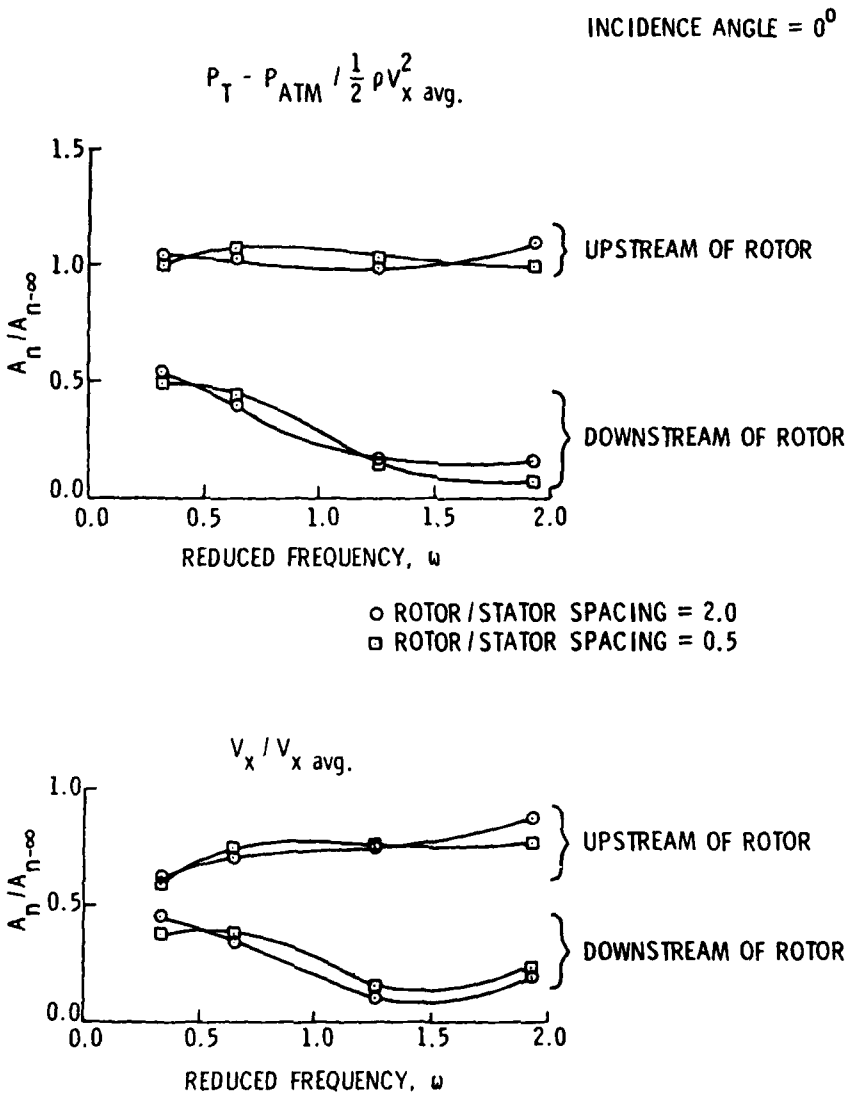

Figure 60. Amplitude Ratio versus Reduced Frequency for a Constant Mean Incidence Angle of Zero Degrees with the Cambered Rotor

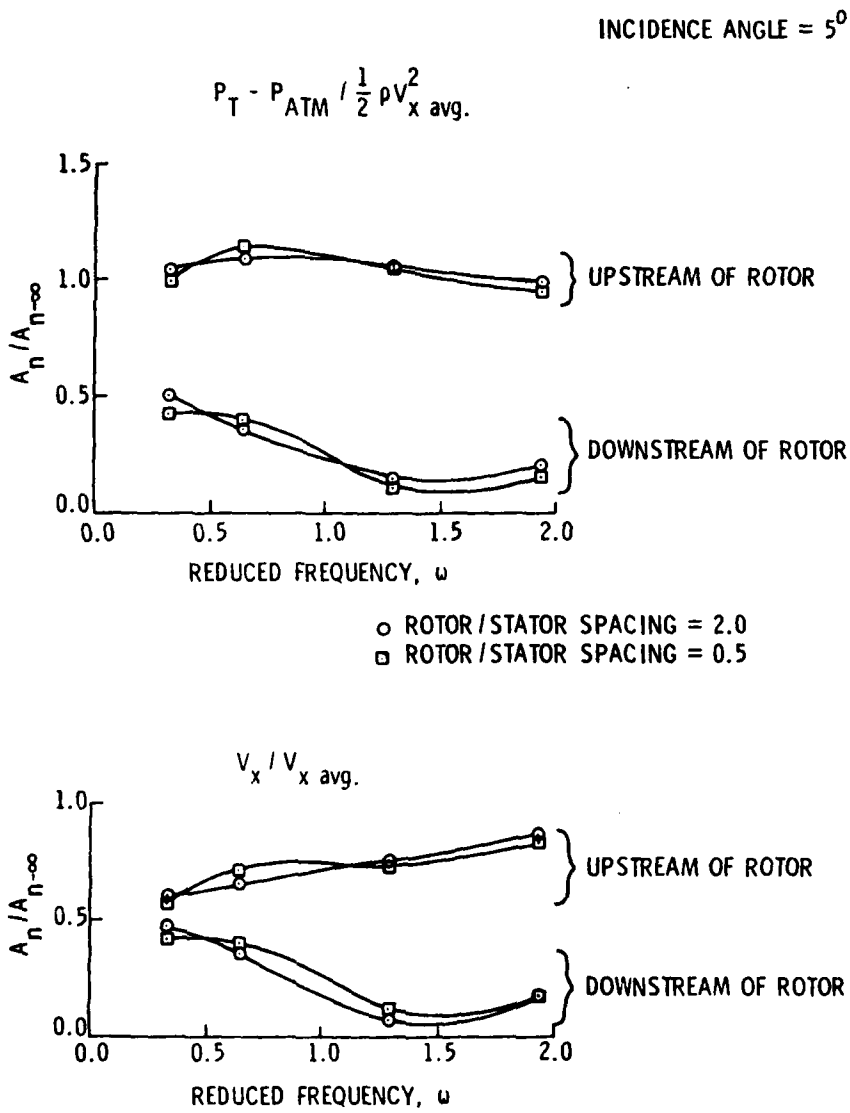

Figure 61. Amplitude Ratio versus Reduced Frequency for a Constant Mean Incidence Angle of Five Degrees with the Cambered Rotor

sinusoidal distortions. By comparing the magnitudes of the amplitude ratios in the two figures, it is easily seen again that incidence angle has little effect on the distortion attenuation. Also, the effect of rotor-stator spacing is again found to be insignificant. Downstream of the rotor, the attenuation of the total pressure and axial velocity distortions is increased with increasing values of reduced frequency.

The final set of attenuation data for the cambered rotor presents the response of the rotor on the distortion where the measurements were made at radial locations other than the mean radius of the blade. Two radial or spanwise locations were less than the mean radius and two were greater than the mean radius. Figures 62 and 63 present the amplitude ratio of the total pressure and axial velocity distortions as a function of the radial distance of the five-hole probe from the surface of the hub for the sinusoidal and square distortions, respectively. Figure 64 shows the attenuation data versus reduced frequency for a constant mean incidence angle of five degrees. The four curves on the graph represent the four radial measurement locations that were tested. Figure 64 shows the expected result of increased attenuation downstream of the rotor with increasing reduced frequency. The main observation to be made from all three figures is that the effect of different radial or spanwise measurement locations on the attenuation of the total pressure and axial velocity distortions is small. In general, the attenuation of the total pressure and axial velocity distortions downstream of the rotor for both the sinusoidal and square-shaped distortions increases closer to the hub. It appears, however, that the increase is only approximately ten to fifteen percent between the two extreme radial locations. It was pointed out in Section 4.2.2 that the total pressure flow field was only slightly changed

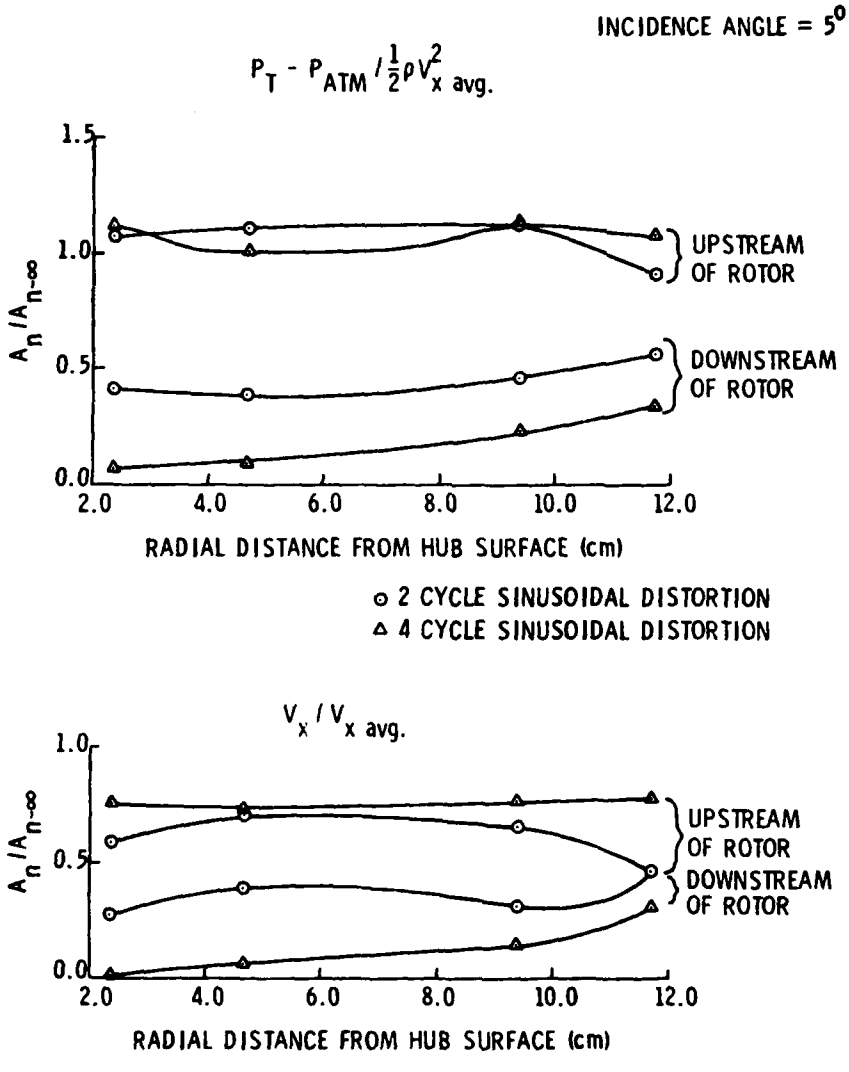

Figure 62. Amplitude Ratio versus Radial Location for a Constant Mean Incidence Angle of Five Degrees with the Cambered Rotor

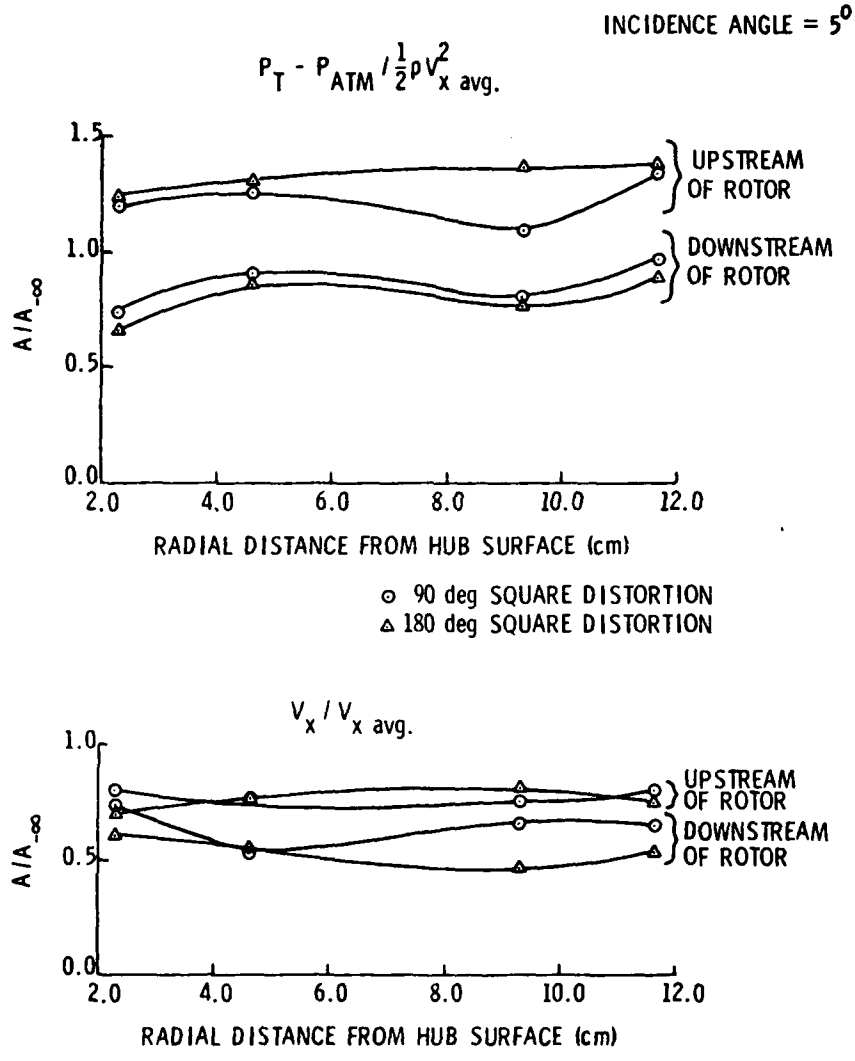

Figure 63. Amplitude Ratio versus Radial Location for a Constant Mean Incidence Angle of Five Degrees with the Cambered Rotor

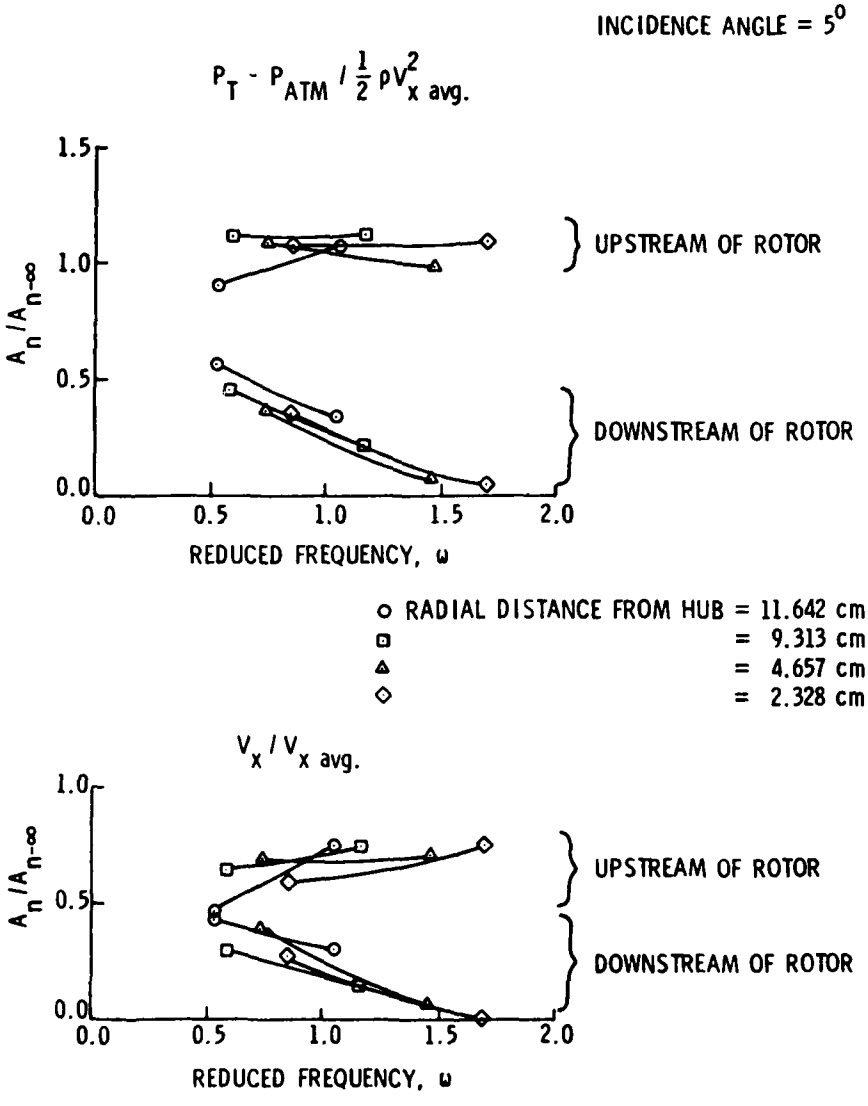

Figure 64. Amplitude Ratio versus Reduced Frequency for a Five Degree Incidence Angle at the Four Radial Locations with the Cambered Rotor

and the axial velocity flow field experienced a larger change in magnitude at different radial locations along the blade. These observations appear to be supported by the attenuation data shown in Figures 62, 63, and 64.

4.4 Unsteady Total Pressure Losses

The operation of a rotating blade row in either a uniform or a distorted flow results in losses in total pressure. As a consequence of these losses, the total pressure rise predicted by ideal fluid theories is not realized. In an actual turbomachine, these losses are the result of skin friction and pressure drag on the blades, viscous drag on the casing walls, and secondary flows due to three-dimensional effects. While the contribution of each of these losses is well documented for a rotor in a steady, uniform flow, there is little, if any, data available regarding the losses in a distorted inflow.

In Section 4.1, the total pressure loss coefficient for steady flow was defined by Equation (34). The same definition is used to represent the unsteady losses in this section, except that the circumferential averaged values of P_T and V_θ are used. Thus, the unsteady actual and ideal and total pressure rise and the total pressure loss coefficients are defined by the following equations:

$$\tilde{\Psi} = \frac{\overline{P}_{T\ exit} - \overline{P}_{T\ inlet}}{1/2\rho U^2}, \tag{41}$$

$$\tilde{\Psi} = \frac{2\ (\overline{V}_{\theta\ exit} - \overline{V}_{\theta\ inlet})}{U}, \tag{42}$$

and

$$\tilde{C}_{P_{T\ loss}} = \tilde{\Psi}_{ideal} - \tilde{\Psi} \tag{43}$$

where the bar over P_T and V_θ indicates circumferential-mean values. A ratio of the unsteady loss coefficient to the steady loss coefficient at the same mean incidence angle can then be formed.

The studies which have been conducted in this area have been concerned with the effects of upstream unsteadiness in turbine cascades [40, 41]. These studies were conducted with a stationary turbine cascade and a set of rotating cylinders located upstream of the cascade. As a result, the cascade experienced a time varying inflow. The conclusions from these studies are that the presence of an unsteady flow increases the total pressure loss as compared with that experienced in a uniform flow. In both investigations, the loss associated with the unsteadiness increased with the speed of rotation of the cylinders, i.e., reduced frequency and, in some cases, were twice the magnitude of the steady loss.

A portion of the data obtained in this study can be analyzed to determine the total pressure losses associated with a distorted inflow. Since most of the flow surveys were conducted at the mean blade radius, the losses experienced are primarily those due to skin friction and pressure drag on the blades. The losses due to the viscous drag on the casing walls are not present and the effects of secondary losses are minimal for the studies conducted at the mean radius [42]. Considering only the influence of skin friction and pressure drag to contribute to these losses, it is concluded on a quasi-steady basis that the loss in the distorted inflow will be greater than that experienced in a uniform flow since the blades are locally experiencing higher angles of incidence. This follows from data of cascades in a uniform or steady flow showning an increase in cascade loss with increasing angle of incidence.

Furthermore, one would suspect the presence of an unsteady loss which is a function of the type of distortion in which the blade row is operated, i.e., reduced frequency.

In a manner similar to that described in Section 4.1 for uniform flow, the ideal and actual circumferential-mean total pressure rise coefficients can be obtained for the blade row operated in a distorted inflow. The ideal circumferential-mean total pressure rise for a sinusoidal distorted inflow is identical to that in a uniform flow if the pressure rise characteristic is linear. Higher blade stagger angles result in a larger component of circumferential velocity downstream of the blade row since the amount of swirl or turning of the flow is increased as ξ is increased. However, to maintain equal values of incidence or blade loading at different stagger angles, the blade speed, U, must also change (for a constant axial velocity). Therefore, within experimental accuracy, the ideal total pressure rise in uniform flow does not change for the various blade stagger angles. Figure 65 presents some typical data for the six-bladed uncambered rotor operated in a four- and six-cycle sinusoidal distortion flow field. From Equation (34), the difference between the actual and ideal circumferential-mean total pressure rise coefficient represents the total pressure loss associated with operation in the distorted inlet flow.

The ratio of the unsteady total pressure loss coefficient to the steady total pressure loss coefficient calculated from the data for the sinusoidal distortions is presented as a function of reduced frequency for the uncambered and cambered test rotors in Figures 66 and 67, respectively. The reduced frequency was previously defined in equation (40); in a uniform flow, the distortion wavelength is infinite and hence $\omega = 0$.

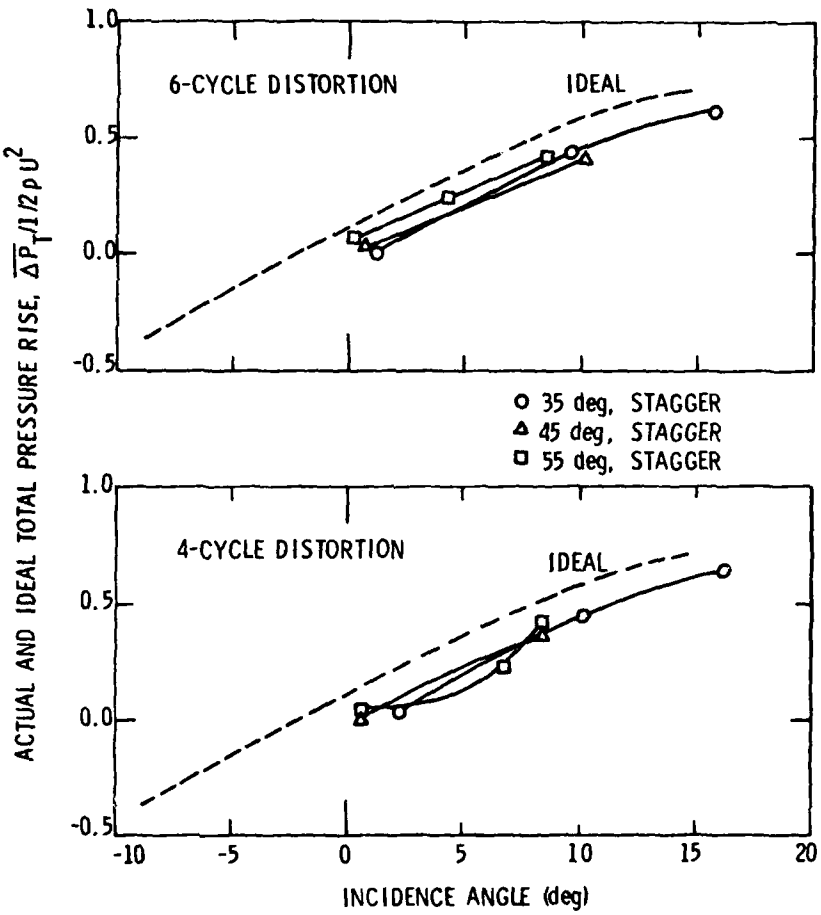

Figure 65. Six Bladed Cambered Rotor Performance in a Distorted Flow

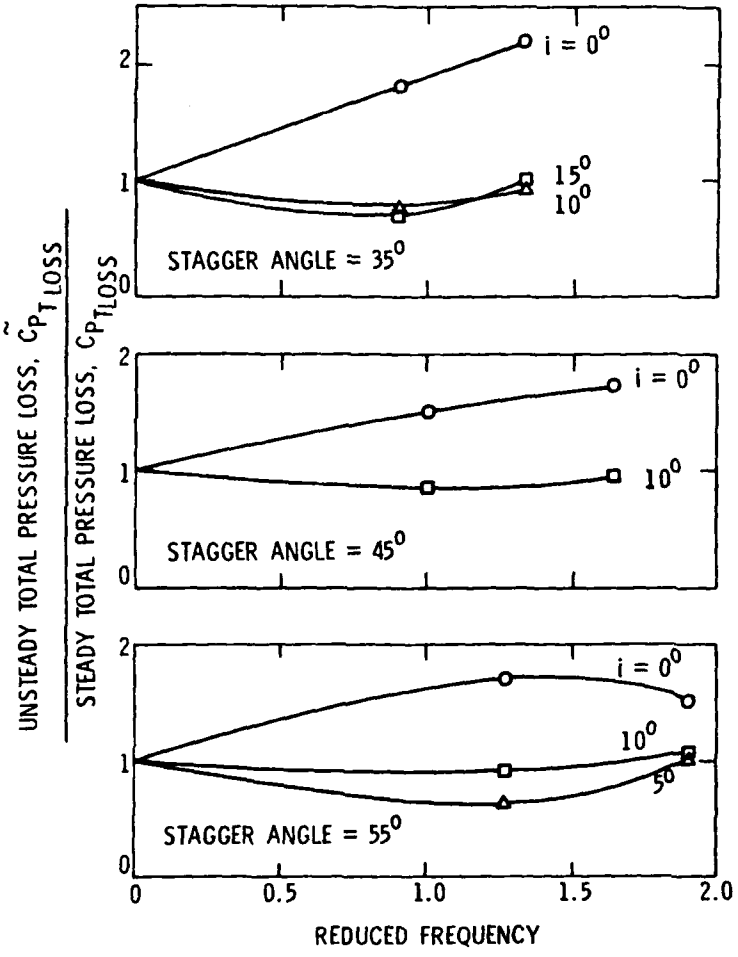

Figure 66. Ratio of Unsteady Loss to Steady Loss versus Reduced Frequency for the Six Bladed Uncambered Rotor

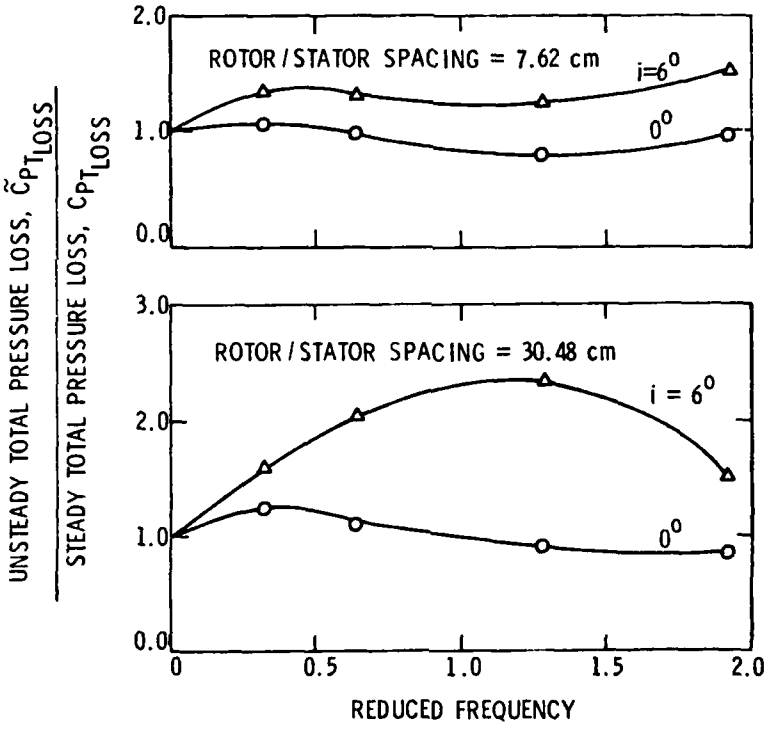

Figure 67. Ratio of Unsteady Loss to Steady Loss versus Reduced Frequency for the Nine Bladed Cambered Rotor

The studies of Yocum [37] and Kirillov et al. [40] reveal that the unsteady losses are highly dependent on reduced frequency. Their data show that the unsteady losses reach a maximum at low values of reduced frequency and, in some cases, the peak values of unsteady losses are greater than three times the losses in steady flow. No such peak is observed in the data of this study as shown in Figures 66 and 67. For the case of the uncambered rotor in Figure 66, no experimental data was obtained to determine whether the unsteady losses reach a maximum at low values of reduced frequency. It is necessary to perform experiments at low reduced frequencies, i.e., in a distortion flow field with one- and two-cycle sinusoidal variations of total pressure, in order to verify the conclusions reached in References [37] and [40].

Based on the data available, an attempt was made to correlate the total pressure loss data obtained in this study for the six-bladed uncambered rotor and the data obtained in Reference [37] for the twelve-bladed uncambered rotor. This was done to try to prove the existence of peak unsteady losses at low distortion frequencies. To do this, the ratio of unsteady loss to steady loss was plotted as a function of the ratio of rotor blade spacing to distortion wavelength (the reason for using this ratio will be discussed in Chapter V), and the results are shown in Figure 68.

Part of the change of unsteady losses with respect to frequency observed by Kirillov [40] was due to a change in the flow nonuniformity as the frequency changed. Additional experimental and analytical investigations are required to identify the causes of the unsteady losses and to explain the dependency on frequency.

Figure 69 presents the ratio of unsteady to steady total pressure loss as a function of reduced frequency for the four different radial

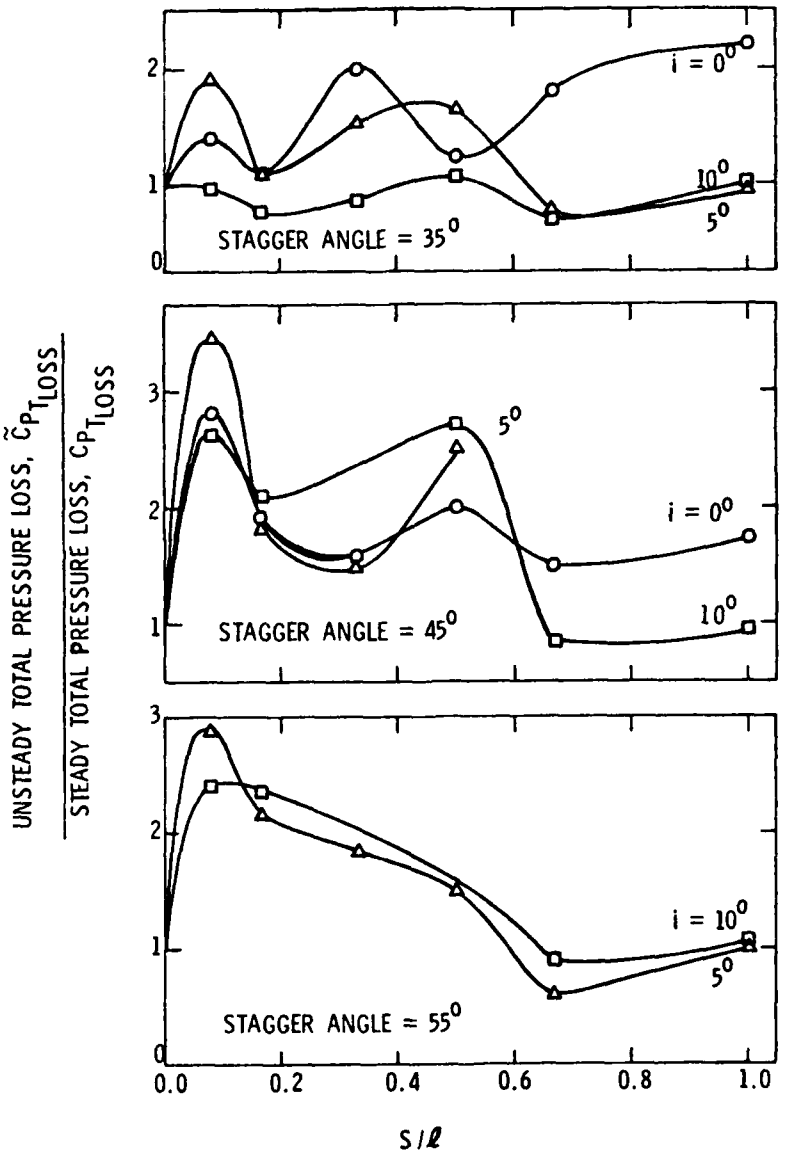

Figure 68. Ratio of Unsteady Loss to Steady Loss versus Ratio of Blade Spacing to Distortion Wavelength for the Uncambered Rotor

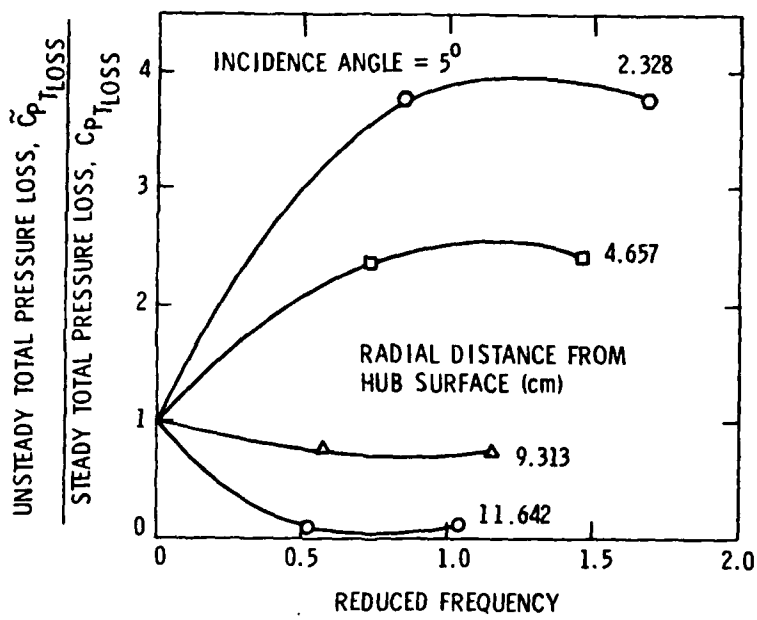

Figure 69. Ratio of Unsteady Loss to Steady Loss versus Reduced Frequency at the Four Radial Locations for the Cambered Rotor

locations at which the circumferential flow surveys were taken using the nine-bladed cambered rotor. It can be seen that the unsteady losses are much greater near the hub of the blade than near the tip. In fact, the data show that the loss ratio is close to zero near the tip for the values of reduced frequency that were tested. It is possible that local flow separation near the tip could cause large values of steady total pressure loss.

From an unsteady viewpoint, additional losses in total pressure may be caused by the vortex shedding associated with the unsteady circulation on the blades. The unsteady pressure distribution on the blades will also affect the growth and stability of the boundary layer, and the effect of the unsteadiness on the boundary layer is expected to be dependent on the reduced frequency. The data in Figure 69 indicate that the losses due to the boundary layer at the hub surface are much higher than the losses due to the annulus wall boundary layer. Also, the losses due to secondary flows near the hub seem to be important and may account for the increase in the loss curves. Furthermore, it is suspected that a radial shift in streamlines could seriously affect the unsteady losses. More detailed and extensive radial and circumferential flow surveys are required in a flow where a radial shift in the streamline occurs, and the data should then be energy or mass averaged. Although some data at different radial locations have been presented here, future studies with regard to a proper averaging technique should be conducted to identify the causes of the unsteady losses. The contributions to the unsteady losses from various sources such as hub and annulus wall boundary layer, secondary flows, vortex shedding, and viscous drag should also be examined in more detail.

Radial surveys in a uniform flow could also be conducted to determine the effects of the hub and annulus wall boundary layers on the steady total pressure losses.

CHAPTER V

COMPARISON OF EXPERIMENTAL AND THEORETICAL RESULTS

In this section, the results of the theoretical analysis discussed in Chapter II are presented and compared with experimental results obtained in the AFRF. The results for the six-bladed and twelve-bladed uncambered rotors and the nine-bladed cambered rotor with space-to-chord ratios of 1.353, 0.676, and 0.90, respectively, are presented. The data for the twelve-bladed rotor was provided by Yocum [37]. These data are then compared with the predicted results of the time-mean total pressure downstream of the rotor obtained by the use of Equation (19).

In addition to the reduced frequency, the unsteady response of a cascade or blade row is also dependent upon a pitchwise frequency parameter, the intrablade frequency (or intrablade phase angle) which is defined as

$$\tau = - \frac{2\pi S}{\ell} , \tag{44}$$

where S is the rotor blade spacing and ℓ is the wavelength of the distortion in the pitchwise direction. This frequency parameter relates the unsteady response of the neighboring blades of the blade row or cascade to that of the reference blade at a given instant in time. For a rigid, non-vibrating cascade of blades, the intrablade frequency is related to the reduced frequency, ω, as follows:

$$\tau = - 2\omega \frac{S}{C} \csc\xi . \tag{45}$$

The experimental and theoretical results presented in this chapter are plotted as the ratio of the distortion amplitude with the rotor

operating to the distortion amplitude at the rotor inlet without the rotor operating as a function of the ratio of blade spacing to distortion circumferential wavelength. The blade spacing and distortion circumferential wavelength are defined, respectively, as:

$$S = \frac{2\pi r}{B} \tag{46}$$

and

$$\ell = \frac{2\pi r}{N} \ . \tag{47}$$

where r is the radius at which the measurements were taken (in most cases, the mean radius), B is the number of rotor blades, and N is the number of distortion cycles. Combining Equations (46) and (47), the ratio of blade spacing to distortion wavelength can be written as:

$$\frac{S}{\ell} = \frac{2\pi r/B}{2\pi r/N} = \frac{N}{B} \ . \tag{48}$$

Figures 70 and 71 present the experimental values of the distortion amplitude ratio versus the ratio s/ℓ. Both the axial velocity and total pressure distortions upstream and downstream of the rotor are plotted in the same figure. Figure 70 shows the experimental data for the six-bladed and twelve-bladed rotors for blade stagger angles of 35 and 45 degrees. Figure 71 shows the experimental data for the six-bladed and twelve-bladed rotors for stagger angles of 55 degrees and also the data for the nine-bladed rotor with a stagger angle of 50 degrees. It was determined in Section 4.3.1 that stagger angle is an important parameter which influences the attenuation of a distortion. Therefore, the data on Figures 70 and 71 are grouped together according to nearly equivalent stagger angles.

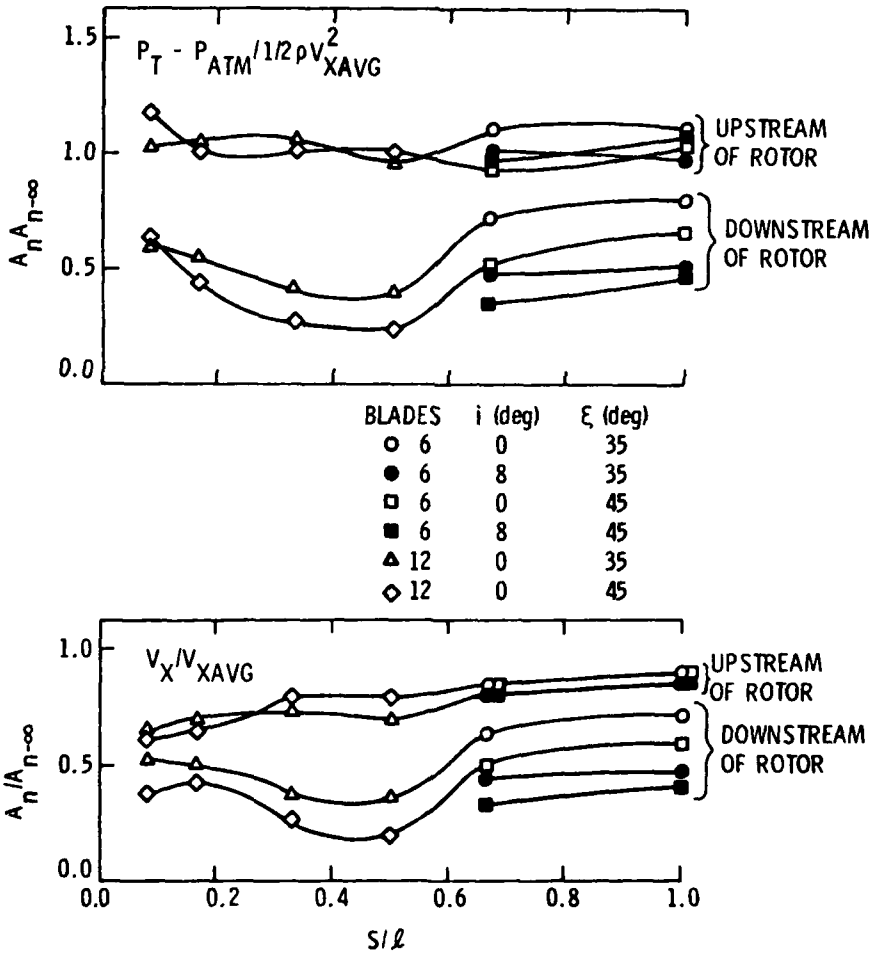

Figure 70. Measured Values of Amplitude Ratio versus Ratio of Blade Spacing to Distortion Wavelength for Stagger Angles of 35 and 45 Degrees

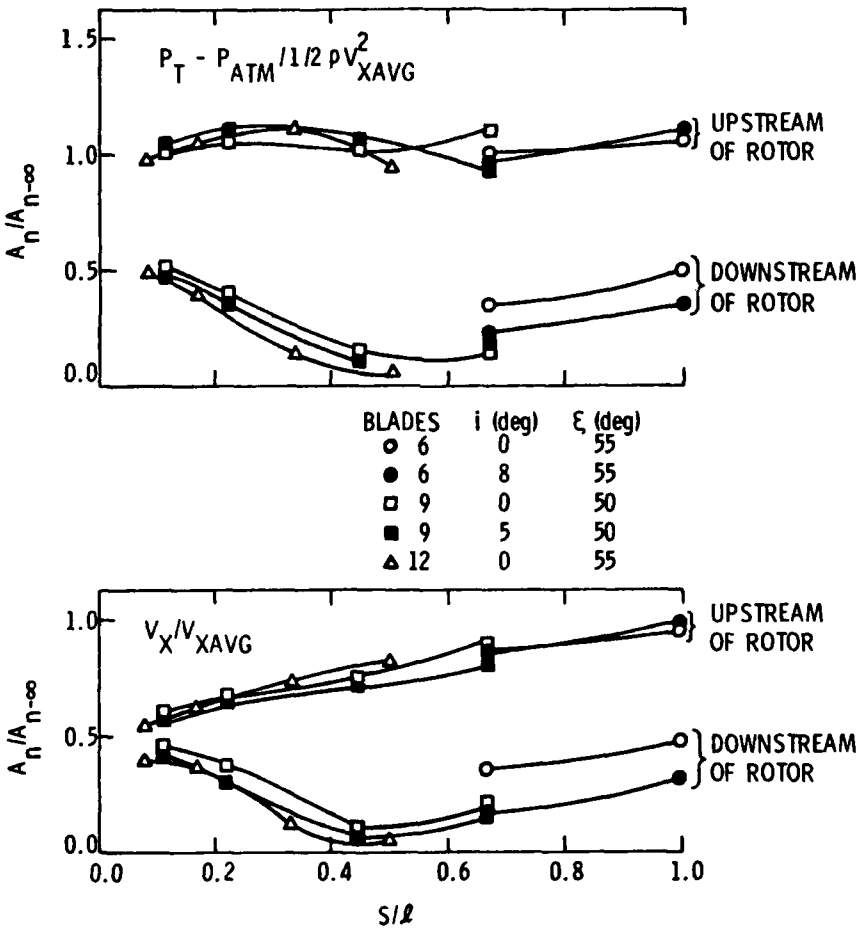

Figure 71. Measured Values of Amplitude Ratio versus Ratio of Blade Spacing to Distortion Wavelength for Stagger Angles of 50 and 55 Degrees

The most important observation to be made in Figures 70 and 71 is the effect on the distortion amplitude which produces a maximum attenuation when the blade spacing is equal to one-half the wavelength of the distortion. This maximum attenuation downstream of the rotor corresponds to a value of intrablade phase angle equal to $-\pi$ and different values of ω dependent upon the value of S/C and ξ. As seen from the figures, the attenuation then decreases as S/ℓ approaches one, i.e., as the intrablade phase angle approaches -2π. It should be noted here that the negative signs on π and 2π come from the definition of τ in Equation (44) which is is the result of the coordinate system which is chosen for the cascade [21]. In the present system, the cascade is moving to the right, and the adjacent blades to the right of the reference blade are designated as positive. Thus, the blades to the left of the reference blade, which are designated as negative, see the same disturbance as the reference blade at time t>o. Therefore, a negative sign occurs simply because of the way in which the blades in the cascade (or blade row) were counted.

The conclusion that the ratio of blade spacing to distortion wavelength is a primary factor in the attenuation of the inlet distortion and that a value of $S/\ell = 0.5$ (i.e., $\tau = -\pi$) produces a maximum attenuation is very significant. This is a condition when the unsteady response of adjacent blades in the blade row are 180 degrees out of phase; at a given instant of time, if a blade experiences a maximum distortion velocity in a sinusoidal distortion, the adjacent blades are experiencing a minimum distortion velocity. Correspondingly, at $S/\ell = 1.0$ ($\tau = -2\pi$), all of the blades experience a similar portion of the sinusoidal distortion at a given instant of time and the amount of attenuation is minimized. Thus,

the unsteady cascade effect on the distortion is very significant and, if the blade spacing and distortion wavelength are properly matched to give $S/\ell = 0.5$, a maximum attenuation of the distortion amplitude will occur.

The data for all three rotors shown in Figure 71 appear to collapse onto the same curve downstream of the rotor. It is also seen that the effect of stagger angle is consistent between the six- and twelve-bladed rotors. Downstream of the rotor, however, the data for the six-bladed rotor at zero degree incidence does not collapse on the curve; these data show a significant decrease in the level of attenuation. The most probable cause for this is an effect due to the space-to-chord ratio. For a higher space-to-chord ratio, there is less variation in flow angle between the blades. This could result in less turbulent mixing and, therefore, less attenuation downstream of the rotor. However, to verify this effect requires data showing the distortion amplitude ratio as a function of S/C for constant values of S/ℓ. At present, such data do not exist, although the two points at $S/\ell = 0.666$ in Figure 71 exhibit the anticipated trend.

Figures 72 and 73 show the results of the total pressure amplitude downstream of the rotor predicted by the theoretical analysis described in Chapter II. Also shown in these figures are the experimental data measured downstream of the rotor. An important feature of these two graphs is that the amount of attenuation measured experimentally is found to be much greater than the attenuation predicted by theory. In fact, the theory predicts an amplification of the distortion. This is due to the magnitude of the unsteady blade circulation which increases the distortion amplitude above the amplitude experienced in the absence of the rotor. The magnitude of unsteady blade circulation plays a very

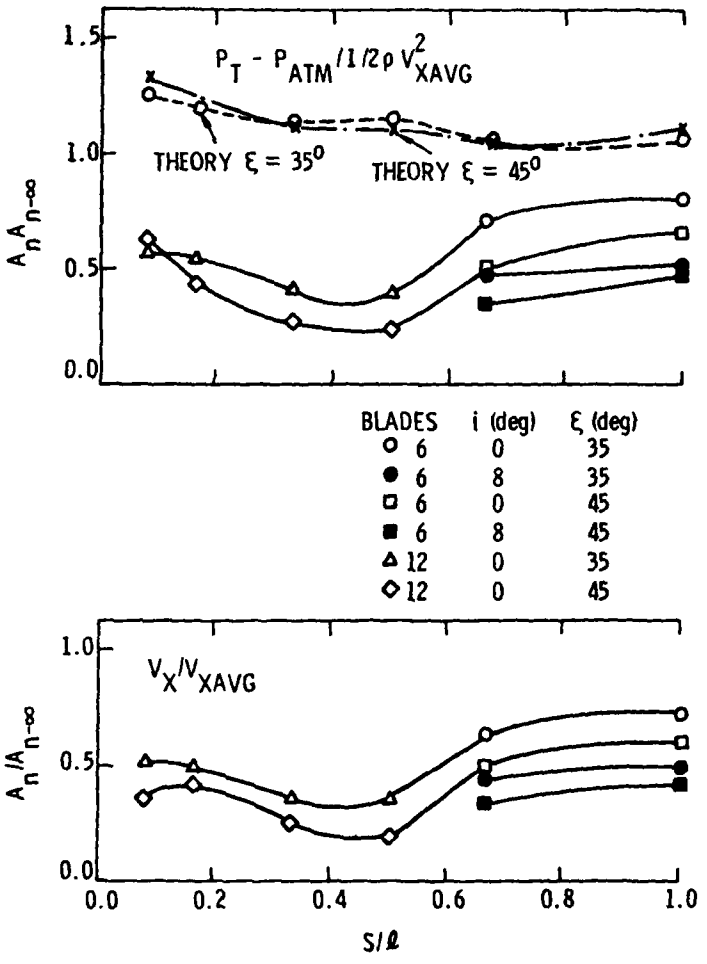

Figure 72. Amplitude Ratio versus Ratio of Blade Spacing to Distortion Wavelength Downstream of Rotor Showing the Predicted Values of Total Pressure for Stagger Angles of 35 and 45 Degrees

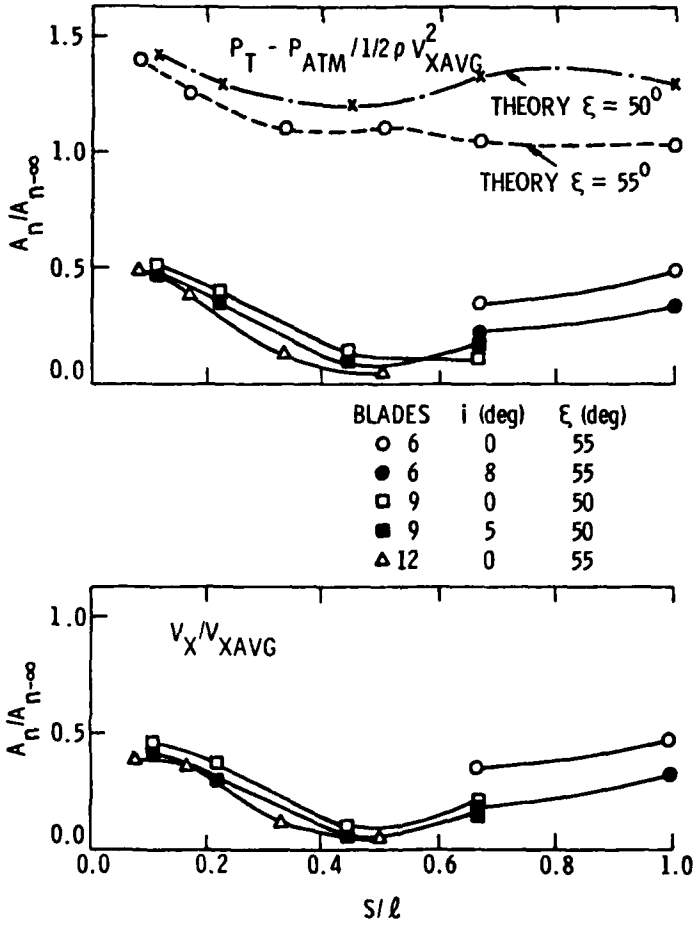

Figure 73. Amplitude Ratio versus Ratio of Blade Spacing to Distortion Wavelength Downstream of Rotor Showing the Predicted Values of Total Pressure for Stagger Angles of 50 and 55 Degrees

significant role in determining the amplitude of the distortion in the theoretical analysis. As the magnitude of unsteady blade circulation increases, the amplitude ratio of the total pressure distortion also increases since the theory does not account for any viscous losses. An increase in the amplitude ratio is equivalent to a decrease in the attenuation of the distortion. The large difference between the amount of attenuation predicted by theory and that measured experimentally is attributed to blade thickness, boundary layer, and turbulence mixing effects which are assumed negligible in the theory. There is also the possibility of unsteady radial flows which result from a radial gradient of unsteady circulation and are not included in the two-dimensional theoretical analysis.

It was stated previously that the experimental results show a maximum attenuation at $S/\ell = 0.5$ and then a decrease in attenuation as the ratio of spacing to wavelength approaches one. From Figures 72 and 73, it is seen that the predicted results also demonstrate an increasing attenuation as a value of $S/\ell = 0.5$ is approached. However, as S/ℓ is increased above 0.5 for the six- and twelve-bladed rotors, the predicted attenuation also shows a slight increase. The data obtained in this study for the nine-bladed cambered rotor employed the one-, two-, four-, and six-cycle sinusoidal distortion screens. These distortions correspond to values of S/ℓ equal to 0.111, 0.222, 0.444, and 0.667, respectively. For these points, as seen on Figure 73, the trend of the predicted results agree quite well with the trend of the measured values. In an attempt to verify the increase in the experimental attenuation which is observed for the cambered rotor as S/ℓ approaches one, a set of AFRF data was obtained for the nine-bladed rotor in a nine-cycle sinusoidal

distortion flow field. This yields a ratio of blade spacing to distortion wavelength of one. From this set of data, as shown in Figure 73, it was again found that the predicted attenuation increased as S/ℓ goes to one. It should be noted that the points shown on the theoretical curves in Figures 72 and 73 are the points at which the theory was applied and are based on experimental measurements of the distortion at the rotor inlet. The shape of the curves between these discrete points is not defined. Additional data utilizing more distortion screens would be required to determine the complete shape of the predicted curve.

One final observation to be made from the figures just discussed is the effect of incidence angle on the attenuation. It is seen that the measured attenuation is increased at higher values of incidence angle, and the effect is most prominent with the six-bladed rotor. This result was observed previously and discussed in Section 4.3.

When dealing with inlet distortions, two parameters are used to describe the unsteadiness of the flow; these two parameters are the amplitude and the phase angle. The amplitude has been discussed in the preceding paragraphs. The phase angle merely shows how the flow is displaced circumferentially due to both the steady and unsteady effects of the rotor. In Figures 74 and 75, the phase angle upstream of the rotor is plotted as a function of the ratio of blade spacing to distortion wavelength. The phase angle of both the axial velocity and total pressure distortions are presented. The data in Figure 74 represent the six- and twelve-bladed rotors having stagger angles of 35 and 45 degrees. Figure 75 presents the data for the six- and twelve-bladed rotors with a stagger angle of 55 degrees and for the nine-bladed cambered rotor with a stagger angle of 50 degrees. Since these figures show the phase angle at the

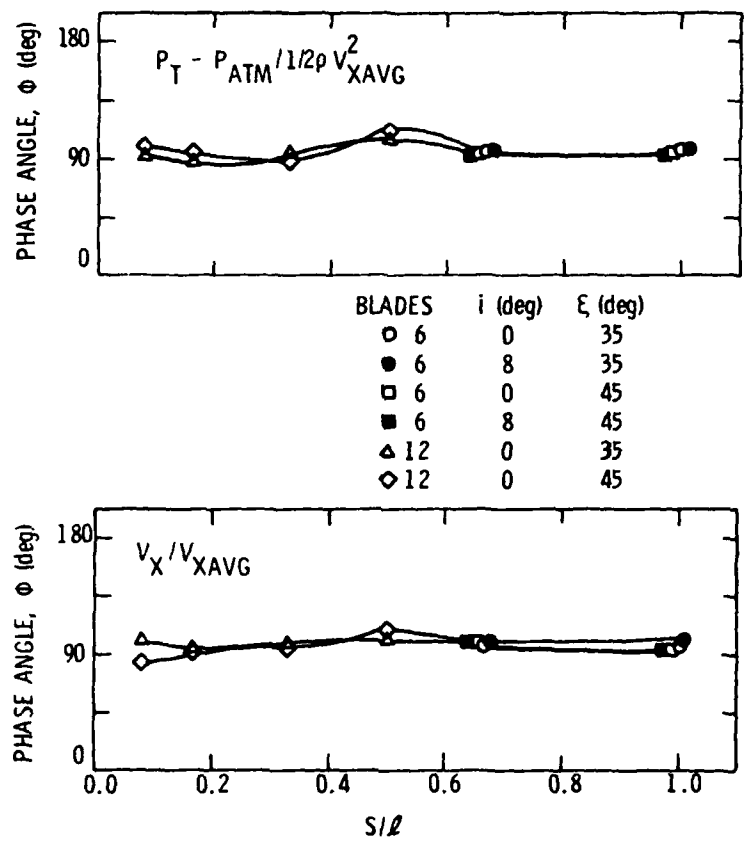

Figure 74. Phase Angle versus Ratio of Blade Spacing to Distortion Wavelength Upstream of Rotor for Stagger Angles of 35 and 45 Degrees

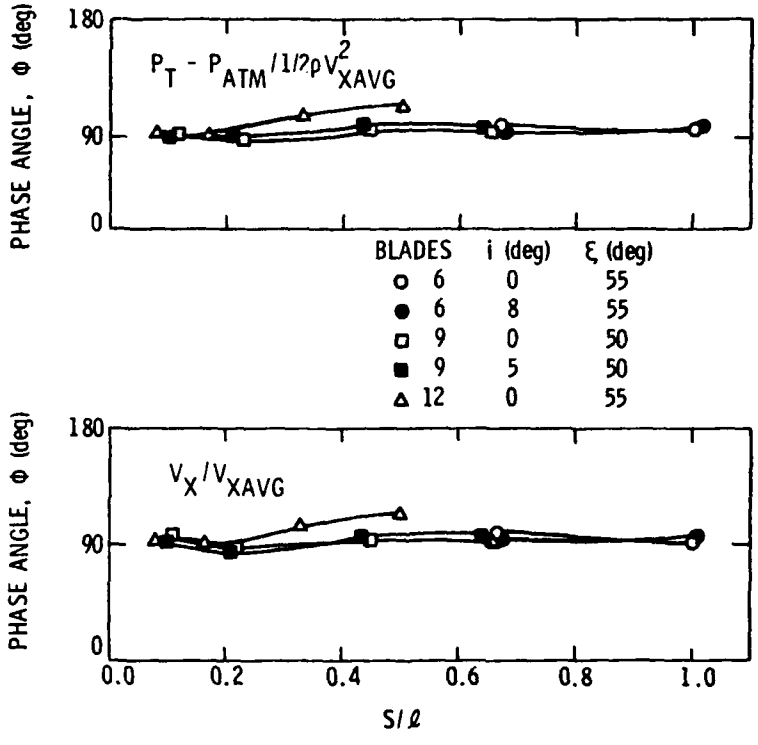

Figure 75. Phase Angle versus Ratio of Blade Spacing to Distortion Wavelength Upstream of Rotor for Stagger Angles of 50 and 55 Degrees

inlet before its passage through the rotor, all the data, as expected, show a constant phase angle of approximately 95 degrees. This represents the phase angle of the distortion only, and it is not influenced by the action of the rotor. The one-, two-, four-, and six-cycle distortion screens were all placed in the inlet of the AFRF such that a minimum value of velocity occurred at a circumferential location of zero degrees. Since the screens were all placed in the AFRF in the same way, the phase angles of the fundamental harmonics at the inlet to the rotor were all approximately the same and equal to approximately 90 degrees.

As the distortion is transported through the rotor, several factors contribute to the change of phase angle. Among these are the steady lift on the rotor blades, the magnitude and phase angle of the unsteady circulation referenced to the trailing edge of the blade, and the convection of the distortion downstream of the rotor. These factors were all included in the theoretical analysis to give a predicted value of the phase angle of the total pressure distortion downstream of the rotor. These predicted phase angles are plotted and compared to the phase angles measured experimentally downstream of the rotor in the AFRF in Figures 76 and 77. Once again, the large discrepancy between the measured and the predicted values may be due to the effects of blade thickness and viscosity (i.e., boundary layer) which are neglected in the theory. The presence of a boundary layer on the blade acts to delay the response of the blade to the disturbance flow. The existence of an unsteady radial or spanwise flow may also contribute to the large difference between the theoretical and experimental results. An increase in the phase angle is noticed in the experimental data at the higher incidence angles, and it is most noticeable at larger values of S/ℓ. Higher mean incidence angles result

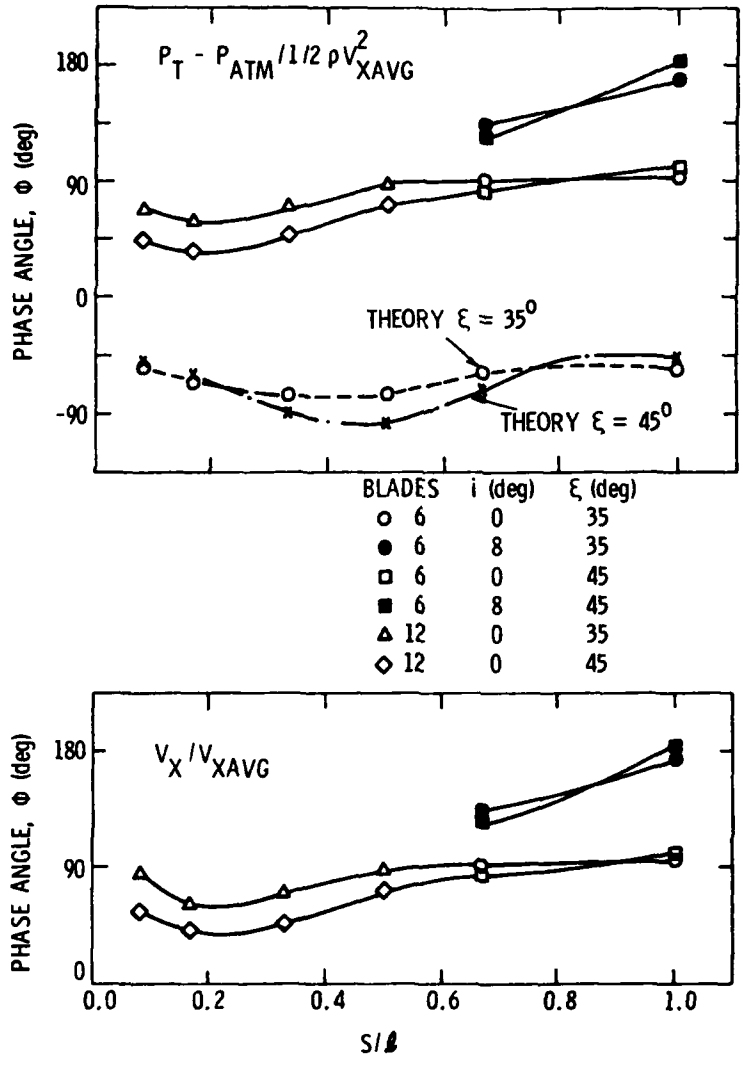

Figure 76. Phase Angle versus Ratio of Blade Spacing to Distortion Wavelength Downstream of Rotor Showing the Predicted Values of Total Pressure for Stagger Angles of 35 and 45 Degrees

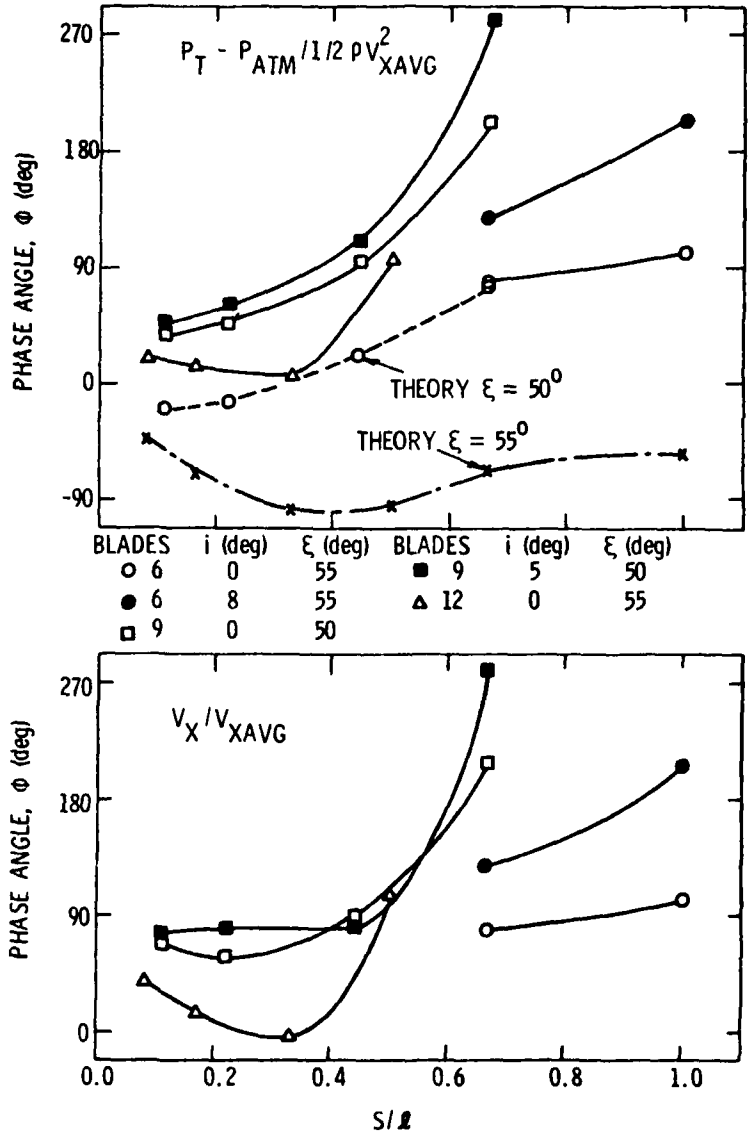

Figure 77. Phase Angle versus Ratio of Blade Spacing to Distortion Wavelength Downstream of Rotor Showing the Predicted Values of Total Pressure for Stagger Angles of 50 and 55 Degrees

in greater steady lift on the rotor blades (up to a point), thus increasing the amount of phase shift in the circumferential direction. This effect would also be reflected in the theoretical values of phase angle; however, the theory was only applied to cases with an incidence angle of zero degrees.

The conclusions reached in this chapter are very important, and they provide a successful tool for the designer which can be applied to the unsteady design of an axial flow fan or compressor. The data of this study show that, if the type of inlet distortion is known, the maximum amount of attenuation of the distortion can be achieved by designing a blade row with a blade spacing of one-half the distortion wavelength. Both experimental and analytical efforts, however, have only reached this conclusion for sinusoidal inlet distortions. This conclusion was not observed for the 90 and 180 degree square distortions since the values of reduced frequency were too low for the square distortions.

CHAPTER VI

SUMMARY, CONCLUSIONS, AND RECOMMENDATIONS FOR FUTURE RESEARCH

6.1 Summary and Conclusions

A parametric study of the effects of blade stagger angle, mean blade loading, rotor-stator spacing, blade spanwise location, and distortion characteristics on the flow fields upstream and downstream of two test rotors has been conducted. The investigation involved the collection of a large amount of experimental data to describe the effects of the various parameters just listed. These data can, hopefully, be used in future studies to obtain a better understanding of distortion phenomena and to improve current prediction techniques. It is also hoped that data such as the type provided in this study will aid turbomachinery designers in the design of axial flow fans and compressors with improved performance. A complete set of the data obtained in this investigation can be found in Reference [39]. The study has also revealed some important parameters affecting distortion attenuation and unsteady losses, which should provide guidance for conducting future experimental and analytical research in this area.

On the basis of the results obtained from the experimental and analytical research conducted in this investigation, the following conclusions can be made:

1. The incidence angle or mean blade loading was found to have very little effect on the distortion attenuation for the nine-bladed cambered rotor. This is probably due partially to the linearity of the steady performance characteristics of the rotor. For the tests made with

the six-bladed uncambered rotor, the effect of incidence angle was more significant. The attenuation of the distortion downstream of the rotor was found to increase as the incidence angle increased. This dependence on blade loading is due to the non-linear behavior of the performance curve at high angles of incidence and also to greater turbulent mixing.

2. The effect of rotor-stator spacing was found to be negligible. Although a blockage effect was seen to cause a drastic change in the velocity and static pressure profiles with the stator row located in the forward position, the amplitudes of the axial velocity and total pressure distortions were essentially unchanged for the rotor-stator spacings of 2.0 and 0.5 blade chord lengths that were tested. This is because only the fundamental harmonic of the distortion was considered in the calculation of the distortion amplitude.

3. Although a decrease in the distortion attenuation was observed downstream of the rotor as the radial measurement distance from the hub was increased, this effect was small. A difference of only approximately ten to fifteen percent was found between the attenuation measured closest to the hub and that measured closest to the outer casing. The most noticeable effect of the different spanwise locations occurred in the unsteady total pressure losses; the losses were significantly

increased as the measurement locations approached the surface of the inner hub. This increase in losses near the hub could be due to the growth of the hub wall boundary layer and also secondary losses occurring near the hub.

4. Increasing the reduced frequency was found to result in an increased attenuation of the sinusoidal distortions that were tested using the nine-bladed rotor as S/ℓ approached 0.5. The one case of $S/\ell > 0.5$ showed the attenuation to decrease from the maximum value. Increasing the blade stagger angle for a fixed value of reduced frequency with the six-bladed rotor also resulted in an increase in the distortion attenuation. It should be noted that the stagger angle is contained in the definition of reduced frequency, and an increase in ξ will increase ω. Stagger angle also changes the disturbance velocities that are parallel and perpendicular to the axial direction (i.e., the chordwise and transverse gusts). The stagger angle, therefore, appears to be a very important parameter influencing the attenuation of a distortion.

5. The result obtained in References [37] and [40] that the unsteady losses reached a maximum at low values of reduced frequency is not observed in this investigation. In most cases, the operation of a rotor in a distorted flow field was found to result in total pressure losses greater than those measured with the rotor operating

in a uniform flow. However, no peak values of unsteady losses occurred at low values of ω for the cambered rotor. For the uncambered rotor, such a peak may exist, but experimental measurements at low values of reduced frequency are needed to confirm this suspicion.

6. An important conclusion drawn from the data with six- and nine-bladed rotors employed in this study and with the twelve-bladed rotor used in Reference [37] is that the inlet distortion is most greatly attenuated at a value of rotor blade spacing equal to one-half the distortion wavelength. As the ratio of blade spacing to distortion wavelength is further increased and approaches one (i.e., the number of blades equals the number of distortion cycles), the attenuation is decreased. This explains the decrease in attenuation for increasing values of reduced frequency which was observed with the six-bladed rotor; a decrease in attenuation was observed for the case of a six-bladed rotor in a six-cycle distortion. This conclusion is particularly important since it shows that, knowing the shape of the inlet distortion, the maximum attenuation can be achieved by designing a rotor such that the blade spacing is one-half the distortion wavelength. This conclusion also appears to be supported by the unsteady theory used in this investigation with one exception; no decrease in attenuation is observed for the uncambered rotor as the ratio of spacing to

to wavelength approaches one. In addition, the measured attenuation was found to be much greater than the attenuation predicted by the theoretical analysis. This is not surprising, however, since the theory does not account for the effect of viscosity.

6.2 Recommendations for Future Research

Besides providing data of a fundamental nature which demonstrate the effects of various design and operating variables on the response of a rotor to inlet distortions, this investigation also uncovered several areas where future research should be conducted. Some of the future research will serve to verify or explain the results of the present study. Other research should expand on the experimental and theoretical studies made in this investigation, thus providing a more complete and detailed understanding of turbomachinery unsteady aerodynamics and inlet distortion phenomena.

A more thorough investigation should be undertaken to determine the effects of the radial flows in the AFRF. It has been pointed out that radial shifts in the streamlines will alter the distortion amplitude at the mean radius and can yield misleading results with regard to the distortion attenuation and the unsteady losses.

Another recommendation for future research is to conduct a more extensive experimental program employing a larger number of distortion screens. This would give a larger number of reduced frequencies and intrablade frequencies, thus allowing both experimental and theoretical attenuation data and unsteady total pressure losses to be more accurately analyzed. Further experimental studies should be conducted with the nine-bladed cambered rotor in distortions with higher values of reduced

frequency or intrablade phase angle. This would help to verify the shape of the curve of the amplitude ratio as a function of blade spacing over distortion wavelength observed for the uncambered rotor. Also, low values of ω and τ should be tested experimentally with the six-bladed rotor since only the four- and six-cycle sinusoidal distortions were evaluated in the present study.

A large discrepancy was observed between the amount of attenuation measured experimentally and the amount of attenuation predicted by a two-dimensional, unsteady theoretical analysis. It was suggested that the discrepancy was caused by the fact that the effects of viscosity and turbulent mixing were neglected in the theory. Further study should be aimed at discovering the causes of the attenuation observed in the measured data and also at providing an analytical method which includes viscous effects in the prediction of the total pressure distribution downstream of the rotor. Mokelke in Reference [30] has analytically investigated the contribution of turbulent mixing, and a similar analysis could be used as a starting point for a study of the observed phenomena in the AFRF. From Reference [37], it is known that no significant turbulent mixing occurs without the rotor installed; if turbulent mixing is significant, it must be caused by the rotor.

The last topic to be included in recommendations for future research is the area of unsteady losses. A maximum value of unsteady losses at low values of reduced frequency was observed in References [37] and [40]. To verify such a peak for the six-bladed test rotor used in this study, measurements at lower values of reduced frequency are required. The effect of radial measurement location on the unsteady losses was found to be very important; however, no definitive explanation of the observed

AD-A084 446 PENNSYLVANIA STATE UNIV UNIVERSITY PARK APPLIED RESE--ETC F/G 21/5
THE UNSTEADY RESPONSE OF AN AXIAL FLOW TURBO-MACHINERY ROTOR TO--ETC(U)
OCT 78 L C BARR N00017-73-C-1418
UNCLASSIFIED ARL/PSU/TM-78-253 NL

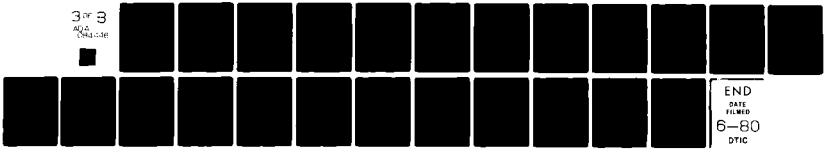

END
DATE FILMED
6-80
DTIC

behavior is available. Possible sources of unsteady losses are local regions of flow separation, turbulent mixing, vortex shedding due to the unsteady blade circulation, pressure and viscous drag, and hub and annulus wall boundary layers. The contributions of these sources to the losses should be investigated.

REFERENCES

1. Kemp, N. H. and W. R. Sears. "Aerodynamic Interference Between Moving Blade Rows." Journal of the Aeronautical Sciences, Vol. 20, No. 9, Sept. 1953, pp. 585-497.

2. Kemp, N. H. and W. R. Sears. "The Unsteady Forces Due to Viscous Wakes in Turbomachines." Journal of the Aeronautical Sciences, Vol. 22, No. 7, July 1955, pp. 478-483.

3. von Karman, T. and W. R. Sears. "Airfoil Theory for Non-Uniform Motion." Journal of the Aeronautical Sciences, Vol. 5, No. 10, Aug. 1938, pp. 379-390.

4. Sears, W. R. "Some Aspects of Non-Stationary Airfoil Theory and Its Practical Application." Journal of the Aeronautical Sciences, Vol. 8, No. 3, Jan. 1941, pp. 104-108.

5. Horlock, J. H. "Fluctuating Lift Forces on Aerofoils Moving Through Transverse and Chordwise Gusts." Journal of Basic Engineering, Vol. 90D, No. 4, Dec. 1968, pp. 494-500.

6. Naumann, H. and H. Yeh. "Lift and Pressure Fluctuations of a Cambered Airfoil Under Periodic Gusts and Applications in Turbomachinery." Journal of Engineering for Power, Vol. 95, No. 1, Jan. 1973, pp. 1-10.

7. Whitehead, D. S. "Force and Moment Coefficients for Vibrating Aerofoils in Cascade." Aeronautical Research Council Reports and Memoranda No. 3254, Feb. 1960.

8. Henderson, R. E. and H. Daneshyar. "Theoretical Analysis of Fluctuating Lift on the Rotor of an Axial Turbomachine." Aeronautical Research Council Reports and Memoranda No. 3684, 1971.

9. McCroskey, W. J. "Some Current Research in Unsteady Fluid Dynamics--The 1976 Freeman Scholar Lecture." Journal of Fluids Engineering, Vol. 99, No. 2, Mar. 1977, pp. 8-38.

10. Verdon, J. M. and J. E. McCune. "Unsteady Supersonic Cascade in Subsonic Axial Flow." AIAA Journal, Vol. 13, No. 2, Feb. 1975, pp. 193-201.

11. Jones, W. P. and J. A. Moore. "Aerodynamic Theory for a Cascade of Oscillating Airfoils in Subsonic Flow." AIAA Journal, Vol. 14, No. 5, May 1976, pp. 601-605.

12. Rao, B. M. and W. P. Jones. "Unsteady Airloads on a Cascade of Staggered Blades in Subsonic Flow." AGARD Conference Proceedings No. 177, Unsteady Phenomena in Turbomachinery, Sept. 1975, Paper No. 32.

REFERENCES (Continued)

13. Ni, R. H. and F. Sisto. "Numerical Computation of Nonstationary Aerodynamics of Flat Plate Cascades in Compressible Flow." Journal of Engineering for Power, Vol. 98, No. 2, Apr. 1976, pp. 165-170.

14. Adamczyk, J. J. "The Passage of a Distorted Velocity Field Through a Cascade of Airfoils," AGARD Conference Proceedings No. 177, Unsteady Phenomena in Turbomachinery, Sept. 1975, Paper No. 31.

15. Goldstein, M. E. and H. Atassi. "A Complete Second Order Theory for the Unsteady Flow About an Airfoil Due to a Periodic Gust." Journal of Fluid Mechanics, Vol. 74, Part 4, Apr. 1976, pp. 741-765.

16. Horlock, J. H., E. M. Greitzer, and R. E. Henderson. "The Response of Turbomachinery Blades to Low Frequency Inlet Distortions." Journal of Engineering for Power, Vol. 99, No. 2, Apr. 1977, pp. 195-203.

17. Namba, M. "Lifting Surface Theory for Unsteady Flows in a Rotating Annular Cascade." Revue Francaise de Mecanique, Numero Special, 1976, pp. 39-46.

18. Mazzawy, R. S. "Multiple Segment Parallel Compressor Model for Circumferential Flow Distortion." AGARD Conference Proceedings No. 177, Unsteady Phenomena in Turbomachinery, Sept. 1975, Paper No. 21.

19. Horlock, J. H. and H. Daneshyar. "Stagnation Pressure Changes in Unsteady Flow." Aeronautical Quarterly, Vol. XXII, Part III, Aug. 1971.

20. Hawthorne, W. R. "The Flow Through Moving Cascades of Lifting Lines with Fluctuating Lift." Aeronautical Research Council, Paper No. ARC 32369, 1970.

21. Henderson, R. E. "The Unsteady Response of an Axial Flow Turbomachine to an Upstream Disturbance." Ph.D. dissertation, Engineering Department, University of Cambridge, Oct. 1972.

22. Bruce, E. P. and R. E. Henderson. "Axial Flow Rotor Unsteady Response to Circumferential Inflow Distortions." AGARD Conference Proceedings No. 177, Unsteady Phenomena in Turbomachinery, Sept. 1975, Paper No. 18.

23. Fleeter, S., A. S. Novick, and R. E. Riffel. "An Experimental Determination of the Unsteady Aerodynamics in a Controlled Oscillating Cascade." ASME Paper 76-GT-17, Mar. 1976; Also AGARD Conference Proceedings No. 177, Unsteady Phenomena in Turbomachinery, Sept. 1975, Paper No. 27.

REFERENCES (Continued)

24. Carta, F. O. and A. O. St. Hilaire. "An Experimental Study of the Aerodynamic Response of a Subsonic Cascade Oscillating Near Stall." United Technologies Research Center, East Hartford, CT, Report R76-912270, July 1976.

25. Roberts, F., G. A. Plourde, and F. Smakula. "Insights into Axial Compressor Response to Distortion." AIAA Paper No. 68-565, 1968.

26. Plourde, G. A. and A. H. Stenning. "The Attenuation of Circumferential Inlet Distortion in Multi-Stage Axial Compressors." AIAA Paper No. 67-415, 1967.

27. Hawthorne, W. R. and J. H. Horlock. "Actuator Disc Theory of the Incompressible Flow in Axial Compressors." Proceedings of the Institution of Mechanical Engineers, Vol. 176, No. 30, 1962, pp. 789-803.

28. Hawthorne, W. R. and J. Ringrose. "Actuator Disc Theory of the Compressible Flow in Free-Vortex Turbomachinery." Proceedings of the Institution of Mechanical Engineers, Vol. 178, pv 3, 1963-64.

29. Rannie, W. D. and F. E. Marble. "Unsteady Flows in Axial Turbomachines." Communication Aux Journées Internationales de Sciences Aéronautiques, O.N.E.R.A., May 1957.

30. Mokelke, H. "Prediction Techniques." AGARD Lecture Series No. 72 on Distortion Induced Engine Instability, 1974.

31. Platzer, M. F. "Unsteady Flows in Turbomachines--A Review of Current Developments." Proceedings of AGARD Fluid Dynamics Panel Symposium, Unsteady Aerodynamics, Ottawa, Canada, Sept. 1977.

32. Henderson, R. E. "The Unsteady Response of a Blade Row from Measurements of the Time-Mean Total Pressure." ASME Paper No. 73-GT-94, Mar. 1973.

33. Dixon, S. L. Fluid Mechanics, Thermodynamics of Turbomachinery. Pergamon Press, 1975, pp. 54-59.

34. Bruce, E. P. "The Axial Flow Research Fan--A New Facility for Investigation of Time-Dependent Turbomachinery Flows." ASME Paper No. 74-FE-27, May 1974.

35. Bruce, E. P. "Design and Evaluation of Screens to Produce Multi-Cycle ±20% Amplitude Sinusoidal Velocity Profiles." AIAA Paper No. 74-623, July 1974.

REFERENCES (Continued)

36. Treaster, A. L. and A. M. Yocum. "The Calibration and Application of Five-Hole Probes." Proceedings of the 24th International Instrumentation Symposium, Instrument Society of American, Albuquerque, NM, May 1978.

37. Yocum, A. M. "The Effects of Design and Operating Variables on the Response of an Axial Flow Fan to Inlet Flow Distortions." Master of Science thesis, Department of Mechanical Engineering, The Pennsylvania State University, Aug. 1978.

38. Lieblein, S. "Experimental Flow in Two-Dimensional Cascades." National Aeronautics and Space Administration Special Publications No. 36, Aerodynamic Design of Axial-Flow Compressors, Chapter VI, 1965.

39. Barr, L. C. "Measurements of Inlet Flow Distortions in an Axial Flow Fan." Applied Research Laboratory Technical Memorandum 78-252, October 10, 1978.

40. Kirillov, I. I., A. S. Laskin, and G. G. Shpenzer. "Influence of Unsteadiness of the Flow on Efficiency of Turbine Stages." Teploenergetika, Vol. 17, No. 10, 1970.

41. Yurinskiy, V. T. and I. Ya. Shestachenko. "Losses in an Impulse Turbine Cascade in an Unsteady Flow." Fluid Mechanics--Soviet Research, Vol. 3, No. 1, 1974.

42. Horlock, J. H. Axial Flow Compressors. Huntingdon, NY: Robert E. Krieger Publishing Co., 1973.

APPENDIX A

RESOLUTION OF THE VELOCITY COMPONENTS FOR THE FIVE-HOLE PROBES

In this appendix, an analytical development of the vector resolution of the three velocity components measured by the five-hole probes is presented. It is desired to know the axial, circumferential, and radial components of a velocity vector $\overline{V}$ at angles γ and μ with respect to the local probe axes. Actually, these components depend on the definition of the pitch angle γ and the yaw angle μ. Calibration of the probe where the first rotation was in the yaw plane followed by rotation in the pitch plane (THE YAW-PITCH MODE) yield one set of values for the velocity components. However, the alternate rotational procedure, that is, the pitch-yaw mode, will result in distinctly different values for the velocity components. The particular five-hole probes used in this study were calibrated in the yaw-pitch mode. Thus, only the vector resolution for probes calibrated in the yaw-pitch mode will be presented. This derivation of the velocity components exactly follows that presented in Reference [36], and is reproduced here for convenience.

Consider any vector $\overline{V}$ whose components are V_1, V_2, and V_3 in the original or unprimed coordinate system and V_1', V_2', and V_3' in the primed or rotated coordinate system (see Figure A.1). It can be shown that the primed components can be computed from

$$V_1' = \sum_j a_{ij} V_j \ , \tag{A.1}$$

where a_{ij}'s are the direction cosines defined by:

$$a_{ij} = \cos\ (X_i', X_j) \ . \tag{A.2}$$

The symbol (X_i', X_j) represents the angle between the positive direction of the axes X_i' and X_j.

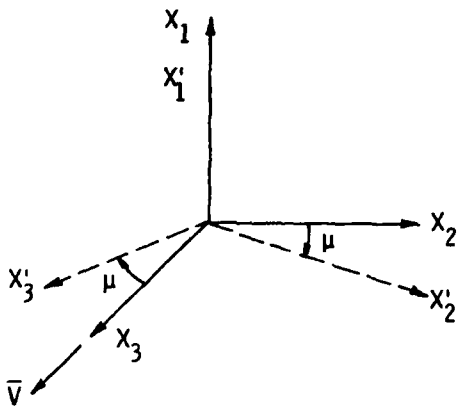

Figure A-1. Rotated Coordinate System

Let $\bar{V}$ be the reference velocity in the positive X_3 direction of the original coordinate system; that is, $V_1 = 0.0$, $V_2 = 0.0$, and $V_3 = \bar{V}$. The first rotation is a yawing motion about the X_1 axis of magnitude μ. The geometry is illustrated in Figure A.1.

Thus,

$$a_{11} = \cos(X_1', X_1) = \cos(0°) = 1.0,$$
$$a_{21} = \cos(X_2', X_1) = \cos(90°) = 0.0,$$
$$a_{31} = \cos(X_3', X_1) = \cos(90°) = 0.0,$$
$$a_{12} = \cos(X_1', X_2) = \cos(90°) = 0.0,$$
$$a_{22} = \cos(X_2', X_2) = \cos(\mu) = \cos\mu, \qquad (A.3)$$
$$a_{32} = \cos(X_3', X_2) = \cos(90°+\mu) = -\sin\mu,$$
$$a_{13} = \cos(X_1', X_3) = \cos(90°) = 0.0,$$
$$a_{23} = \cos(X_2', X_3) = \cos(90°-\mu) = \sin\mu,$$

and

$$a_{33} = \cos(X_3', X_3) = \cos\mu .$$

From Equation (A.1), the components of $\bar{V}$ in the rotated axis system are:

$$V_1' = a_{11} V_1 + a_{12} V_2 + a_{13} V_3 = 0.0, \qquad (A.4)$$

$$V_2' = a_{21} V_1 + a_{22} V_2 + a_{23} V_3 = \bar{V} \sin\mu, \qquad (A.5)$$

and

$$V_3' = a_{31} V_1 + a_{32} V_2 + a_{33} V_3 = \bar{V} \sin\mu. \qquad (A.6)$$

For the yaw-pitch calibration, the next rotation is a pitching motion about the X_2' axis of magnitude α. This final axis orientation will be denoted by the double primed symbols. The geometry is shown in Figure A.2.

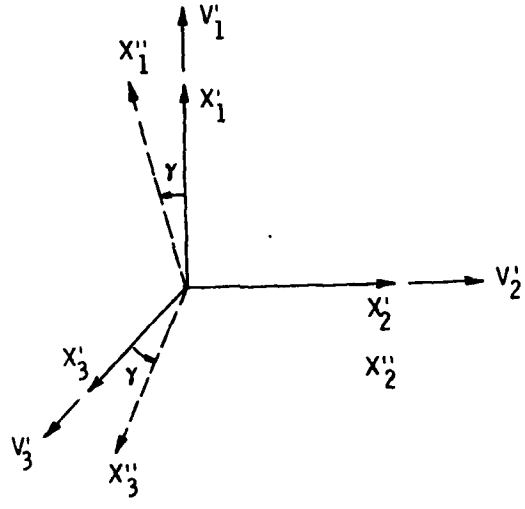

Figure A-2. Final Coordinate System

$$
\begin{aligned}
a_{11} &= \cos(X_1'', X_1') = \cos\gamma, \\
a_{21} &= \cos(X_2'', X_1') = \cos(90°) = 0.0, \\
a_{31} &= \cos(X_3'', X_1') = \cos(90°+\gamma) = -\sin\gamma, \\
a_{12} &= \cos(X_1'', X_2') = \cos(90°) = 0.0, \\
a_{22} &= \cos(X_2'', X_2') = \cos(0°) = 1.0, \\
a_{32} &= \cos(X_3'', X_2') = \cos(90°) = 0.0, \\
a_{13} &= \cos(X_1'', X_3') = \cos(90°-\gamma) = \sin\gamma, \\
a_{23} &= \cos(X_2'', X_3') = \cos(90°) = 0.0,
\end{aligned}
\tag{A.7}
$$

and

$$a_{33} = \cos(X_3'', X_3') = \cos\gamma.$$

The components of V_1'', V_2'', and V_3'' of the original vector $\bar{V}$ relative to the final axis orientation are obtained by combining Equations A.4 through A.7, using Equation A.1.

$$V_1'' = a_{11} V_1' + a_{12} V_2' + a_{13} V_3' = \bar{V}\cos\mu\sin\gamma, \quad (A.8)$$

$$V_2'' = a_{21} V_1' + a_{22} V_2' + a_{23} V_3' = \bar{V}\sin\mu, \quad (A.9)$$

and

$$V_3'' = a_{31} V_1' + a_{32} V_2' + a_{33} V_3' = V\cos\mu\cos\gamma. \quad (A.10)$$

In many applications, these three velocity components are identified as follows:

$$\text{Radial:} \quad V_R = V_1'' = \bar{V}\cos\mu\sin\gamma. \quad (A.11)$$

$$\text{Circumferential:} \quad V_\theta = V_2'' = \bar{V}\sin\mu. \quad (A.12)$$

$$\text{Axial:} \quad V_X = V_3'' = \bar{V}\cos\mu\cos\gamma. \quad (A.13)$$

For surface ship applications, V_R is positive when directed radially inward along the longitudinal probe axis; V_θ is positive when directed counterclockwise when looking upstream; and V_X is positive in the axial direction as shown in Figure A.3.

In some cases where the rotor was operated at large blade loadings, there were large components of circumferential velocity, or swirl, present downstream of the rotor. In these cases, the values of the downstream yaw angle sensed by the probe were large and fell outside the calibration range of ±30 degrees. Since the velocity components were calculated using the probe calibration data, the velocities calculated for these particular cases were meaningless. Thus, it was necessary to rotate the probe in the counterclockwise direction by an angle σ in order that the probe would

sense yaw angle values within the calibration range. When the probe is rotated in this manner, the equations for the yaw and pitch angles used in the data reduction program must be changed. The derivation of these new angles is presented here.

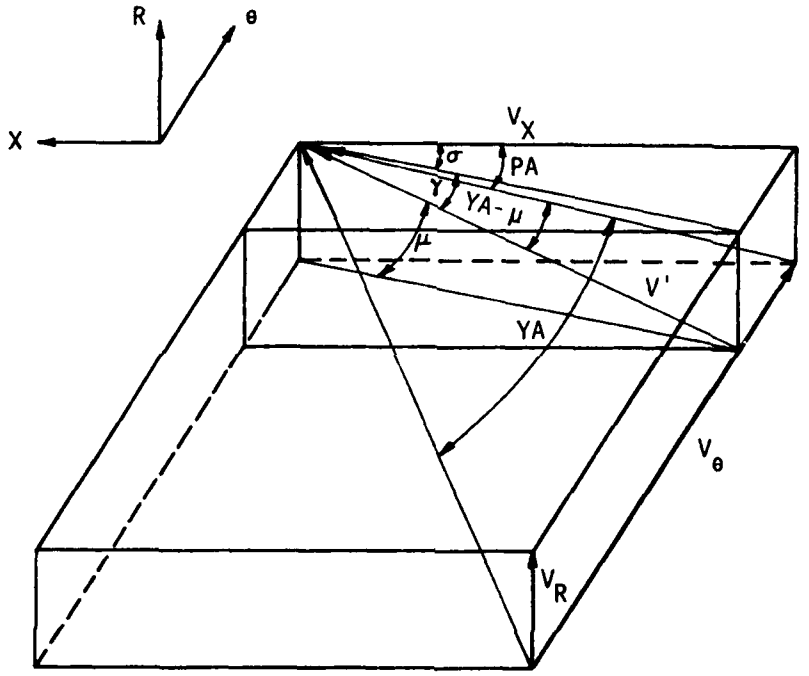

Figure A-3. Velocity Components and Angles

Referring to Figure A.3, the angles γ and μ are the pitch and yaw angles relative to the probe; PA and YA are the pitch and yaw angles relative to the axial reference, and they are the angles used in the data reduction program. σ is the angle that the probe is rotated.

The three velocity components are unchanged:

$$V_X = V\cos YA\cos PA, \tag{A.11}$$

$$V_\theta = V\sin YA, \tag{A.12}$$

and

$$V_r = V\cos YA\sin PA. \tag{A.13}$$

Now, with the probe rotated, we have:

$$V_X = V' \cos (YA-\mu) \cos PA, \tag{A.14}$$

$$V_X = V'\cos\gamma\cos\sigma, \tag{A.15}$$

$$V_r = V'\sin\gamma, \tag{A.16}$$

$$V_r = V'\cos (YA-\mu) \sin PA, \tag{A.17}$$

$$\cos (YA-\mu) \cos PA = \cos\gamma\cos\sigma, \tag{A.18}$$

and

$$\sin\gamma = \cos (YA-\mu) \sin PA\,. \tag{A.19}$$

Substitution of Equation (A.19) into Equation (A.18) gives:

$$\frac{\sin\gamma}{\sin} \cos PA = \cos\gamma\cos\sigma .$$

Then, by rearranging, we have:

$$\frac{\cos PA}{\sin PA} = \frac{\cos\gamma}{\sin\gamma} \cos\sigma$$

and

$$\tan PA = \frac{\tan\gamma}{\sin\sigma} .$$

Therefore,

$$PA = \tan^{-1} \left(\frac{\tan\gamma}{\cos\sigma}\right). \qquad (A.20)$$

From equation (A.18),

$$\cos (YA-\mu) = \frac{\cos\gamma\cos\sigma}{\cos PA} .$$

Therefore,

$$YA = \cos^{-1} \left(\frac{\cos\gamma}{\cos PA} \cos\sigma\right) + \mu . \qquad (A.21)$$

Equations (A.20) and (A.21) are the new angles which are used in the cases where the downstream probe is rotated counterclockwise in the yaw plane.

APPENDIX B

SUMMARY OF EXPERIMENTAL TEST CONDITIONS

Table B.1. Table of Run Conditions Completed for the Six-Bladed Rotor

Screen	Stagger (Deg.)	RPM	Avg. $\frac{V_X}{U_m}$	Avg. $\frac{\Delta P_T}{1/2\rho V_X^2 avg.}$	Avg. Incidence (Deg.)
4-Cycle Sinusoidal Distortion	35	682	1.303	0.023	2.29
	35	941	0.992	0.454	10.12
	35	1203	0.802	1.004	16.24
	45	975	0.985	0.014	0.40
	45	1293	0.739	0.660	8.50
	55	1392	0.675	0.093	0.57
	55	1622	0.526	0.848	6.78
	55	1913	0.493	1.732	8.35
6-Cycle Sinusoidal Distortion	35	714	1.354	0.001	1.20
	35	1020	1.010	0.424	9.58
	35	1260	0.814	0.911	15.79
	45	1020	0.971	0.029	0.76
	45	1413	0.696	0.851	10.13
	55	1457	0.679	0.131	0.19
	55	1698	0.586	0.708	4.25
	55	2002	0.487	1.767	8.52

Table B.1. Table of Run Conditions Completed for the Six-Bladed Rotor (Continued)

Screen	Stagger (Deg.)	RPM	Avg. $\frac{V_X}{U_m}$	Avg. $\frac{\Delta P_T}{1/2\rho V_X^2 \text{ avg.}}$	Avg. Incidence (Deg.)
90 Degree Square Distortion	35	696	1.363	0.009	1.29
	35	993	0.963	0.479	11.07
	35	1143	0.817	0.847	15.75
	45	994	0.990	0.027	0.34
	45	1375	0.722	0.800	9.18
	55	1419	0.615	0.145	3.02
	55	1653	0.552	0.785	5.57
	55	1950	0.483	1.787	8.84
180 Degree Square Distortion	35	692	1.396	0.017	0.80
	35	955	0.977	0.435	10.78
	35	1138	0.866	0.766	14.18
	45	989	0.951	0.054	1.57
	45	1328	0.717	0.755	9.41
	55	1412	0.634	0.148	2.18
	55	1646	0.533	0.801	6.47
	55	1941	0.474	1.794	9.35

Table B.2. Table of Run Conditions Completed for the Nine-Bladed Rotor With a Rotor-Stator Spacing of 12 Inches (30.48 cm)

Screen	Stagger (Deg.)	RPM	Avg. $\frac{V_X}{U_m}$	Avg. $\frac{\Delta P_T}{1/2\rho V_X^2 \text{ avg.}}$	Avg. Incidence (Deg.)
1-Cycle	50	1525	0.647	1.104	0.65
Sinusoidal	50	1699	0.583	1.775	3.36
Distortion	50	1837	0.532	2.444	5.65
2-Cycle	50	1529	0.638	1.188	1.18
Sinusoidal	50	1704	0.564	1.960	4.28
Distortion	50	1842	0.517	2.623	6.40
4-Cycle	50	1492	0.620	1.281	1.88
Sinusoidal	50	1663	0.536	2.248	5.47
Distortion	50	1798	0.492	2.951	7.50
6-Cycle	50	1462	0.626	1.244	1.65
Sinusoidal	50	1741	0.527	2.316	5.97
Distortion	50	1882	0.530	2.515	5.81
90 Degree	50	1521	0.616	1.260	2.08
Square	50	1695	0.574	1.800	3.84
Distortion	50	1833	0.523	2.494	6.09
180 Degree	50	1515	0.605	1.295	2.56
Square	50	1688	0.553	2.011	4.79
Distortion	50	1825	0.507	2.679	6.85

Table B.3. Table of Run Conditions Completed for the Nine-Bladed Rotor With a Rotor-Stator Spacing of 3 Inches (7.62 cm)

Screen	Stagger (Deg.)	RPM	Avg. $\frac{V_X}{U_m}$	Avg. $\frac{\Delta P_T}{1/2\rho V_X^2 \text{ avg.}}$	Avg. Incidence (Deg.)
1-Cycle	50	1525	0.644	1.117	0.95
Sinusoidal	50	1699	0.577	1.825	3.73
Distortion	50	1837	0.532	2.364	5.72
2-Cycle	50	1529	0.632	1.210	1.56
Sinusoidal	50	1704	0.565	1.910	4.37
Distortion	50	1842	0.514	2.639	6.64
4-Cycle	50	1492	0.610	1.356	2.41
Sinusoidal	50	1663	0.534	2.252	4.70
Distortion	50	1798	0.489	2.968	7.74
6-Cycle	50	1562	0.618	1.301	2.09
Sinusoidal	50	1741	0.536	2.133	5.61
Distortion	50	1882	0.541	2.305	5.40
90 Degree	50	1521	0.604	1.360	2.70
Square	50	1696	0.573	1.796	3.99
Distortion	50	1833	0.522	2.482	6.28
180 Degree	50	1515	0.606	1.268	2.69
Square	50	1688	0.579	1.762	3.75
Distortion	50	1825	0.530	2.356	4.94

Table B.4. Table of Run Conditions Completed for the Nine-Bladed Rotor With the Probe Located at a Radial Distance of 4.583 Inches (11.64 cm) from the Hub Surface*

Screen	Stagger (Deg.)	RPM	Avg. $\frac{V_X}{U_m}$	Avg. $\frac{\Delta P_T}{1/2\rho V_X^2 \text{ avg.}}$	Avg. Incidence (Deg.)
2-Cycle	50	1704	0.537	2.289	5.59
4-Cycle	50	1663	0.534	2.313	5.77
90 Deg. Sq.	50	1695	0.531	2.255	5.86
180 Deg. Sq.	50	1688	0.530	2.272	5.95

Table B.5. Table of Run Conditions Completed for the Nine-Bladed Rotor With the Probe Located at a Radial Distance of 3.667 Inches (9.31 cm) from the Hub Surface

Screen	Stagger (Deg.)	RPM	Avg. $\frac{V_X}{U_m}$	Avg. $\frac{\Delta P_T}{1/2\rho V_X^2 \text{ avg.}}$	Avg. Incidence (Deg.)
2-Cycle	50	1704	0.547	2.131	5.22
4-Cycle	50	1663	0.529	2.321	5.97
90 Deg. Sq.	50	1695	0.540	2.118	5.53
180 Deg. Sq.	50	1688	0.583	1.807	3.66

*NOTE: The mean radius is 2.75 inches (6.99 cm) from the Hub Surface.

Table B.6. Table of Run Conditions Completed for the Nine-Bladed Rotor With the Probe Located at a Radial Distance of 1.833 Inches (4.66 cm) from the Hub Surface

Screen	Stagger (Deg.)	RPM	Avg. $\frac{V_X}{U_m}$	Avg. $\frac{\Delta P_T}{1/2\rho V_X^2 \text{ avg.}}$	Avg. Incidence (Deg.)
2-Cycle	50	1704	0.567	1.882	4.22
4-Cycle	50	1663	0.552	1.997	4.87
90 Deg. Sq.	50	1695	0.541	2.062	5.36
180 Deg. Sq.	50	1688	0.528	2.165	5.95

Table B.7. Table of Run Conditions Completed for the Nine-Bladed Rotor With the Probe Located at a Radial Distance of 0.917 Inch (2.33 cm) from the Hub Surface

Screen	Stagger (Deg.)	RPM	Avg. $\frac{V_X}{U_m}$	Avg. $\frac{\Delta P_T}{1/2\rho V_X^2 \text{ avg.}}$	Avg. Incidence (Deg.)
2-Cycle	50	1704	0.533	2.059	5.81
4-Cycle	50	1663	0.519	2.198	6.46
90 Deg. Sq.	50	1695	0.555	1.917	4.70
180 Deg. Sq.	50	1688	0.547	1.949	5.06

DISTRIBUTION LIST FOR ARL UNCLASSIFIED TM 78-253 by L. C. Barr, dated October 12, 1978

Commander
Naval Sea Systems Command
Department of the Navy
Washington, DC 02362
Attn: Library
Code NSEA-09G32
(Copy Nos. 1 and 2)

Naval Sea Systems Command
Attn: E. J. McKinney
Code NSEA-0342
(Copy Nos. 3 and 4)

Naval Sea Systems Command
Attn: T. E. Peirce
Code NSEA-0351
(Copy No. 5)

Naval Sea Systems Command
Attn: A. R. Paladino
Code NSEA-0372
(Copy No. 6)

Defense Documentation Center
5010 Duke Street
Cameron Station
Alexandria, VA 22314
(Copy Nos. 7-18)

Commander
Naval Ship Engineering Center
Washington, DC 02362
Attn: D. Burke
Code NSEC-6140B.1
(Copy No. 19)

Commanding Officer
Naval Underwater Systems Center
Newport, RI 02840
Attn: Library
Code 54
(Copy No. 20)

Commanding Officer
Naval Ocean Systems Center
San Diego, CA 92152
Attn: D. Nelson
Code 6342
(Copy No. 21)

Naval Ocean Systems Center
Attn: Library
(Copy No. 22)

Naval Ocean Systems Center
Attn: M. Reischman
Code 2542
(Copy No. 23)

Commanding Officer and Director
David W. Taylor Naval Ship R&D Center
Department of the Navy
Bethesda, MD 20084
Attn: W. B. Morgan
Code 154
(Copy No. 24)

David W. Taylor Naval Ship R&D Center
Attn: R. Cumming
Code 1544
(Copy No. 25)

David W. Taylor Naval Ship R&D Center
Attn: J. McCarthy
Code 1552
(Copy No. 26)

David W. Taylor Naval Ship R&D Center
Attn: M. Sevik
Code 19
(Copy No. 27)

David W. Taylor Naval Ship R&D Center
Attn: W. K. Blake
Code 1942
(Copy No. 28)

Commanding Officer & Director
David W. Taylor Naval Ship R&D Center
Department of the Navy
Annapolis Laboratory
Annapolis, MD 21402
Attn: J. G. Stricker
Code 2721
(Copy No. 29)

Commander
Naval Surface Weapon Center
Silver Spring, MD 20910
Attn: Library
(Copy No. 30)

DISTRIBUTION LIST FOR ARL UNCLASSIFIED TM 78-253 by L. C. Barr, dated October 12, 1978

NASA Lewis Research Center
21000 Brookpark Road
Cleveland, OH 44135
Attn: N. C. Sanger
MS 5-9
(Copy No. 31)

NASA Lewis Research Center
Attn: M. J. Hartmann
MS 5-9
(Copy No. 32)

NASA Lewis Research Center
Attn: D. M. Sandercock
MS 5-9
(Copy No. 33)

NASA Lewis Research Center
Attn: W. M. McNally
MS 5-9

NASA Lewis Research Center
Attn: J. Adamczyk
MS 5-9
(Copy No. 35)

NASA Lewis Research Center
Attn: Library
(Copy No. 36)

NASA Lewis Research Center
Attn: D. Morris
MS 60-3
(Copy No. 37)

General Applied Science Labs.
Merrick and Stewart Avenues
Westbury, NY 11590
(Copy No. 38)

Arnold Air Force Station
Tennessee 37389
Attn: Library
(Copy No. 39)

Air Force Aero Propulsion Laboratory
Wright-Patterson Air Force Base
Ohio 45433
Attn: Library
(Copy No. 40)

Air Force Office of Scientific Research
1400 Wilson Boulevard
Arlington, VA 22209
Attn: Dr. J. F. Masi
(Copy No. 41)

NASA Ames Research Center
Moffett Field, CA 94085
Attn: Library
(Copy No. 42)

NASA Ames Research Center
Attn: Dr. S. Bodapati
MA 227-9
(Copy No. 43)

NASA Langley Research Center
Hampton, VA 23365
Attn: Library
(Copy No. 44)

National Technical Information Service
Department of Commerce
5285 Port Royal Road
Springfield, VA 22151
Attn: Chief, Input Section
(Copy No. 45)

Naval Postgraduate School
Monterey, CA 93940
Attn: Library
Code 0212
(Copy No. 46)

Office of Naval Research
Department of the Navy
Arlington, VA 22217
Attn: J. Patton
(Copy No. 47)

Calspan Corporation
4455 Genessee Street
Buffalo, NY 14221
Attn: Head Librarian
(Copy No. 48)

DISTRIBUTION LIST FOR ARL UNCLASSIFIED TM 78-253 by L. C. Barr, dated October 12, 1978

Detroit Diesel Allison Division
P. O. Box 894
Indianapolis, Indiana 46206
Attn: D. S. Fleeter
(Copy No. 49)

Detroit Diesel Allison Division
Attn: Library
(Copy No. 50)

Garrett Corporation
Air Research Manufacturing Company
Sky Harbor Airport
402 South 36th Street
Phoenix, Arizona 85034
Attn: Library
(Copy No. 51)

General Electric Company
Cincinnati, Ohio 45215
Attn: Library
(Copy No. 52)

General Electric Company
Corporate Research & Development
P. O. Box 8
Schenectady, NY 12301
Attn: Library
(Copy No. 53)

General Electric Company
1000 Western Avenue
West Lynn, Massachusetts 01910
Attn: Library
(Copy No. 54)

LTV Vought Aeronautics Company
P. O. Box 5907
Dallas, Texas 75000
Attn: Library
(Copy No. 55)

Lockheed-Georgia Company
Marietta, Geomgia 30060
Attn: Library
(Copy No. 56)

Lockheed Propulsion Company
Scientific and Technical Library
P. O. Box 111
Redlands, CA 92373
Attn: Head Librarian
(Copy No. 57)

McDonnell Aircraft Company
P. O. Box 516
St. Louis, Missouri 63166
Attn: Res. & Eng. Library
Dept. 218 - Bldg. 101
(Copy No. 58)

Nielsen Eng. & Research, Inc.
510 Clyde Avenue
Mountain View, CA 94040
Attn: Dr. J. N. Nielsen
(Copy No. 59)

Pratt and Whitney Aircraft Division
United Aircraft Company
400 S. Main Street
East Hartford, Connecticut 06108
Attn: Library
(Copy No. 60)

Pratt and Whitney Aircraft Division
Attn: R. Mazzaway
(Copy No. 61)

Pratt and Whitney Aircraft
Florida Res. & Dev. Center
P. O. Box 2691
West Palm Beach, Florida 33402
Attn: Library
(Copy No. 62)

United Aircraft Research Laboratory
East Hartford, Connecticut 06108
Attn: Dr. F. Carta
(Copy No. 63)

United Aircraft Research Laboratory
Attn: Librarian
(Copy No. 64)

DISTRIBUTION LIST FOR ARL UNCLASSIFIED TM 78-253 by L. C. Barr, dated October 12, 1978

California Institute of Technology
Jet Propulsion Laboratory
4800 Oak Grove Drive
Pasadena, CA 91130
Attn: Library
(Copy No. 65)

Case Western Reserve University
10900 Euclid Avenue
Cleveland, Ohio 44106
Attn: Sears Library - Reports Dept.
(Copy No. 66)

Massachusetts Institute of Technology
77 Massachusetts Avenue
Cambridge, Massachusetts 02139
Attn: Dr. E. M. Greitzer
(Copy No. 67)

Massachusetts Institute of Technology
Attn: Technical Reports - MIT Libraries
Room 14 E-210
(Copy No. 68)

Massachusetts Institute of Technology
Attn: Eng. Tech. Reprts. - Room 10-408
(Copy No. 69)

Virginia Polytechnic Inst. &
State University
Mechanical Engineering Dept.
Blackburg, Virginia 24061
Attn: Mr. W. F. O'Brien, Jr.
(Copy No. 70)

Virginia Polytechnic Inst. &
State University
Attn: Library
(Copy No. 71)

Dr. John H. Horlock
Vice Chancellor
University of Salford
Salford, M5 4WT
ENGLAND
(Copy No. 72)

Dr. G. K. Serovy
Mechanical Engineering Department
Iowa State University
Ames, Iowa 50010
(Copy No. 73)

Von Karman Inst. for Fluid Dynamics
Turbomachinery Laboratory
Rhode-Saint-Genese
Belgium
Attn: Library
(Copy No. 74)

Dr. D. S. Thompson
Turbine Research Department
Rolls Royce Ltd.
P. O. Box 31
Derby, England
(Copy No. 75)

Whittle Turbomachinery Laboratory
Madingley Road
Cambridge, England
Attn: Library
(Copy No. 76)

Whittle Turbomachinery Laboratory
Attn: Sir William Hawthorne
(Copy No. 77)

Prof. R. E. Peacock
School of Mechanical Engineering
Cranfield Institute of Technology
Cranfield, Bedford MK430AL
England
(Copy No. 78)

Dr. Hand Mikelke
Mut-Munchen GMBLT
8 Munchen 50
Postfack 50 06 40
Germany
(Copy No. 79)

Dr. S. N. B. Murthy
Thermal Science & Prop. Center
Purdue University
West Lafayette, Indiana 47907
(Copy No. 80)

Prof. J. P. Gostelow
School of Mechanical Eng.
NSW Institute of Technology
Broadway
Sidney, Australia
(Copy No. 81)

DISTRIBUTION LIST FOR ARL UNCLASSIFIED TM 78-253 by L. C. Barr, dated October 12, 1978

Applied Research Laboratory
Post Office Box 30
State College, PA 16801
Attn: E. P. Bruce
(Copy No. 82)

Applied Research Laboratory
B. Lakshminarayana
(Copy No. 83)

Applied Research Laboratory
Attn: A. M. Yocum
(Copy No. 84)